

A PROPELLER DESIGN AND ANALYSIS CAPABILITY  
EVALUATION FOR HIGH ALTITUDE APPLICATION

**John Steven Monk**

A dissertation submitted to the Faculty of Engineering and the Built Environment,  
University of the Witwatersrand, Johannesburg, in fulfilment of the requirements  
for the degree of Master of Science in Engineering.

Johannesburg, 2010

## DECLARATION

I declare that this dissertation is my own, unaided work except where otherwise indicated. It is being submitted for the degree of Master of Science in the University of the Witwatersrand, Johannesburg. It has not been submitted before for any degree or examination at any other university.

---

John Monk

\_\_\_\_\_ day of \_\_\_\_\_ 20\_\_\_\_

## **ABSTRACT**

The purpose of this research is the evaluation of a relatively simple minimum induced loss propeller design and a radially-graded momentum theory analysis method to provide the initial propeller design and analysis capability for predicting propeller performance of a High Altitude Long Endurance (HALE) flight vehicle. These design and analysis capabilities cover flight conditions from take off at sea level to the low air density, high true airspeeds and high blade Mach numbers of high altitude flight. A conceptual propeller was designed and its performance analysed within a time-stepped mission simulation code. Wind tunnel tests were carried out on a scaled model of the propeller comparing actual performance against theoretical predictions. The design method was shown to be capable of producing a propeller design that could provide sufficient thrust over a large range of advance ratios (0.12 to 0.4) and altitudes (0 to 15 000 m). Agreement between the predicted and measured results is particularly good at the lower thrust coefficients and advance ratios, at higher power coefficients and advance ratios increasing differences between the predicted and measured results became apparent.

## **ACKNOWLEDGEMENTS**

I would like to express my thanks to my supervisors, Drs. Craig Law and Jimoh Pedro for their assistance in and advice on the completion of this work, the CSIR for the funding that was provided for the manufacture of the propeller test rig and Mr. Peter Skinner for the fruitful technical discussions, advice and wind tunnel test support.

My deepest gratitude is extended to my wife, Lorraine for her support and encouragement, enabling me to complete this work through some of the busiest times in my life. Finally I owe a great deal to my children, Michelle and Matthew who missed out on many hours of family time that should rightly have been theirs.

# CONTENTS

<b>DECLARATION</b>	<b>II</b>
<b>ABSTRACT</b>	<b>III</b>
<b>ACKNOWLEDGEMENTS</b>	<b>IV</b>
<b>CONTENTS</b>	<b>V</b>
<b>LIST OF FIGURES</b>	<b>VIII</b>
<b>LIST OF TABLES</b>	<b>XI</b>
<b>LIST OF SYMBOLS</b>	<b>XII</b>
<b>ACRONYMS</b>	<b>XIII</b>
<b>1. INTRODUCTION</b>	<b>1</b>
<b>1.1. Historical Development of Propeller Design Theories</b>	<b>1</b>
<b>1.2. Motivation</b>	<b>3</b>
<b>1.3. Objectives</b>	<b>3</b>
<b>1.4. Roadmap</b>	<b>4</b>
<b>2. LITERATURE SURVEY</b>	<b>6</b>
<b>2.1. An Introduction to Larrabee’s Design and Analysis Methods</b>	<b>6</b>
2.1.1 Larrabee’s Minimum Induced Loss Design Method	6
2.1.2 Larrabee’s Graded Momentum Theory Analysis Method	7
<b>2.2. Literature Survey on High Altitude Propellers</b>	<b>8</b>
2.2.1 Pathfinder, Centurion and Helios propellers	9
2.2.2 Strato 2C propellers	10
<b>2.3. Investigation into the Wind Tunnel Testing of Propellers</b>	<b>12</b>
2.3.1 Propeller test rigs	12
2.3.2 Balances	13
2.3.3 Test Techniques	14
<b>3. APPLICABILITY OF LARRABEE’S METHOD TO THE HALE UAV DESIGN</b>	<b>15</b>
3.1.1 Low disc loading assumption and Small Angle Approximations	15
3.1.2 Exclusion of Viscous Terms	16
3.1.3 Applicability of a Point Performance Design Method	17
<b>4. INITIAL HALE UAV PROPELLER DESIGN AND ANALYSIS</b>	<b>18</b>
<b>4.1. Propeller Design Requirements Specification</b>	<b>18</b>
4.1.1 UAV Mission Description	18
4.1.2 UAV Performance	20
4.1.3 Propeller Design Constraints	21
4.1.4 Atmospheric Modelling	22
<b>4.2. Initial Propeller Design and Analysis</b>	<b>23</b>

4.2.1	Initial Propeller Design	23
4.2.2	Initial Propeller Analysis	28
<b>4.3.</b>	<b>Aerofoil Selection</b>	<b>30</b>
<b>4.4.</b>	<b>Aerofoil Analysis</b>	<b>32</b>
4.4.1	Choice of Aerofoil Analysis Code	32
4.4.2	Radial Distribution of Aerofoil Sections	34
4.4.3	Prediction of Aerofoil Characteristics	34
<b>5.</b>	<b>MISSION PROPELLER DESIGN AND ANALYSIS</b>	<b>39</b>
<b>5.1.</b>	<b>Propeller Design in the Mission Simulation Program</b>	<b>39</b>
<b>5.2.</b>	<b>Propeller Performance Analysis in the Mission Simulation Program</b>	<b>40</b>
5.2.1	Climb Performance Analysis	40
5.2.2	Cruise Performance Analysis	41
<b>5.3.</b>	<b>Results of Analyses</b>	<b>41</b>
<b>5.4.</b>	<b>Choice of Propeller Design</b>	<b>42</b>
<b>5.5.</b>	<b>Predicted mission performance</b>	<b>44</b>
<b>5.6.</b>	<b>Comment on Design Capability</b>	<b>47</b>
<b>5.7.</b>	<b>Prediction of Wind Tunnel Propeller Performance</b>	<b>48</b>
<b>6.</b>	<b>DESIGN AND MANUFACTURE OF THE TEST EQUIPMENT</b>	<b>51</b>
<b>6.1.</b>	<b>Sizing of propeller</b>	<b>51</b>
6.1.1	Choice of Materials	52
6.1.2	Test Propeller Geometric Definition	52
6.1.3	Calculation of the Blade and Hub Stressing	56
6.1.4	Blade Root Stresses	56
6.1.5	Ground Adjustable Hub stresses	59
6.1.6	Manufacture of the Test Propeller	60
<b>6.2.</b>	<b>Conceptual Design of the Propeller Test Rig</b>	<b>61</b>
<b>6.3.</b>	<b>Manufacture of the Propeller Test Rig</b>	<b>62</b>
6.3.1	Propeller Drive Shaft	64
6.3.2	Flexure Design	64
6.3.3	Thrust measurement	65
6.3.4	Fairing geometry	66
6.3.5	Torque Measurements	68
<b>6.4.</b>	<b>Calibration of Load Cells</b>	<b>68</b>
6.4.1	Torque Transducer	68
6.4.2	Thrust load cell	68
<b>6.5.</b>	<b>Electromagnetic Interference effects</b>	<b>69</b>
<b>6.6.</b>	<b>Data Acquisition</b>	<b>69</b>
<b>7.</b>	<b>WIND TUNNEL TESTS</b>	<b>70</b>
<b>7.1.</b>	<b>Correction Factors - tare and Interference</b>	<b>70</b>

<b>7.2.</b>	<b>Description of the First Wind Tunnel Test Series</b>	<b>70</b>
7.2.1	Wind Tunnel Set-up	70
7.2.2	Tare and Interference prediction / measurements	71
7.2.3	Prop-wash effects on tare corrections	72
7.2.4	Test Methodology	72
<b>7.3.</b>	<b>Test Matrix</b>	<b>75</b>
<b>7.4.</b>	<b>Wind Tunnel Test Results</b>	<b>77</b>
<b>7.5.</b>	<b>Comparison between Theoretical and Predicted Results</b>	<b>78</b>
<b>7.6.</b>	<b>Propeller Geometric Error</b>	<b>80</b>
<b>7.7.</b>	<b>Second Wind Tunnel Test Series</b>	<b>82</b>
7.7.1	Modifications to Test Rig for Second Test Series	82
7.7.2	Wind Tunnel Set-up	85
7.7.3	Tare and Interference prediction/measurements	85
7.7.4	Propeller induced velocity effects on tare corrections	86
7.7.5	Test Methodology	86
7.7.6	Motor Characterisation	87
<b>7.8.</b>	<b>Torque Prediction</b>	<b>89</b>
<b>7.9.</b>	<b>Results from the second test series</b>	<b>89</b>
7.9.1	Thrust Coefficient	90
7.9.2	Power Coefficient	91
<b>8.</b>	<b>DESIGN METHODOLOGY ASSESSMENT</b>	<b>93</b>
<b>9.</b>	<b>CONCLUSIONS AND RECOMMENDATIONS</b>	<b>95</b>
	<b>REFERENCES</b>	<b>97</b>
	<b>APPENDIX A AEROFOIL DATA</b>	<b>102</b>
	<b>APPENDIX B TARE CORRECTIONS</b>	<b>117</b>
	<b>APPENDIX C THRUST LOAD CELL CALIBRATION</b>	<b>121</b>
	<b>APPENDIX D WIND TUNNEL TEST DATA FIRST TEST SERIES</b>	<b>125</b>
	<b>APPENDIX E WIND TUNNEL TEST DATA - SECOND TEST SERIES</b>	<b>144</b>
	<b>APPENDIX F PROPELLER TEST RIG DRAWINGS</b>	<b>149</b>
	<b>APPENDIX G PROPELLER TEST RIG STRESS CALCULATIONS</b>	<b>152</b>

## LIST OF FIGURES

Figure 2.1	Pathfinder propellers designed for 24 400 m altitude flight (NASA, 1995) ....	10
Figure 2.2	Centurion propellers designed for 30 500 m altitude flight (NASA, 1998).....	10
Figure 2.3	The Strato 2C high altitude aircraft (MT-Propeller, 2006) .....	11
Figure 4.1	HALE UAV mission profile .....	19
Figure 4.2	UAV Perseus B propeller [NASA, 1999].....	20
Figure 4.3	Concept drawing of UAV [Monk, 1995] .....	22
Figure 4.4	Initial propeller geometry – radial chord distribution.....	25
Figure 4.5	Initial propeller geometry – radial twist distribution.....	25
Figure 4.6	Radial Reynolds number variation with altitude.....	27
Figure 4.7	Radial Mach number variation with altitude.....	28
Figure 4.8	Iteration history showing reducing induced angle errors .....	29
Figure 4.9	The MH family of propeller aerofoils .....	31
Figure 4.10	Variation in zero lift angle along the propeller radius.....	35
Figure 4.11	Comparison between MH117 and MH121 aerofoil section geometries .....	36
Figure 5.1	Radial chord distribution .....	43
Figure 5.2	Radial twist distribution .....	43
Figure 5.3	Propeller radial lift coefficient distribution during climb phase.....	44
Figure 5.4	Propeller pitch angle variation over flight time.....	45
Figure 5.5	Propeller radial lift coefficient distribution during cruise .....	46
Figure 5.6	Variation in advance ratio over the mission.....	47
Figure 5.7	Predicted thrust coefficient vs. advance ratio for pitch angles from -12 to 12 degrees .....	50
Figure 6.1	Rotation of the aerofoil sections around their quarter chord location.....	53
Figure 6.2	Cross sections through the blade root area showing effect of hub geometry	54
Figure 6.3	Rear view of final blade geometry .....	54
Figure 6.4	Top view of final blade geometry .....	55
Figure 6.5	Final blade geometry shown with respect to the wood blank .....	55
Figure 6.6	Radial distribution of cross sectional area and blade stresses at 1200 rpm .	57
Figure 6.7	Hub shear area shown in red.....	58
Figure 6.8	The Beech wood shear test sample .....	58
Figure 6.9	View of ground adjustable hub section showing root fittings.....	59
Figure 6.10	Conceptual design of propeller test rig .....	62
Figure 6.11	Propeller test rig frame .....	62
Figure 6.12	CAD rendering of propeller test rig installation in 2MWT .....	63
Figure 6.13	Close up detail of flexures .....	65
Figure 6.14	Base plate and test rig cross beam supported by flexures.....	65

Figure 6.15	CAD rendering of the propeller test rig with fairing installed in the 2MWT..	67
Figure 6.16	View of the propeller test rig partial installation in the 2MWT.....	67
Figure 7.1	Measured propeller thrust coefficients for pitch angles of -12 to 0 degrees..	77
Figure 7.2	Measured propeller thrust coefficients for pitch angles of 2 to 18 degrees...	78
Figure 7.3	Comparison of predicted and measured propeller thrust coefficients for pitch angles of -12 to 0 degrees .....	79
Figure 7.4	Comparison of predicted and measured propeller thrust coefficients for pitch angles of 2 to 8 degrees.....	80
Figure 7.5	Comparison between designed and manufactured blade geometries .....	81
Figure 7.6	Cross section through new vertical fairing.....	83
Figure 7.7	Rollers directing the drive belts behind the vertical support .....	83
Figure 7.8	CAD rendering of the propeller test rig with fairing.....	84
Figure 7.9	CAD rendering of the installed new test rig geometry .....	84
Figure 7.10	Prony brake drum mounted on propeller test rig .....	87
Figure 7.11	Motor torque versus measured armature current for various speeds .....	88
Figure 7.12	No-load motor current at various speeds .....	89
Figure 7.13	Comparisons between results of predicted and measured thrust coefficients at pitch angles from -8 degrees to 4 degrees .....	91
Figure A1	MH 112 lift coefficient versus angle of attack.....	103
Figure A2	MH 112 drag coefficient versus angle of attack .....	104
Figure A3	MH 113 lift coefficient versus angle of attack.....	105
Figure A4	MH 113 drag coefficient versus angle of attack .....	106
Figure A5	MH 114 lift coefficient versus angle of attack.....	107
Figure A6	MH 114 drag coefficient versus angle of attack .....	108
Figure A7	MH 115 lift coefficient versus angle of attack.....	109
Figure A8	MH 115 drag coefficient versus angle of attack .....	110
Figure A9	MH 116 lift coefficient versus angle of attack.....	111
Figure A10	MH 116 drag coefficient versus angle of attack .....	112
Figure A11	MH 117 lift coefficient versus angle of attack.....	113
Figure A12	MH 117 drag coefficient versus angle of attack .....	114
Figure A13	MH 121 lift coefficient versus angle of attack.....	115
Figure A14	MH 121 drag coefficient versus angle of attack .....	116
Figure B1	Measured test rig drag against tunnel speed .....	117
Figure B2	Influence of wind tunnel velocity on test rig drag coefficient .....	118
Figure B3	Increase in test rig tare drag with tunnel dynamic pressure.....	119
Figure B4	Variation of test rig drag coefficient with tunnel speed with the new fairing.	120
Figure C1	Thrust cell calibrations at 10 Volts .....	122
Figure C2	Thrust cell calibration differences at 10 Volts .....	122
Figure C3	Second test series thrust cell calibration.....	123

Figure F1	Top Bearing Housing .....	149
Figure F2	Top view of test rig .....	149
Figure F3	Side view of test rig .....	150
Figure F4	Side view of test rig with fairing .....	150
Figure F5	Side view of test rig with fairing, motor and propeller.....	151
Figure F6	Cross section through new test rig fairing .....	151

## LIST OF TABLES

Table 4.1 UAV specifications .....	21
Table 4.2 Propeller design inputs .....	24
Table 4.3 Radial position of aerofoil sections .....	34
Table 4.4 Zero lift angles of aerofoil sections .....	36
Table 4.5 Maximum D/L ratios for the chosen propeller aerofoils .....	38
Table 4.6 Fixed design parameters .....	38
Table 5.1 Final design parameters .....	42
Table 7.1 Test record of first test series.....	76
Table C1 Calibration of Thrust Load Cell at 10 Volts.....	121
Table C2 Determination of gradients and offsets .....	123
Table C3 Calibration of Thrust Load Cell at 12 Volts.....	124
Table D1 (List of wind tunnel test results).....	126
Table D2 -12° Pitch Angle at 1200 RPM.....	127
Table D3 - 8° Pitch Angle at 1200 RPM.....	128
Table D4 - 4° Pitch Angle at 800 RPM.....	129
Table D5 - 4° Pitch Angle at 1200 RPM.....	130
Table D6 0° Pitch Angle at 800 RPM.....	131
Table D7 0° Pitch Angle at 1200 RPM.....	132
Table D8 2° Pitch Angle at 800 RPM.....	134
Table D9 2° Pitch Angle at 1200 RPM.....	136
Table D10 -4° Pitch Angle at 800 RPM.....	137
Table D11 4° Pitch Angle at 1200 RPM.....	138
Table D12 8° Pitch Angle at 800 RPM.....	140
Table D13 4° Pitch Angle at 1200 RPM.....	142
Table D14 12.1° Pitch Angle at 800 RPM.....	143
Table E1: - 8° Pitch Angle at 1000 RPM.....	144
Table E2 -4° Pitch Angle at 1000 RPM.....	145
Table E3 0° Pitch Angle at 800 RPM .....	146
Table E4 0° Pitch Angle at 1200 RPM .....	147
Table E5 4° Pitch Angle at 1000 RPM .....	148
Table G1- Calculation of Blade Tensile Stresses at 1200 rpm .....	153

## LIST OF SYMBOLS

Air density ( $\text{kg/m}^3$ )	$\rho$
Blade element helix angle (Radians)	$\Phi$
Coefficient of Pressure	$C_P$
Coefficient of Torque	$C_Q$
Coefficient of Thrust	$C_T$
Diameter (m)	$D$
Drag Coefficient	$C_D$ or $C_d$
Lift (N)	$L$ or $l$
Lift Coefficient	$C_L$ or $C_l$
Local propeller element blade radius (m)	$r$
Mach number	$M$
Power (W)	$P$
Radius of the propeller blade (m)	$R$
Revolutions per Minute (1/min)	RPM
Revolutions per second (1/sec)	$N$ or $n$
Rotational Speed (Radians/sec)	$\Omega$
Specific Gas Constant for air ( $J/kg/K$ )	$R$
Transition factor	$n$
Thrust (N)	$T$
Velocity (m/sec)	$V$
Subscripts:	
critical	crit
maximum	max
minimum	min
zero lift – as applied to drag coefficient	0

## ACRONYMS

Computer Aided Design/Drawing	CAD
Computational Fluid Dynamics	CFD
Computer Numerically Controlled	CNC
Committee on Extension to the Standard Atmosphere (United States)	COESA
Engineering and Science Data Units	ESDU
Electromagnetic Interference	EMI
Environmental Research Aircraft and Sensor Technology	ERAST
Federal Aviation Requirements	FAR
High Altitude Long Endurance	HALE
Hewlett Packard	HP
National Advisory Committee for Aeronautics	NACA
National Aeronautics and Space Administration	NASA
Non-uniform Rational B-Splines	NURBS
Standardized Exchange of Product – a CAD geometry format	STEP
Unmanned Aerial Vehicle	UAV
Ultimate tensile strength	UTS

# 1. INTRODUCTION

## 1.1. Historical Development of Propeller Design Theories

In 1900 and 1901 Stefan .K. Drzewiecki, a Polish mathematician and mariner presented two papers in Paris on his blade element, or “strip” theory (Carrol, 2005). Based on Bernoulli’s principles they provided a way of determining forces and moments by representing the blade as a number of aerodynamically independent cross-sections. The characteristics of each of these sections were assumed to be the same as an aerofoil at that angle of attack. The main drawback of the theory was that, as the operation of a cross-section was indirectly related to that of a two-dimensional aerofoil, Experimental two-dimensional aerofoil data was thus needed *a priori*.

The Wright brothers were the first of the early aircraft design pioneers to realise that a propeller worked on the principle of a rotating wing generating forward lift as opposed to the previous concept of a propeller pushing the air rearwards (Carroll & Carroll, 2005). Despite their relatively basic understanding of the aerodynamic principles involved their designs exhibited high efficiencies - even when compared to modern designs. While they utilised the blade element theory of Drzewiecki, they realised that it was not able to predict the induced velocities required to produce the correlation between an aerofoil in axial flow and a rotating aerofoil. They realised that it had to be combined with the earlier momentum theory of Rankine and Froude in order to complete the analysis.

In 1903 they had produced a propeller that demonstrated a maximum efficiency of 66% and by 1905 they had achieved an efficiency of 81.5% (Carrol 2005). These efficiencies were not achieved by other designers until after World War I (Ash, 2001) and are high even by modern day standards.

In 1919 Albert Betz published a paper while working as a researcher at the University of Göttingen Aerodynamic Laboratory on minimum energy loss propellers (Betz, 1919). In this paper he illustrated that there was a particular radial propeller blade loading which would minimise the energy loss in the wake. He also showed that the induced power required by a propeller was minimized if the slipstream had the same velocity at all radial points and if each cross section of the slipstream rotated around the rotation axis in a rigid fashion.

Betz followed this with a paper translated into English titled, "The Theory of the Screw Propeller" (Betz, 1922). This work was a summary of the understanding at the time of the flow phenomena around propellers. In particular he mentioned the requirement for a combined blade element and momentum theory that made it possible to evaluate the induced velocity field and therefore predict the inflow conditions assumed by the blade element theory. Betz (1922) also noted that the use of aerodynamic data as used on the wing aerofoils should be used with caution when applied to propellers.

Ludwig Prandtl, a German physicist and a pioneer of subsonic aerodynamics, wrote the appendix to Betz's 1919 paper in which he described an approximate solution to this minimum energy loss, radial force distribution (*Prandtl and Betz, 1919*). He recognised that the slipstream velocity would move at a fixed fraction of the free stream velocity (Larrabee, 1984a). He approximated this fraction using an analogy to the flow between semi-infinite plates moving normal to the free stream in terms of an edge distance / plate spacing parameter. This was the first, approximate attempt at predicting a minimum loss blade loading.

Goldstein (1929) suggested that a design method existed that would produce a family of minimum induced loss propeller designs with different ratios of induced to profile losses depending on the design parameters used. He did not elaborate on this design method any further.

Research into propellers for higher speed aircraft and more powerful engines continued throughout World War II. However the advent of the gas turbine engine and its ability to thrust aircraft to speeds greater than that of sound brought research into the further understanding of the aerodynamics of the propeller to a virtual standstill by the start of the 1950's.

Many years later, due partly to a renewed interest in man-powered flight and the requirement for highly efficient propellers, the relatively simple design method suggested by Goldstein was developed and published (Larrabee, 1979a). He investigated the connection between propeller design utilising lifting line theory with induced velocity distributions being induced by helical trailing edge vortex sheets and Glauert's radially graded momentum theory. He showed that through a combination of these two methods a radial twist and chord distribution could be determined that would result in an optimal circulation distribution.

Larrabee (1979a, 1979b) went on to simplify the resulting method in his paper with small-angle approximations, assumptions of low disc loading as regards to the displacement velocities and disregarding the viscous terms in the induced velocity expressions. He stated that his method would be most accurate when applied to “relatively lightly loaded” propellers.

The design and analysis methods presented are relatively simple and require minimal computational power making them particularly suitable for use in the initial phase of an aircraft design.

## **1.2. Motivation**

The design and analysis of a propeller that provides sufficient thrust for take off at sea level and then operates efficiently at high altitude is not a trivial exercise. A propeller designed for cruise flight at altitudes this high with air densities a fraction of that at sea level will typically not perform well at lower altitudes. Flight in the relatively thin atmosphere at high altitudes where the combination of low Reynolds numbers and high Mach numbers place limitations on the performance of the aerofoil sections.

Aircraft flying at a constant indicated airspeed while ascending experience an increase in true airspeed with increase in altitude. The relatively large amount of blade twist required due to the high true airspeeds at high altitude reduce the performance at low altitude and often results in large portions of the blade operating far from their optimum angles of attack at the lower mission altitudes. It is thus important that the performance of the aircraft is correctly modelled over its large operating envelope.

An investigation into the initial design of such a propeller needs to be undertaken early in the design process to obtain first iteration performance figures and feasibility data using relatively quick design and analysis tools such as those presented here. The design of such a propeller may ultimately be derived from a commercial propeller design code.

## **1.3. Objectives**

The primary objectives of this research were the evaluation of the capabilities of a propeller design and analysis methodology as applied to the initial design of a propeller of a High Altitude Long Endurance (HALE) Unmanned Aerial Vehicle (UAV) and an experimental verification of its accuracy.

An evaluation was carried out of the capability of the minimum induced loss method proposed by Larrabee (1979a) to design a propeller that was capable of performing efficiently over the range of conditions encountered during a HALE UAV mission. Likewise the accuracy of his analysis method, based on radially-graded momentum theory, was evaluated at flight conditions far removed from the initial propeller design point and over the range of blade pitch angles required by the mission.

A propeller was designed for application over a particular HALE UAV mission in order to evaluate the abilities of the design code. Its performance was assessed via a UAV mission simulation. The assessment of the accuracy of the analysis method at predicting performance both at the design point and at evaluating the magnitude of the losses in off-design point was carried out through wind tunnel tests using a reduced scale propeller manufactured for the purpose.

An electric motor powered, two-component propeller test rig was developed in support of this work. The test rig was equipped with a custom designed torque transducer and rotary speed sensor and the propeller thrust was measured independently via a calibrated load cell. The propeller rotational speed was controlled by a three phase speed controller at speeds set by the operator. A streamlined fairing covered the vertical support strut over the airflow impingement region to reduce the effect of its drag on the accuracy of the readings.

#### **1.4. Roadmap**

This dissertation explores the historical evolution of propeller design theories leading up to the theoretical optimal Minimum Induced Loss propeller design methodology. As the design methodology being considered is for a high altitude application, the propellers on a number of similar aircraft were examined as was the wind tunnel testing literature with respect to test rigs, balances and wind tunnel corrections applicable.

The applicability of this particular method of propeller design to high altitude flight was then investigated along with the simplifying assumptions and an initial concept propeller was designed for the cruise condition at which the aircraft would spend much of its time. The operating point conditions along the blade length were determined and the choice of blade aerofoil sections and aerofoil analysis code made. The optimal minimum induced loss propeller was chosen from the mission analysis of a particular UAV.

Having demonstrated that Larrabee's design method is capable of producing a propeller that performs satisfactorily over the mission, the focus of the dissertation shifts to the assessment of the accuracy with which the analysis method is capable of predicting its performance. A model of the propeller was manufactured and a propeller test rig constructed and installed into an open section wind tunnel.

The expected performance of the scale propeller was predicted and is compared with wind tunnel results from two wind tunnel test series. Comments and recommendations are made based on these results.

## **2. LITERATURE SURVEY**

In addition to the historical surveys, various literature was sourced that was relevant to the minimum induced loss design and analysis methods of Larrabee (1979), propellers designed for high altitude flight, wind tunnel testing of propellers, test rigs and balances.

### **2.1. An Introduction to Larrabee's Design and Analysis Methods**

A detailed description of Larrabee's design and analysis methods are not presented here as they can be found, including their derivations, in his publications (Larrabee, 1979a, 1979b).

#### **2.1.1 Larrabee's Minimum Induced Loss Design Method**

Propellers designed using the induced loss method have radial blade loadings analogous to that of elliptically loaded wings and experience a uniform induced velocity radially across the blades. Implicit in the assumption of a "relatively lightly loaded" propeller as mentioned by Larrabee (1979a) is the fact that the axial velocity change through the propeller is small in comparison with that of the free stream velocity,  $V$  and the induced velocities are assumed to be half that of the vortex sheet in the fully developed slipstream. Knowing the number of blades, shaft rotation speed and flight speed allows one to determine the wake geometry and hence the normalised circulation for minimum induced loss can be calculated (Larrabee, 1979a).

The "light loading" assumption is typical of many of the methods used in the design of propellers for light aircraft (Goldstein, 1929; Glauert, 1926, 1943; and Borst, 1973) and as will be shown later, the propeller disc loading to which this design is being applied is an order of magnitude lower than that of the typical light aircraft.

The performance of a propeller can be described in terms of non-dimensional coefficients: thrust coefficient, power coefficient and advance ratio. The efficiency of the propeller can be calculated from these three coefficients. These coefficients are typically used in the comparison of propellers of different scales tested under different operating conditions as will be the case in this work.

The coefficients presented here are (Glauert, 1943):

$$\text{Thrust coefficient} \quad C_T = T/(\rho n^2 D^4) \quad (2.1)$$

$$\text{Power coefficient} \quad C_P = P/(\rho n^3 D^5) \quad (2.2)$$

$$\text{Advance Ratio} \quad \lambda = V/nD \quad (2.3)$$

$$\text{Efficiency} \quad \eta = V/nD (C_T/ C_P) \quad (2.4)$$

It should be noted that throughout this work, the 70 % radial point is used as the blade pitch angle reference point and a radial position is typically defined as the (non-dimensional position of the point of interest along the propeller blade.

### 2.1.2 Larrabee's Graded Momentum Theory Analysis Method

Although designed for a particular design point in the UAV flight envelope, the propeller performance must be analysed at other points in the aircraft flight envelope. In the case of the HALE UAV these points can be relatively far removed from the design point. Larrabee (1979a) used a radially graded momentum theory method that is simple to implement, using the optimal propeller's radial loading to provide this analysis. Without this loading the analysis method would produce finite amounts of lift at the blade tips as it ignores the aerodynamic effects of the neighbouring blades.

This analysis routine requires an initial estimate of locally induced inflow angle to the blade at each radial station. The axial velocity induced by the radial lift distribution is calculated and the difference between the two values calculated. A new estimate of the induced angle of attack is made using a fixed fraction of the difference to ensure stable convergence and the iteration continued until the difference between successive estimations has decreased to an acceptably small value.

The analysis routine of Larrabee (1979a) was entered into a spreadsheet to provide an insight into the values of the variables and to identify limitations in the convergence at performance points far displaced from the design point. In particular convergence rates at each radial station could be monitored for all flight cases and in particular for variations in pitch angle. This functionality was added to allow for the evaluation of the effects of the large pitch angles expected in flight.

One of the issues being evaluated here is the applicability of this analysis method to analysing propellers far from their design point where the assumed radial grading can be far removed from that actually experienced in flight. The limitations of the method will be evaluated during the wind tunnel tests.

## **2.2. Literature Survey on High Altitude Propellers**

The advent of high altitude, low speed aircraft for reconnaissance or atmospheric research had also brought about a renewed interest in the topic of propeller design for efficiency at high altitudes. Such propellers have been the method of choice for propulsion of a number of high altitude aircraft such as the Egrett (1987), Condor (1988), Pathfinder (1993) and Strato 2C (1995). In the mid 1990's the NASA ERAST (Environmental Research Aircraft and Sensor Technology) programme office contracted the construction by Aurora Flight Sciences of Perseus A and B (1993 and 1994) high altitude propeller driven UAVs. AeroVironment was similarly contracted to provide the Pathfinder Plus (1998), Centurion (1998) and Helios (1999) high altitude aircraft designs all of which utilised propellers driven by electric motors (Goebel, 2008)

Not surprisingly little information was found on the designs of the aircraft propellers as those details are seldom published, even more so for unique aircraft. However in his paper on the development of the Condor High Altitude Long Endurance UAV, Colozza (1998) describes the design methodology followed in the design of the propeller. Unfortunately some of the technical details of this report have been removed due to USA export restrictions. The information sourced on the high altitude propeller designs for the Pathfinder, Centurion and Helios UAVs and the Strato 2C aircraft are discussed in more detail below:

### 2.2.1 Pathfinder, Centurion and Helios propellers

The design of the propellers for the Pathfinder Centurion and Helios UAVs are of a fixed pitch design due to the stringent low mass requirements of an airframe that relies on solar power for propulsion. The author was fortunate enough to ascertain directly from AeroVironment personnel during a visit that the required performance was achieved through the use of blades of wider than usual chords with relatively low thickness aerofoil sections. The wider chords result primarily from the matching of the required engine power to that of the propeller at the very low atmospheric density at high altitudes and the typically lower design lift coefficients chosen for aerofoils intended for use at low Reynolds numbers.

The propeller design was carried out by National Aeronautics and Space Administration (NASA) engineer Dr A Hibbs using the minimum induced loss method with the poor off-design point performance being accepted as a compromise against the advantages of the resultant low mass of the propellers (Bieryla, 2007). In a similar fashion to the current work, these propellers were required to perform at low altitudes for a small fraction of the total mission time and as such the relatively poor performance attained at low altitudes was deemed an acceptable penalty in order to produce the required performance at altitude.

The propeller visible in Figure 2.1 was designed for flight up to 24 400 m altitudes but was too inefficient for an attempt on the 30 500 m altitude world record. The propellers designed for that altitude are shown in Figure 2.2 with their significantly wider chords being visible in this view.



Figure 2.1 Pathfinder propellers designed for 24 400 m altitude flight (NASA, 1995)



Figure 2.2 Centurion propellers designed for 30 500 m altitude flight (NASA, 1998)

### 2.2.2 Strato 2C propellers

The Strato 2C high altitude aircraft (Figure 2.3) flew its maiden flight in 1995. The aircraft was designed to perform at altitudes of up to 24 000 m but it never attained that altitude, achieving only 18 500 m on its final flight. In their aerodynamic assessment of the aircraft, Schawe et al. (2002, pp. 43-51) showed that at altitudes above 18 500 m the propeller performance was severely reduced through flow separation starting at the 60% radial

position and that at higher altitudes this would extend out to the 80% radial position. Their evaluation showed that the propeller would have operated at a propulsive efficiency of 91% at 12 000 m and 18 500 m but this had reduced to 87% at 22 000 m and 66% at 24 000 m. While the poor high altitude propeller performance was not the sole reason for the lower than expected aircraft performance (there were other airframe related aerodynamic deficiencies) it was a major contributing factor.



Figure 2.3 The Strato 2C high altitude aircraft (MT-Propeller, 2006)

Schawe et al. (2002) also noted in their report that the aerofoils used on the aircraft propellers were not sufficiently carefully designed for the high Mach number, low Reynolds number conditions experienced at 24 000 m. Also mentioned was that the ISES aerofoil analysis code used by the authors, while possibly one of the more accurate available in 2001, could have errors as high as 20% to 30% in the performance predictions at the high Mach numbers and low Reynolds numbers typical of that environment.

While the atmospheric conditions at 24 000 m are more extreme in Mach and Reynolds number effects than that at the 15 000 m cruise altitude of the current work, cognisance was taken of the aerodynamic issues and the limitations of the aerofoil performance prediction methods in this flight regime.

## 2.3. Investigation into the Wind Tunnel Testing of Propellers

To model the performance of the predicted propeller in the wind tunnel equivalence must be met for certain parameters. In particular modelling identical advance ratios (the ratio of airspeed along the axis of a propeller to the speed of the blade tip) for the predicted and tested propellers ensures that the angle of attack at each radial position is consistent with that of the full scale propeller ensuring that the measured performance is comparable.

### 2.3.1 Propeller test rigs

In his work on large scale propeller testing Barber (1983 and 1984) describes the propeller test rigs designed for use at the National Research Council of Canada in Ottawa for validating propeller performance estimates and evaluating the effects of propeller geometries and excrescences. See Figure 2.4.



Figure 2.4 Hartzell propeller on NRC 9M tunnel test rig (Barber, 1983)

Testing at full scale was considered essential to avoid Reynolds number effects and to allow accurate representation of design features that typically influenced installed performance. The maximum tunnel speed of 105 knots (54 m/s) allowed accurate representation of flight conditions for only the aircraft takeoff and climb phases. Cruise conditions were simulated non-dimensionally at reduced propeller rotational speed although the compressibility effects could not be correctly modelled in this case.

The tunnel flow velocity was measured via a dynamic probe with the static port mounted in the ceiling in the plane of the propeller. This was demonstrated to yield a free stream velocity independent of the propeller loading. A pitot-static calibration probe mounted at the location of the propeller was used to calibrate the ceiling static port. Corrections for the solid blockage effect of the propeller and nacelle were still required.

The nacelle fore body, spinner and propeller were mounted together on the main balance so the buoyancy forces arising from interaction between these components were effectively cancelled. The net thrust measured also includes the reduction due to the increased forward nacelle skin friction drag caused by the slipstream and swirl effects. According to Barber (1983) independent estimates judged this additional drag to have been negligible.

Any model supports inserted into a wind tunnel test section affect both the free flow of air and cause drag themselves, these are called *tare* and *interference* factors and corrections are required to the force and moment readings to compensate for them.

The nacelle tare drag was determined prior to mounting the propeller. A dummy spinner without any cut outs for the blades was fitted to the forward nacelle and the drag determined at maximum tunnel speed. A similar approach has been adopted in the current work.

### 2.3.2 Balances

In the majority of the literature on wind tunnel tests the test propeller was typically mounted on the main balance in the wind tunnel or on a balance designed to fit the test rig. The lack of information on propeller test rig balances did not hinder the current research as the limited project budget precluded the design and manufacture of a custom balance for the propeller test rig. A different approach was adopted in which the rig was

pivoted around a transverse axis and a standard load cell was utilised for thrust measurement.

### 2.3.3 Test Techniques

Various references were obtained on wind tunnel test techniques for propellers, all of which covered the theory of testing of propellers although only Glauert (1959), Rae and Pope (1984) provided indications of the correction factors.

Wind tunnel testing techniques described in Rae and Pope (1984) were followed where relevant.

### **3. APPLICABILITY OF LARRABEE'S METHOD TO THE HALE UAV DESIGN**

At the operational altitude of 15 000 m the relative air density is 12% of that at sea level and the ratio of true airspeed to equivalent airspeed is three times that at sea level. The propeller is therefore required to adjust pitch through a large angular range to absorb the power of the engine as the aircraft increases its true airspeed at a relatively constant equivalent airspeed with increase in altitude. The relatively large amount of blade twist required due to the high true airspeeds at high altitude reduce the performance at low altitude and often results in large portions of the blade operating far from their optimum angles of attack at the lower mission altitudes.

The applicability of Larrabee's methods to provide an efficient design and the analysis of a variable pitch propeller system with the operation of the blade at angles of attack far from those of the design point needed to be evaluated in order to ensure that a fair assessment could be made. Following a rigorous approach to the evaluation of its applicability to the task at hand, each of the simplifying assumptions in Larrabee's method were analysed with a focus on the current design requirements.

#### **3.1.1 Low disc loading assumption and Small Angle Approximations**

Larrabee (1979a) makes no mention of any formal definition of "low disc loading" and no definitive reference could be found in the literature as to what quantifies this parameter. The current HALE UAV concept requires a large diameter propeller for its high cruise efficiency and has a relatively low drag coefficient of 0.0200 (Monk, 1995) The resultant disc (thrust) loading of  $56 \text{ N/m}^2$  needs to be compared against the range of typical light aircraft.

For comparison purposes the disc loadings of a typical two seat and a four seat light aircraft popular at the time of Larrabee's papers were calculated. Disc loadings of approximately 400 and  $1000 \text{ N/m}^2$  for the Piper PA-38 Tomahawk and Piper PA-140 Cherokee respectively were calculated. As the current UAV disc loading is approximately an order of magnitude smaller than that of the light aircraft for which this approach is

applicable it was considered to be within the “low disc loading” assumption referred to by Larrabee (1979a).

Larrabee (1979a) uses his “light loading” assumption to simplify a number of equations in his method. Assumptions such as equating the slipstream radius to the propeller radius and the slipstream helix angle to the propeller helix angle in particular would apply best to a very low disc loading, and increasing the disc loadings would make these assumptions increasingly inaccurate (Adkins and Liebeck, 1983).

Based on his assumption of a low disc loading, Larrabee (1979a) also makes a number of small angle approximations to simplify the displacement velocity calculations. These small angle assumptions limit the applicability of his method to the design of propellers with lower disc loadings as indicated (and improved on) by Adkins & Liebeck (1983).

There are three assumptions behind the small angle approximations used to simplify the equations used in the design methodology. The first assumption is that the radius of the slipstream tube, or ‘vortex filaments’ as described by Larrabee (1979a), at each blade element is approximately equal to the propeller blade element radius i.e. that there is almost no contraction of the propeller wake. The second assumption is that the filament helix angle is equal to the helix angle followed by the corresponding propeller blade element. The third assumption consistent with the small angle approximations is that the displacement terms of the elemental helical wake can be simplified into functions of the elemental advance ratio,  $V/\Omega r$ .

### 3.1.2 Exclusion of Viscous Terms

Viscous terms are excluded in Larrabee’s determination of the induced velocities. Once again this assumption is sufficiently accurate for the design of propellers of low disc loading with aerofoils operating near their optimum lift/drag point. The exclusion of the elemental drag term does result in the performance predicted at the propeller design point differing from that produced by the propeller at that design input by a small amount.

Due to the very low disc loadings of the current configuration, the loss in accuracy through this assumption is expected to amount to a small percentage of the final design performance.

The error introduced at each blade element by this simplification is equal to  $\sin(\Phi)(D/L)$  (Adkins and Liebeck, 1983).

Assuming the typical design blade element D/L ratios of over 100 and helix angles of the order of a few degrees (for lightly loaded propellers), this error would thus over predict the performance by less than one tenth of a percent at the design point.

### 3.1.3 Applicability of a Point Performance Design Method

Larrabee's design algorithm is typically used to design a propeller to exhibit minimum induced losses at a particular point in an aircraft's flight envelope. The range of operational conditions experienced by the current propeller over the HALE UAV mission removes it far from any particular design point, hence the need to evaluate the design method's applicability.

The vast majority of the mission time is however flown in the cruise phase where flight takes place over a relatively small speed range and at a constant altitude. It is thus expected that the final propeller geometry would be based on design specifications close to those of the HALE UAV cruise flight condition.

## 4. INITIAL HALE UAV PROPELLER DESIGN AND ANALYSIS

The optimal design of a propeller that is to perform over such a large range of altitudes and power settings cannot be accomplished in a single iteration. The design requirements need to be analysed and an *a priori* design completed to determine the local flow conditions on the propeller blade. Based on these results, a candidate aerofoil or series of aerofoils must be chosen for the conditions predicted at the various radial locations on the blade and their aerodynamic characteristics determined over the expected Reynolds number and angle of attack range.

### 4.1. Propeller Design Requirements Specification

Typical UAV propeller design requirements focus on maximising the UAV mission performance. The UAV performance requirements define the required propulsive power over the various phases of its mission. In this case satisfying the requirement to fly over a large range of altitudes requires a thorough knowledge of the relevant atmospheric characteristics from sea level up to 15 000 m.

Other constraints on the propeller design solution space are imposed by the geometry of the airframe. In this particular case a twin-boom configuration limits the maximum diameter of the propeller. There are additional requirements of high Mach number and low Reynolds number performance demanded of the blade sections. These require an initial investigation into the feasibility before the detail design can be initiated.

As the focus of this work is on the capabilities of the propeller design and analysis methods little effort is applied to the structural, aero-elastic or mass properties of the propeller blade except that required for safe testing of a scale wind tunnel model.

#### 4.1.1 UAV Mission Description

The UAV mission description is summarised in Figure 4.1 into four flight phases. These are:

1. Assisted acceleration from standstill at sea level to an airspeed of 27 m/s. This is 1.3 times the predicted stall speed of 21 m/s – a typical speed for the climb phase.
2. Climb to a cruise altitude of 15 000 m at maximum climb rate to minimise flight time in commercial airspace. A minimum climb rate of 5m/s at sea level and 1 m/s at 15 000 m must be attained.
3. Cruise at 15 000 m altitude for maximum range on an “out-and-return” course
4. Descend, approach and land

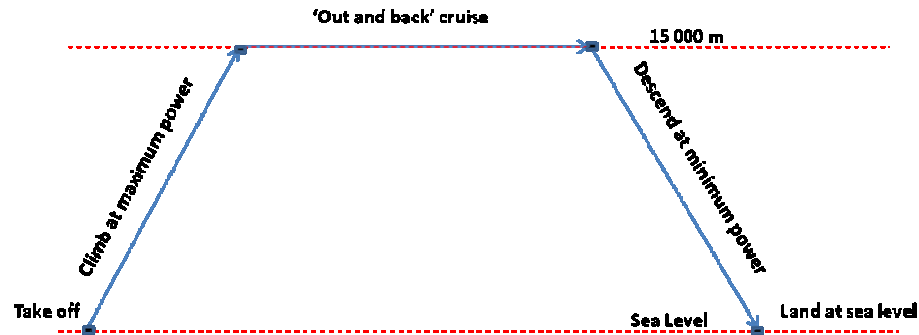


Figure 4.1 HALE UAV mission profile

Note that the cruise flight portion of the mission is an “out and return” course at a constant altitude typically the flight velocity is varied to maximise the airframe efficiency with the reduction in weight over the mission.

The descent and landing phases use an insignificant portion of the fuel as the engine is typically at a low throttle setting for the descent due to the high airframe efficiency. The total fuel usage on the descent and landing phase was estimated at 4 % of total fuel. This amount would not vary significantly with propeller design due to the low power settings required and indeed the propeller would typically not be providing any thrust. As such the descent, approach and land phase was not modelled in the mission analysis except through the assumption of an additional 4% fuel fraction remaining over the normal reserves.

It is assumed that there are no wind or gust effects at any altitude in the mission profile to simplify the design requirements. Maximising range requires flying at airspeeds that are dependent on the local wind strength and direction that may not be optimal for the airframe. The additional power expended flying into the wind is typically more than that saved on the return leg due to the non-linear relationship between the airframe drag and airspeed.

#### 4.1.2 UAV Performance

The HALE UAV airframe chosen for this study was based on a study previously carried out by the author (Monk, 1995) to determine the optimal configuration and sizing of an 18 m span HALE UAV. The work included parametric sizing of the engine and propeller through the application of various empirical methods. The overall propulsive efficiency was at that time estimated with no detailed analysis of the actual design of the propeller. As the original work was classified confidential so as to protect the original airframe's performance requirements, an approximate set of specifications has been used in this work.

A maximum take off mass of 750 kg was assumed including 100 kg of usable fuel before reserves. This includes the 4% provision for the descent and landing phases. The chosen power plant was a Rotax 914 UL four stroke aircraft engine turbocharged to maintain a constant power of 59.6 kW (80 hp) from sea level to 15 000 m as implemented on the Perseus B UAV, Figure 4.2. (Goebel, 2008). The fuel consumption values of 0.419 litres per kW per hour were obtained from the Rotax 914 technical specifications (Rotax, 2009).



Figure 4.2 UAV Perseus B propeller [NASA, 1999]

The UAV would be assisted in the take-off phase to a safe climb speed of approximately 27 m/s, 30% above its predicted stall speed. This is the minimum airspeed at which steady rate of climb is to be measured according to the Federal Aviation Regulation on En-route Climb or Descent (Federal Aviation Regulations, 1996). The flight speed range within which the propeller had to operate was thus defined to be from 27 m/s to maximum cruise speed.

The choice of gear ratio between the engine and propeller was not fixed at this point to allow more flexibility in determining the final design solution.

The specifications for the UAV are summarised in Table 4.1. The aspect ratio, maximum lift coefficient, Oswald efficiency factor and  $Cd_0$  were obtained from (Monk, 1995).

Table 4.1 UAV specifications

Airframe Mass	750	kg
Available Power	59.600	kW
Wingspan	18.0	M
Wing Area	16.2	m <sup>2</sup>
Aspect Ratio	20.0	-
$C_{l_{max}}$	1.65	-
$Cd_0$	0.0200	-
Oswald Efficiency	0.80	-
Specific Fuel Consumption	0.419	l/kW/hr

#### 4.1.3 Propeller Design Constraints

When designing a propeller for a required mission performance for a given airframe, the airframe geometry and power plant choice also place constraints on the design of the propeller.

The UAV configuration consisted of a twin-boom, 18 m span wing and rear mounted engine driving a “pusher” propeller between the booms. The separation distance of three metres between the booms limited the diameter of the propeller to a practical limit of 2.8 m. The ground clearance requirements of the airframe at take-off attitude dictated a two-blade or folding propeller design to meet these requirements. A non-folding two-blade

propeller was chosen. The propeller would be restrained horizontally until the UAV had been towed into the air at which point in time the propeller would be allowed to rotate, a method used with success by Aurora Flight Sciences on their Perseus B UAV (Goebel, 2008).

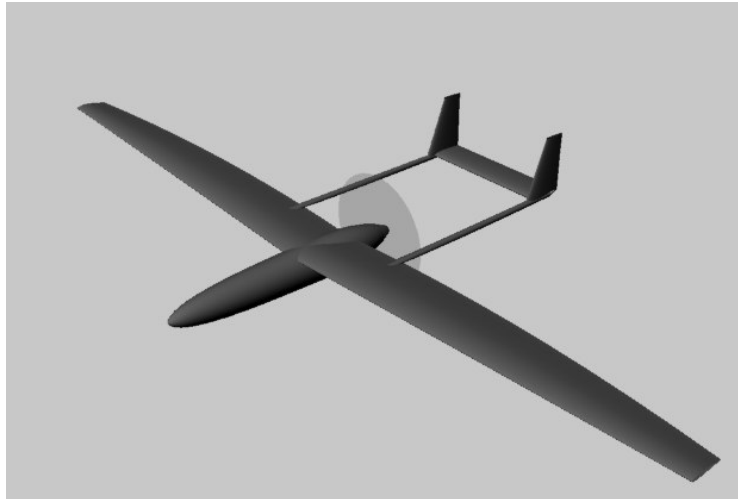


Figure 4.3 The HALE UAV concept layout

The UAV was assumed to have a variable pitch hub capable of allowing rotation of the propeller through the large range of pitch angles required to match the true airspeed over the large change in altitudes.

Large propeller diameters typically result in relatively high blade root structural loads. The structural requirements of the propeller blades normally calculated as part of the design process, do not form a formal part of this study whose focus is on the investigation into the use of Larrabee's methods although mention will be made later of the propeller's structural feasibility.

The formal mass and performance trade-off studies typically carried out to evaluate the degradation in performance of the aircraft due to the additional mass of the pitch change mechanism compared with the lower mass but lower potential performance of the fixed pitch propeller similarly fall outside of the scope of this work. The structural stress predictions and vibration modal analysis are likewise not covered here.

#### 4.1.4 Atmospheric Modelling

The UAV's mission profile requires flight from sea level into the tropopause. Inherent in the design process is an understanding and modelling of the atmospheric conditions from sea level up to these altitudes. The atmospheric conditions used in all the calculations were based on the standard atmosphere equations adopted by the United States Committee on Extension to the Standard Atmosphere (COESA, 1976).

## **4.2. Initial Propeller Design and Analysis**

The design approach adopted in this study specifically utilised the minimum induced loss propeller design method, exactly as suggested by Larrabee (1979a). This was used to design a propeller that would maximise range while meeting the climb rate requirements over the UAV mission. The second part of this investigation is the evaluation of the capability of Larrabee's proposed analysis method to predict the performance when operating far from the design point both in pitch angle and in flight conditions.

### **4.2.1 Initial Propeller Design**

Larrabee's design method requires as input variables propeller diameter, engine power, velocity, root and tip aerofoil design lift coefficients and air density. Some of these variables are fixed by the design of the UAV (propeller diameter) and some are varied in the design process. The design engine power, altitude and velocity input variables are not fixed by the airframe power plant maximum power, final operational altitude or velocity but intermediate values will be evaluated in order to produce a propeller capable of operating optimally over the whole mission. It is likely that the optimal choice of values for these variables will be close to those of the cruise phase but it is unlikely that a propeller designed solely for the cruise phase will be optimal for the mission. What is implicit in the above is that the aerofoil characteristics are known and in the case of the HALE UAV that these characteristics are known at various Reynolds numbers.

In order to predict the performance of the propeller designs, the characteristics of the aerofoil sections were required over the predicted range of operating conditions experienced during the mission. Determining those operating conditions typically require prior knowledge of the propeller geometry as the chord and rotational speed determine the Reynolds numbers for a given altitude. The Mach number is derived from the vector sum of the blade rotation speed and forward speed at each (non-dimensional) radial position divided by the speed of sound at the particular atmospheric conditions and is independent of the blade geometry.

An initial propeller design was carried out at the design point of mid-cruise condition at 50% fuel load corresponding to conditions similar to those which the UAV would spend a large percentage of the mission. It was assumed at the time that the propeller designed could be expected to be close to the final propeller design.

In order to design the initial propeller for the purposes described above and to investigate the sensitivity of the design to the choice of the input parameters, a parametric study was conducted through the implementation of Larrabee's design method in a Microsoft Excel® 2000 spreadsheet.

The individual aerofoil sections were assumed to be operating close to their optimal angle of attack at the design point (the cruise phase) i.e. that they would be operating at their optimum lift/drag ratios. The initial design local lift coefficient at each radial point was chosen to be a linear variation from 1.2 at the root to 0.6 at the tip, chosen to correspond with the maximum efficiency of the various thicknesses of the Clark-Y aerofoil. The Clark-Y aerofoil is commonly used as a propeller aerofoil, thickened as required at the blade root for structural reasons and thinned at the outboard radial stations due to the high local Mach number (Welch, 1979). A drag-to-lift ratio of 0.005 was initially assumed for all blade sections as a conservative estimate of the efficiency of aerofoil sections operating near their design point. Note that Larrabee's method used "drag-to-lift" ratios not the more customary "lift-to-drag" ratio.

A reduction gear ratio of 3.3 was chosen to keep the tip aerofoil section of the 2.8 m diameter propeller from reaching Mach 0.8 at the maximum engine speed of 5800 RPM. A cruise power requirement of 21 kW was calculated for the minimum power speed (maximum endurance factor) of approximately 50 m/s at 15 000 m based on the performance data of the UAV.

The propeller design inputs are listed in Table 4.2:

Table 4.2 Propeller design inputs

Power	21.0 kW
Drive ratio	3.3
Radius	1.4 m
Velocity	50 m/s
Altitude	15 000 m

No. Blades	2
Design lift coefficient range	Linear decrease from 1.2 at 0.1 r/R to 0.6 at blade tip

The initial propeller blade geometry produced by the parametric propeller design and analysis spreadsheet using these design inputs is illustrated as a radial chord distribution (shown as a ratio of chord to blade radius) in Figure 4.3 and radial twist distribution in Figure 4.4 against blade radial position.

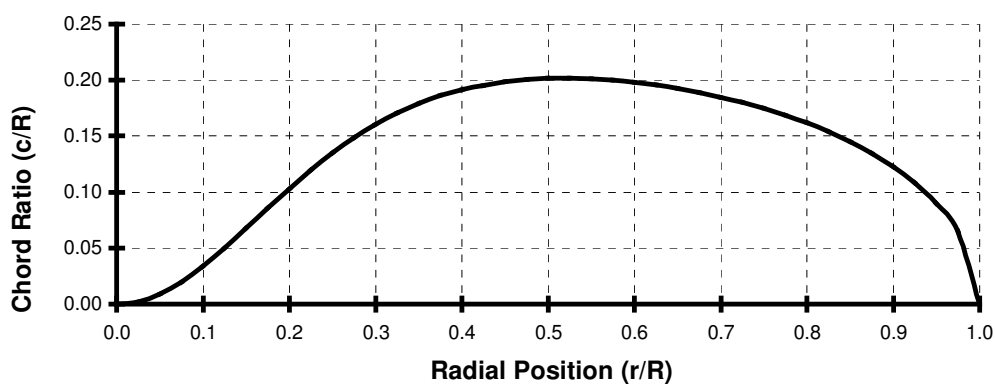


Figure 4.4 Initial propeller geometry – radial chord distribution

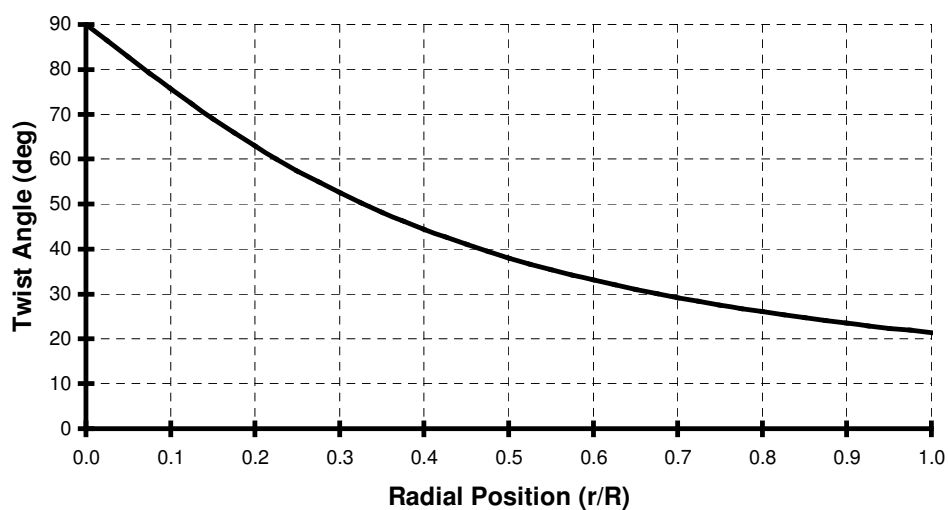


Figure 4.5 Initial propeller geometry – radial twist distribution

The relatively wide chord of the blade is typical of propellers designed for high altitude application as previously noted. The radial twist distribution starts at 90 degrees, as would be expected for the blade root, progressing to a relatively large angle of over 20 degrees due to the high true airspeeds flown by the UAV at high altitudes.

The physical geometry of this propeller is not required at this point in time. All the information needed to determine the local flow conditions can be derived from this information and the aerodynamic data from the program output files.

The local flow conditions at various locations along the blade were predicted at various altitudes along the mission profile. It is interesting to note that even with a relatively large propeller diameter and high rotational speeds, no Reynolds numbers higher than 2 million were predicted as illustrated in Figure 4.5. Above an altitude of 8 000 m Reynolds numbers below one million were experienced over the whole blade. These are relatively low numbers for the efficient operation of the blade aerofoils.

At 15 000 m altitude the whole of the initial propeller blade is operating at a Reynolds number less than 500 000. This is a region of largely non-linear behaviour that requires blade aerofoil section characteristics to be determined with respect to the relevant Reynolds number.

At the propeller blade root the Reynolds numbers approach zero due to the theoretical local chord diminishing to zero however the influence of this area on the overall blade efficiency is relatively small due to its low loading and small distance from the centre of rotation. The convergence of the analysis code was expected to be limited by the non-linear aerofoil characteristics at these low Reynolds numbers.

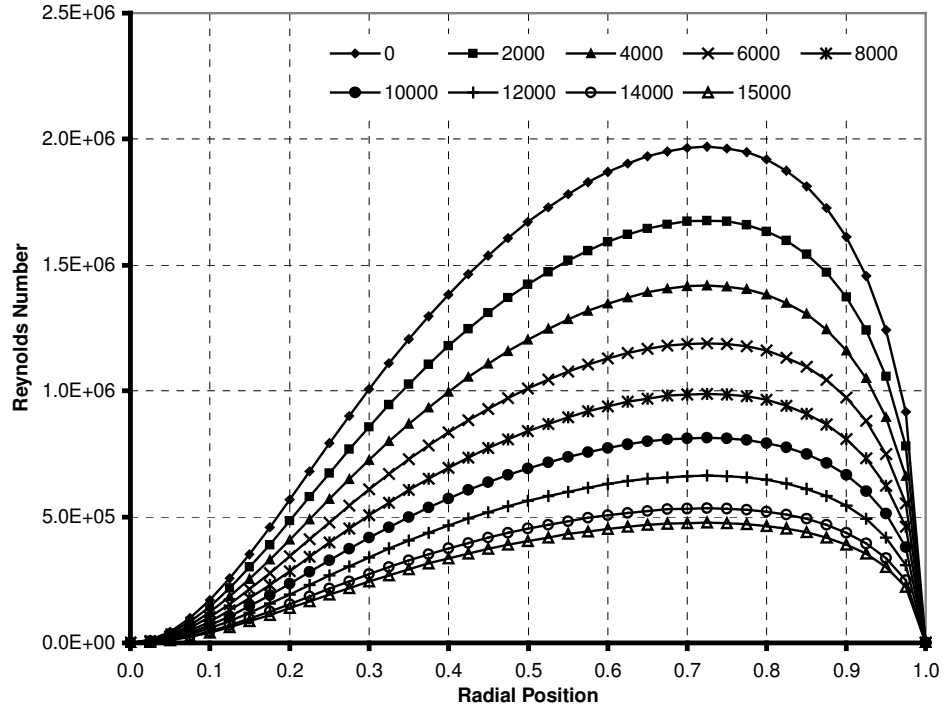


Figure 4.6 Radial Reynolds number variation with altitude

The local Mach number is a linear function of radial position for a given rotational and forward speed. The tip Mach number exceeds 0.8 in this simulation due to the vector sum of the tip velocity and the UAV flight speed (Figure 4.6). As there are currently no aerofoils assigned to this propeller, this is acceptable. The actual tip Mach number had to be monitored during the design iterations of the final propeller.

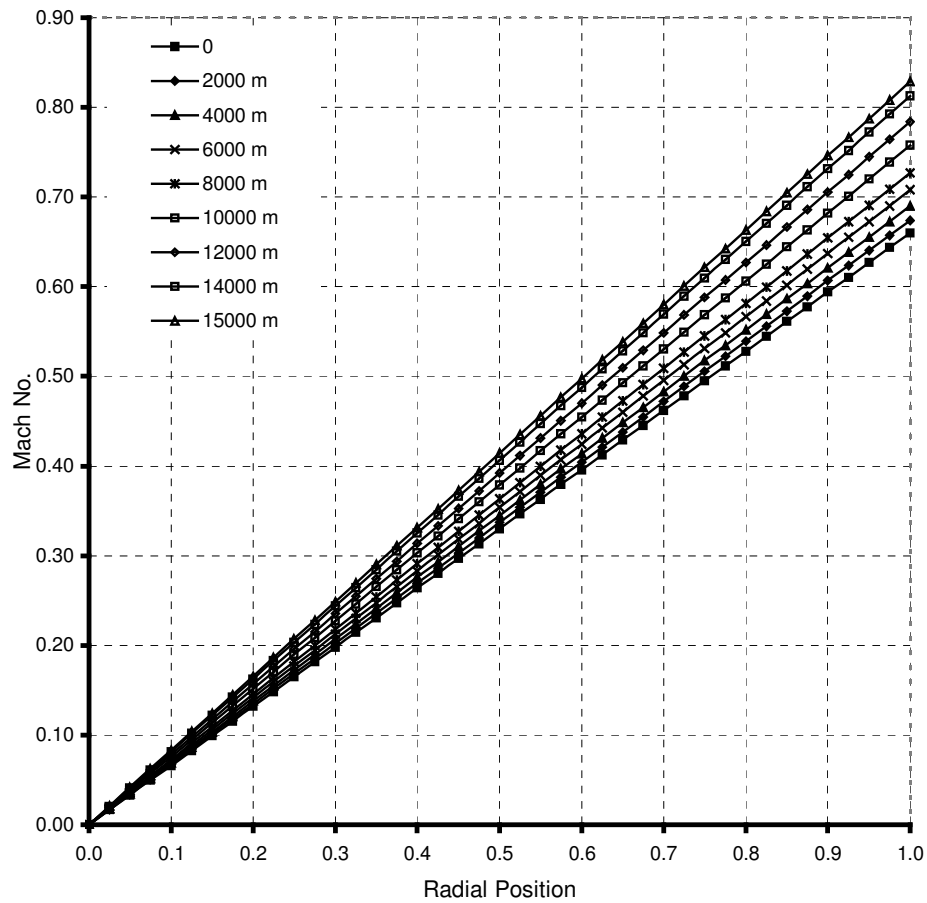


Figure 4.7 Radial Mach number variation with altitude

#### 4.2.2 Initial Propeller Analysis

Larrabee's radially graded momentum theory method was used to predict the performance when operating far from the design point both in pitch angle and in flight conditions. At these points there are a number of parameters whose values fall outside of those assumed in Larrabee's method.

During the initial analysis process difficulties with obtaining convergence to a solution in the off-design cases were observed and through investigation better understood. In particular when the pitch angle was altered to a higher angle of attack where large portions of the blade were stalled the method was unable to converge as rapidly as when the angle of attack was reduced. This was particularly noticeable at the root of the blade.

Figure 4.7 illustrates the convergence history of a 2.8 m diameter two-bladed propeller designed for flight at 15 000 m with a power of 20 kW at 50 m/s operating at that design point but with a pitch angle of 4 degrees above that required by the original design. It can be seen that within five iterations the error over the outboard 90% of the blade is less than two degrees.

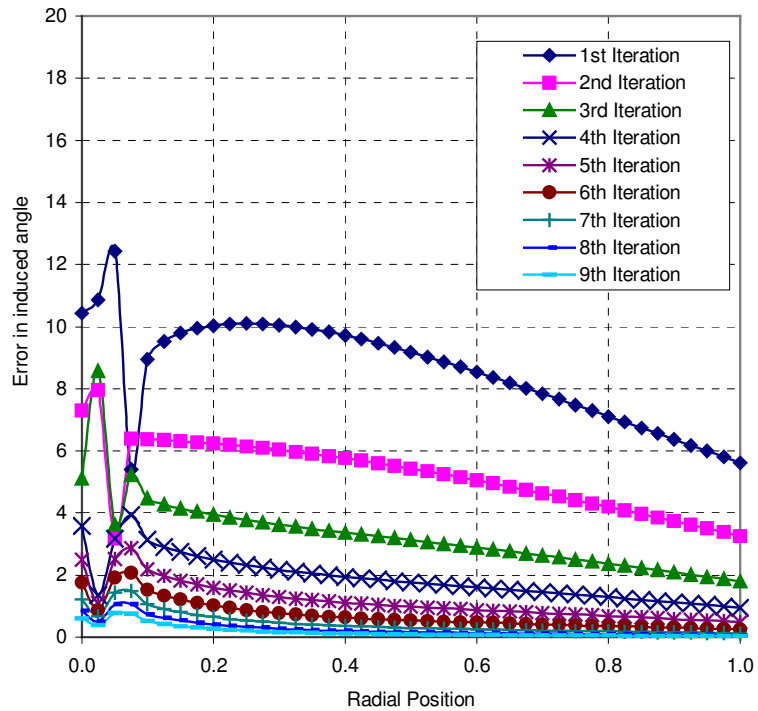


Figure 4.8 Iteration history showing reducing induced angle errors

The convergence of the radial estimation error in the induced angle of attack was monitored in the spreadsheet after each iteration.

### **4.3. Aerofoil Selection**

The high altitude propeller design reports of Koch (1998) and Colozza (1998) contain details of how they carried out designs of their respective propellers with the assumption of a single aerofoil for the complete blade. Koch selected the Eppler 387 aerofoil section used unmodified along the propeller blade length and Colozza the SD8000 thinned or thickened as required by high Mach number drag divergence limits or structural requirements respectively.

Based on the apparent success of these designs an attempt was made to select a single aerofoil section that would be able to perform successfully at the predicted conditions experienced at all sections along the blade. References such as Abbott and van Doenhoff (1959), Riegels (1961) and Althaus & Wortmann(1981) were consulted and while there were aerofoil sections that appeared feasible, analysis showed no single aerofoil of the ones chosen was able to meet the low Reynolds and high Mach number requirements.

No single aerofoil section was found that satisfactorily met the operational requirements over the entire length of the propeller blade, not even the Eppler 387 section used by Koch (1998). This was due to the relatively low Reynolds numbers and high tip Mach numbers experienced over the outer portion of the propeller. In particular the poor high Mach number performance of aerofoil sections that were otherwise capable of producing the required local lift coefficients resulted in a series of aerofoils being sourced, each of which was tailored for their position along propeller blades. The selection of blade sections that do not perform well over their particular Mach number and Reynolds number range could result in a less than optimal performance as was shown to be the case for the Strato propellers by Schawe (2002).

Neither of the previously mentioned aerofoil sections has the capability, unmodified, to meet the high Mach number, low Reynolds number requirements of a high altitude propeller. Either an aerofoil section had to be chosen and its relative thickness varied radially along the blade or a series of propeller aerofoils had to be sourced. A search was conducted for a series of aerofoils designed specifically for use on propeller blades, that were in the public domain.

Eppler (1990) and Hepperle (2004) published information on a series of aerofoils designed for use on propellers. The Reynolds numbers experienced by the propeller blades at this scale is comparable to those of the HALE UAV propeller blades. Eppler

similarly published a family of aerofoils designed for light aircraft propellers that operated at higher Reynolds numbers than those of Hepperle (Eppler, 1990).

The Hepperle series of aerofoils (MH 112 to MH 121) were chosen on the basis that they were designed for Reynolds numbers closer to that expected by the current application (Figure 4.8). The choice of aerofoil sections was not expected to make a difference to the evaluation of the method's applicability. What is important in the evaluation of the analysis method is that the predicted aerofoil performance used in the analysis matches the actual propeller aerofoil performance. A poor choice of aerofoils could however result in the design objectives not being achieved, particularly through their low performance at high altitude.

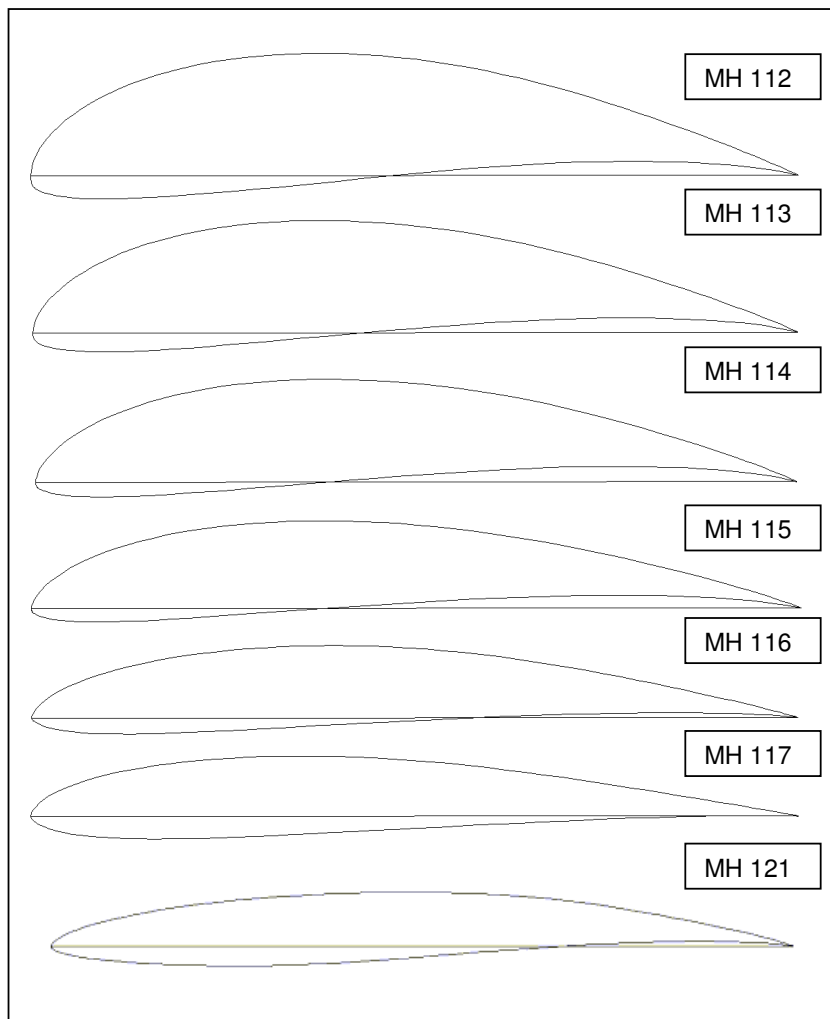


Figure 4.9 The MH family of propeller aerofoils

The particular aerofoil sections were utilised in the current propeller exactly as recommended by Hepperle (2004), starting with the MH112 aerofoil at the root and progressing through to the MH121 tip section. It should be noted that the numbering of the aerofoils is not continuous, and no published information on the MH118 or MH119 aerofoil sections was found at the time.

The suggested tip aerofoil sections MH120 and MH121 are similar in characteristics, both aerofoils are designed to be used at Reynolds numbers of 100 000 and above and at Mach numbers lower than 0.8. The MH121 was chosen based on its slightly thicker profile for easier manufacture.

The MH112 aerofoil section was chosen for use near the propeller hub ( $r/R = 0.1$  to  $0.3$ ) where its low relative thickness to chord ratio of 16.2 % was a cause for concern with regard to the structural strength of the wind tunnel test blades as percentage thicknesses of 25% and higher are typical in this region for propellers. An assessment of the blade loads was carried out and it appeared that the relatively thin aerofoil section produced a sufficient safety margin for the wind tunnel tests. This was largely due to the relatively low rotational speed required to match the full-scale advance ratios of between 0.12 and 0.39.

Having decided on the candidate aerofoils, the prediction of their aerodynamic characteristics over their expected operational Reynolds numbers was required. An aerofoil analysis code had to be sourced.

#### **4.4. Aerofoil Analysis**

Due to the high altitude operation of the propeller design the propeller aerofoils operate at a relatively low Reynolds Number and high Mach number. The aerofoil analysis must be applied over the same Reynolds Number and high Mach number range of flight conditions. This will be looked at in more detail in the following sections.

##### **4.4.1 Choice of Aerofoil Analysis Code**

As was seen in Figures 4.5 and 4.6, the local Reynolds number range experienced by the aerofoils varies from as low as 300 000 at the 30% radial position to almost 2 000 000 at the 70% position. The lower Reynolds numbers experienced by the blade sections meant

that the selection of an aerofoil analysis code was limited to codes that were capable of accurately predicting behaviour at relatively low Reynolds numbers.

Of the various aerofoil analysis codes investigated, only two codes were available to the author and were within the budgetary constraints of the project. These codes were PROFIL by Eppler (1990) and XFOIL (Drela and Youngren, 1989). While both of these codes have aerofoil design capabilities, it is only the analysis capability of the codes that was evaluated.

Eppler's PROFIL analysis code utilises a third order panel method (parabolic vorticity distribution) for the analysis of the potential flow about the aerofoil (Eppler, 1990, 1998; Eppler and Somers, 1980). An integral boundary-layer method is used for the prediction of the boundary layer development at each angle of attack. This method predicts the formation of laminar and turbulent boundary layers as well as the respective transition and separation points. It cannot however model laminar separation bubble geometries, and instead issues a separation bubble warning for each of the calculated data points. The drag increase due to the laminar separation bubble geometry is however predicted.

The results of the performance predictions in the low Reynolds number regime are usually somewhat inaccurate if a laminar separation bubble or large separated flow region occurs (Hepperle, 2004). The net result is that the code tends to under predict the aerofoil drag coefficient at lower Reynolds numbers where the separation bubble geometry is significant.

The XFOIL analysis code consists of a second order panel method (linear vorticity distribution). This is inherently not as accurate as PROFIL's third order panel method but Drela (1989) had implemented a more sophisticated boundary layer prediction method that takes the boundary layer into account while solving for the flow field. The code is thus able to model moderately sized flow separation regions the accuracy reducing when there are larger areas of separation. The transition prediction method used by Drela (1989) is based on the  $e^n$  method. And compressible flow conditions are modelled using the Karman-Tsien compressibility correction up to sonic conditions. It is not known to what extent the code has been validated in the low Reynolds number, high Mach number region as no information could be found for use in that regime.

A disadvantage of XFOIL's more complex methods, at the time it became available to the public (2001), was that the calculation time was much greater than that of Eppler's simpler analysis method. As the computational time is now of the order of minutes this was not an issue. Hepperle (2004) stated that his experiences with XFOIL "indicate that it

tends to shift the polars to higher lift coefficients and that the simple panel method (in conjunction with the spline method) has some problems with leading edges, which often results in jaggy velocity distributions even for perfectly smooth airfoils (sic).” Despite some of these concerns the XFOIL code was chosen as the analysis code for determining the propeller aerofoil characteristics due to the potentially higher predictive accuracy at the lower Reynolds numbers applicable to this work.

#### 4.4.2 Radial Distribution of Aerofoil Sections

The MH series aerofoil sections were designed for an assumed radial spacing of 0.1 r/R. In an effort to improve the accuracy of the final performance estimate the chosen aerofoil sections were distributed radially along twenty equally spaced stations along the blade in the order suggested by Hepperle (2004). The respective radial position of the aerofoils is presented in Table 4.3.

Table 4.3 Radial position of aerofoil sections

Radial Position	Aerofoil
0.05	MH112
0.10	MH112
0.15	MH112
0.20	MH112
0.25	MH112
0.30	MH112
0.35	MH113
0.40	MH113
0.45	MH114
0.50	MH114
0.55	MH115
0.60	MH115
0.65	MH116
0.70	MH116
0.75	MH117
0.80	MH117
0.85	MH121
0.90	MH121
0.95	MH121
1.00	MH121

#### 4.4.3 Prediction of Aerofoil Characteristics

The performance of each of the MH aerofoils was predicted using XFOIL (version 6.94). The number of nodes defining the aerofoil geometry used by the code is dependent on the number of coordinate points entered. This value was increased from the original 68 points for each aerofoil (61 in the case of the MH113 section) to the programs limit of 240

points using XFOIL's PPAR function (an aerofoil panelling command). At lower Reynolds numbers the spacing of the panels typically needs to be relatively close so as to capture the geometry of the boundary layer separation bubble on the upper surface. Despite the aerofoils being defined using 240 nodes and the step size between analyses being only 1 degree, the analyses at some angles of attack were not able to converge. Convergence was obtained by approaching the required angle of attack from angles where convergence had been achieved in increments of as low as 0.1 degrees to ensure successful convergence. The new point spacing is automatically arranged by XFOIL to improve resolution around areas of higher curvature. There was little evidence of the "jaggy velocity distribution" mentioned by Hepperle in the analyses carried out as part of this work.

All the aerofoil characteristics utilised by the propeller design code are referenced from the aerofoil zero-lift line. The angle of this line is however not invariant with Reynolds number for the Reynolds numbers of interest. Consequently the zero-lift line and characteristics of the aerofoil sections were predicted at Reynolds numbers of 250 000, 500 000 and 1 million.

A sensitivity analysis was then carried out on the zero-lift lines angles at the various Reynolds numbers. The results of the predictions at a Reynolds numbers of 1 million did not differ significantly from those at a Reynolds number of 500 000. The predicted zero-lift angles predicted by the analyses at a Reynolds number of 250 000 were less reliable due to the relatively larger scatter in the results. The zero-lift angles of attack of the aerofoil sections do not vary linearly between sections as illustrated in Figure 4.9 and Table 4.4.

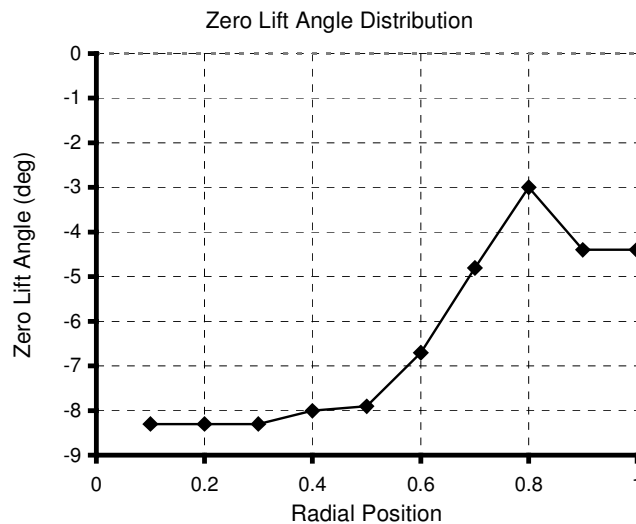


Figure 4.10 Variation in zero lift angle along the propeller radius

Table 4.4 Zero lift angles of aerofoil sections

Aerofoil Section	Zero Lift angle
MH112	-8.3°
MH113	-8°
MH 114	-7.9°
MH 115	-6.7°
MH 116	-4.8°
MH 117	-3°
MH 121	-4.4°

It was noted that the effect of the reversal in the trend of the zero lift line towards the blade tip and the change in aerofoil shape from the MH117 to the MH121 near the blade tips may cause a large radial variation in chord wise pressure gradient reducing the accuracy of the analysis.

The MH121 has a relatively far aft maximum camber position compared with that of its neighbouring section, the MH117 (See, Figure 4.10). The effect of this and the large difference in the position of the aerofoil maximum thickness point between adjacent sections may cause a local flow in the radial direction. The occurrence of any radial flow induced by a radial pressure gradient would tend to reduce the accuracy of the prediction method as it is based on the explicit assumption that the aerodynamic characteristics of each section are independent of adjacent sections.

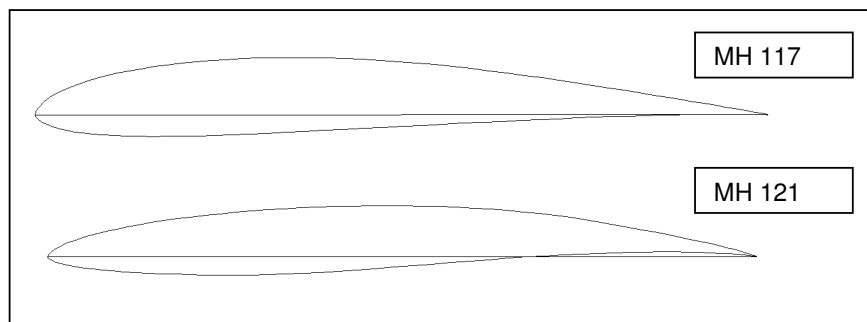


Figure 4.11 Comparison between MH117 and MH121 aerofoil section geometries

Radial flow in the boundary layer on propeller blades due to centripetal acceleration has the effect of delaying the stall to angles of attack higher than that of the 2-dimensional section data (Himmelskamp,1945 and Borst, 1973). No references could be found

referring to the effect of relative changes in chord-wise pressure distribution across a small radial distance.

All the propeller aerofoils were rotated with respect to their zero lift lines and XFOIL was then used to predict the zero lift line based lift and drag polars for Reynolds numbers of 1 million, 500 000, 250 000 and 100 000. The data was typically obtained over a range of angles of attack from 0 degrees to 30 degrees. This data was utilised to populate the aerofoil characteristic database in the mission simulation code.

At the Reynolds numbers of 250 000 and 100 000 there was occasionally a variation in zero lift angle of up to 3 degrees from that of the higher Reynolds number curves. This effect was generally not an overall shift in the lift curve but a deviation at low angles of attack from the otherwise linear lift curve of higher angles of attack. The cause of this shift was invariably by a predicted boundary layer separation on the lower surface of the aerofoils at these lower Reynolds numbers. Extrapolation of the linear portion of the predicted lift curve would usually result in an interception with the vertical (lift coefficient) axis at angles of attack very close to zero. This predicted zero lift angle was used in the calculations. The aerofoil data as predicted by the XFOIL analyses and used in the analysis is included as Appendix A.

It is worth noting that the effect of these lift curve slope deviations is potentially significant in the analysis of the propeller at large negative pitch angles as the lift coefficients of the aerofoil sections at those radial points operating at very low lift coefficients whose value could be greater or less than that of the neighbouring section by values as large as 0.3. Fortunately for the current analysis the portions of the blade that experienced these low lift coefficients were further outboard and seldom experienced Reynolds numbers below 250 000 as shown in Figure 4.5, except at locations very close to the tip where three dimensional flow effects dominate.

The propeller design code uses average aerofoil drag to lift (D/L) values, the inverse of the common aerofoil efficiency parameter L/D, in the determination of the propeller blade geometry. The expected drag/lift ratio of each aerofoil section is required for the initial design phase and was calculated using XFOIL at two degree increments in angle of attack from 0 to 30 degrees at Reynolds numbers of one million and 500 000. The results of these calculations are illustrated in Table 4.5. The average of the maximum D/L ratios from the ten radial stations was determined to be 0.00702 for a Reynolds number of one million and 0.00836 for a Reynolds number of 500 000.

Table 4.5 Maximum D/L ratios for the chosen propeller aerofoils

Aerofoil	r/R	Reynolds number	
		1M	500k
MH112	0.1	0.00691	0.00841
MH112	0.2	0.00691	0.00841
MH112	0.3	0.00691	0.00841
MH113	0.4	0.00650	0.00797
MH 114	0.5	0.00622	0.00752
MH 115	0.6	0.00680	0.00763
MH 116	0.7	0.00654	0.00792
MH 117	0.8	0.00826	0.00991
MH 121	0.9	0.00757	0.00872
MH 121	1.0	0.00757	0.00872
	Average D/L ratio	0.00702	0.00836

The chosen radial distribution of design lift coefficient was chosen to be a linear reduction from 1.3 at the root of the blade to 0.7 at the tip as these lift coefficient values coincide closely with the lift coefficients at which the lift/drag ratio is maximum for the MH112 and MH121 sections of the root and tip respectively based on the XFOIL predictions.

Four of the design inputs required to define the minimum loss propeller have now been fixed. These are diameter (limited by aircraft geometry), gear ratio in relation to engine characteristics (limited by tip Mach number), number of blades (limited by aircraft geometry) and section design lift coefficients range (dictated by the aerofoil section properties) as illustrated in Table 4.6.

Table 4.6 Fixed design parameters

Propeller diameter (m)	2.8
Gear Ratio	3.3
Number of blades	2
Design Cl Gradient – Root to Tip	1.3 - 0.7

The remaining three primary inputs required by the design method are propeller design power, operational altitude and velocity all of which will be input variables in the design phase of the UAV propeller blade to determine the propeller that will provide the longest cruise range for the HALE UAV.

## **5. MISSION PROPELLER DESIGN AND ANALYSIS**

The previous chapter detailed the initial propeller design to determine values of the parameters affecting the propeller aerofoil selection, the initial sizing and the Reynolds numbers and Mach numbers along the blade.

A mission simulation program was written consisting of a time stepped mission flight path simulation including an implementation of Larrabee's design and analysis routines, detailed atmospheric modelling, UAV and engine performance modelling and the predicted aerofoil characteristics of all the propeller aerofoils at various Reynolds numbers in the analysis routines. Various propellers produced in the initial design phase were evaluated over the prescribed mission in the analysis routines. The measure of performance utilised to determine the optimal design was chosen to be that of total cruise distance achieved as predicted by the mission simulation program.

### **5.1. Propeller Design in the Mission Simulation Program**

The modelling of the atmospheric conditions in the mission simulation code was done through the incorporation of software code including the standard atmosphere equations of the COESA (Carmichael, 2006). The simulation code determines the air density, viscosity and speed of sound at each altitude point in the mission. The output of the simulation was validated against the COESA atmospheric tables.

The average of the two D/L values from the XFOIL analyses, a value of 0.00769, (Table 4.4) was selected as the overall aerofoil efficiency estimate. This value proved to be somewhat optimistic due to the later propeller designs having lower Reynolds numbers than those initially predicted along the optimal blade at cruise altitude. Sensitivity analyses however showed that the variation of D/L ratio from 0.00702 at a Reynolds number of 1 million to 0.00836 at a Reynolds number of 500 000 varied the resultant chord length by only 0.3 %, that is a maximum of 1.5 mm on the blade chord of 484 mm on the full-scale propeller. The aerodynamic effect of such a small chord change on the final propeller performance would be insignificant in this evaluation and well within the error bounds of the code.

The performance analyses utilised the predicted aerofoil characteristics at the actual Reynolds numbers occurring along the blade at each point of the mission. Having previously fixed the propeller diameter, reduction gear ratio, number of blades and the radial variation of design lift coefficient, a range of values for the remaining parameters, design power, design altitude and design velocity were set in the design routines of the mission simulation program. The resulting UAV performance was assessed for total distance flown. Additional parameters such as initial and final climb rate and propeller efficiency were also monitored.

The range of design engine powers that was investigated was varied from 10 to 50 kW, design altitude was varied from sea level to 15 000 m and design velocity from 20 to 60 m/s. Each of these inputs produced a propeller design optimised for that design point. The performance of that propeller was then analysed over the mission and its performance assessed.

## **5.2. Propeller Performance Analysis in the Mission Simulation Program**

The propeller performance analysis capability of the mission simulation assessed the performance of the propeller over the climb and cruise phases of the mission. These two phases of the mission are analysed separately.

### **5.2.1 Climb Performance Analysis**

The mission simulation program simulates the UAV performance over the defined mission in a time-stepped approach. During the climb phase, the UAV is flown at its best rate-of-climb airspeed to maximise climb rate. This airspeed is determined by the UAV's aerodynamic characteristics and its mass at any given time during the mission. The initial simulation time steps were set to intervals of five minutes. The engine is assumed to operate at full power to maximise climb rate and the propeller pitch angle is adjusted at each time step to absorb the power at the respective rotational speed. The fuel consumption is calculated at each time step throughout the mission and the UAV mass incrementally reduced. The required thrust is also calculated at each time step in the mission and the excess thrust-power product determined and converted into a climb rate through division by the mass of the UAV at that time. The fuel used over that time step is calculated from the engine's fuel consumption curves and the UAV mass updated.

As the UAV approached the 15 000 m altitude the time increments were reduced to sixty seconds to accurately determine the time at which the altitude was reached. In order to ascertain the effect of time increment on the simulation result, the five-minute increments were reduced to one-minute increments in the mission simulation resulting in a negligible effect on the overall range prediction for which the optimal propeller was to be chosen.

### 5.2.2 Cruise Performance Analysis

Once at 15 000 m altitude, the engine power is reduced to that required to maintain altitude at the UAV's minimum drag speed. The pitch of the propeller is adjusted iteratively until its output (thrust) power matches the required power. The fuel consumed over that time step is calculated from the engine's fuel consumption curves at partial throttle and the UAV mass updated.

Larger time steps (typically 30 minutes) were used over this phase of the mission simulation as the propeller was operating closer to its design point and operating at a relatively high efficiency with minimal fuel usage. Decreases were again made in time steps to sixty second increments over the latter portion of the mission to improve the accuracy of the simulation termination.

### 5.3. Results of Analyses

Altering the design power input in increments of 10 kW, the design altitude input in increments of 1000 m and the design velocity in increments of 10 m/s would have required a total of 400 simulations to be evaluated each taking typically 5-6 minutes to run. To reduce the number of runs required, simulation results for each design velocity and design power at a fixed design altitude were obtained each requiring 25 simulations to complete. These rapidly illustrated that there were a large range of propeller designs that could not achieve some or all of the mission criteria. It also illustrated that propellers designed for altitudes of 12 000 m or higher were the most likely to succeed. What also became apparent during this exercise was that the predicted propeller performance change with linearly incremented input variables was not necessarily monotonically increasing or decreasing in a fashion that would allow the use of a gradient based optimisation technique to converge to a solution. This was partly due to the finite time step size but also due to the non-linear behaviour of the various propeller aerofoils when operated outside their design range of angle of attack.

The results also showed a relatively small range of performance differences between the better propeller designs. As the intention of this work was to find if Larrabee's method could produce a feasible propeller, producing the optimum propeller in itself was not a requirement.

It was determined that the most efficient performances appeared, not too surprisingly, for those propellers designed for altitudes close to 15 000 m. Through altering the design power input and design velocity input within a reasonably narrow range in increments of 1 kW and 1 m/s respectively, the final propeller design was chosen as the one with the longest range capability.

#### 5.4. Choice of Propeller Design

The final choice was for a propeller designed for an airspeed of 50 m/s, 34 kW input power and to operate at 15 000 m. This propeller produced an initial 5.22 m/s climb rate, a final climb rate of 1.17 m/s at 15 000 m, attained an efficiency of 0.883 in cruise and would provide a total range of a little over 650 km. Its design point advance ratio was determined to be 0.28. The design parameters on which the final propeller was based are given in Table 5.1.

Table 5.1 Final design parameters

Blade Radius (m)	1.4
Design Speed (m/s)	50
Design Power (kW)	34
Gear Ratio (for tip Mach < 0.8)	3.3
Number of blades	2
Design lift coefficient at Root	1.3
Design lift coefficient at tip	0.7
Design Altitude (m)	15 000

Assuming no sweep at the quarter chord position, the resultant relative chord distribution ratio is given in Figure 5.1, with twist distribution illustrated in Figure 5.2

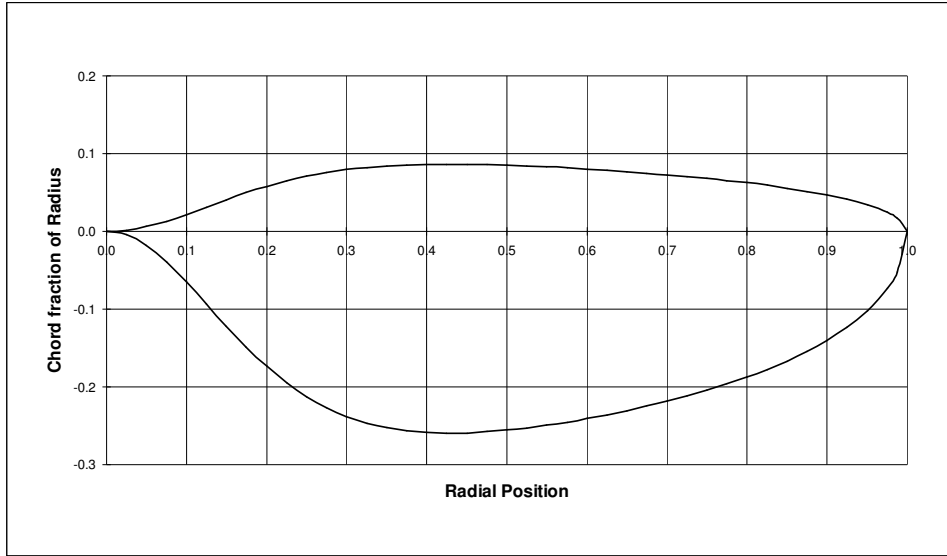


Figure 5.1 Radial chord distribution

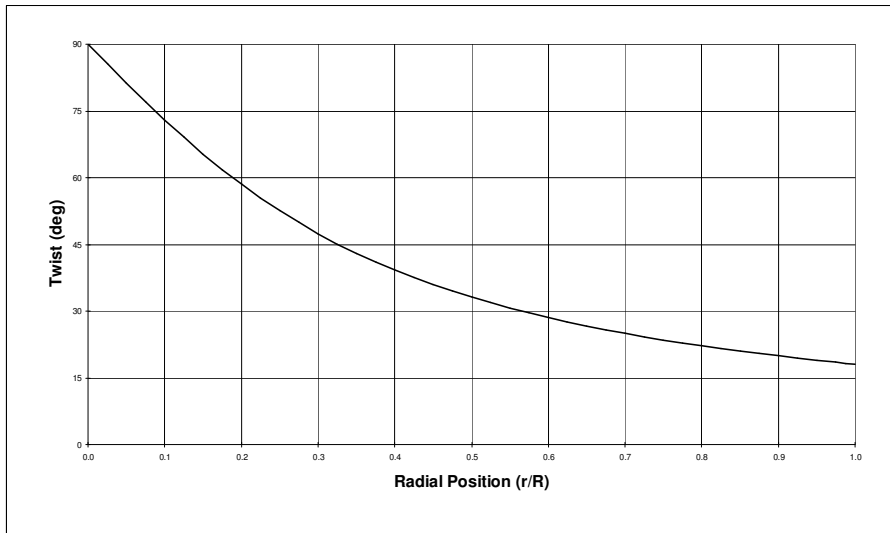


Figure 5.2 Radial twist distribution

Due largely to the low air density at the design point the final blade geometry has the typically wide chord geometry (in comparison with other aircraft propellers) found on high altitude aircraft.

## 5.5. Predicted mission performance

The aerodynamic behaviour of the selected propeller was analysed over the complete mission. The radial variation in lift coefficient over the blade during the climb phase of the mission is presented in Figure 5.3.

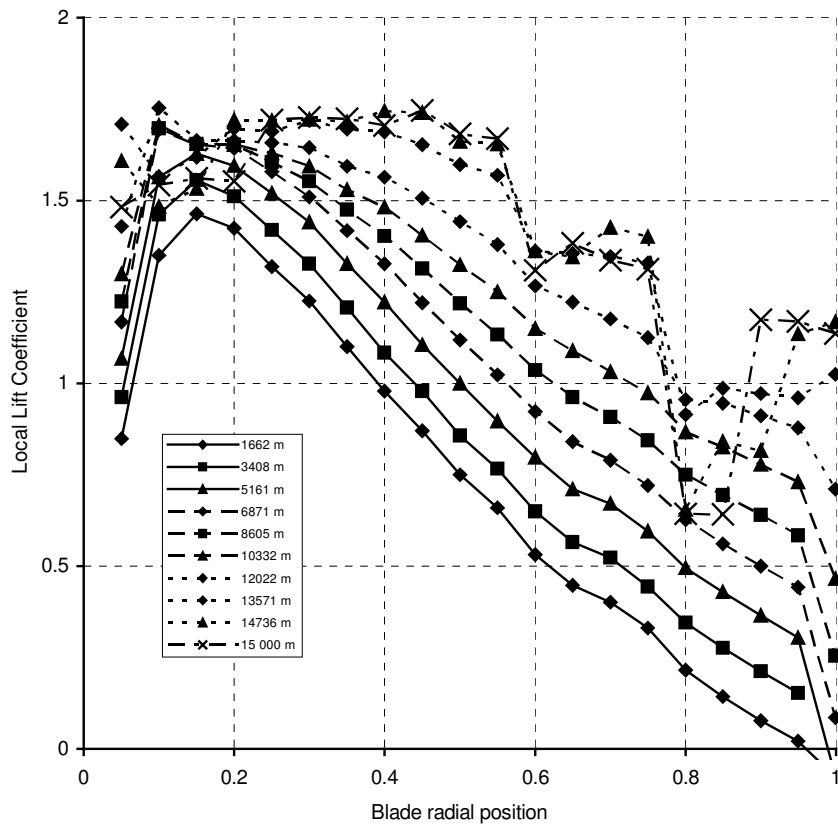


Figure 5.3 Propeller radial lift coefficient distribution during climb phase

It can be seen that at the lower altitudes the propeller tips are acting with a small negative thrust and the root aerofoils are operating close to their stall angles due to the large negative pitch angle and relatively large blade twist optimised for higher airspeeds.

At an altitude of 10 332 metres the aerofoil section at the 0.8 radial point is about to stall and at an altitude of 12 022 metres the aerofoil sections at the 0.6 radial position and

outboard have also stalled while in the climb phase. This is due to the increasingly larger pitch angles being commanded to absorb the full engine power in the thinner air. The large variations in radial loading would reduce the accuracy with which the analysis code (which assumes a certain radial loading) is able to predict the induced velocities.

Reducing power at this point would reduce the loading on the blade and hence the stalled areas. The resultant in climb rate may still have been sufficient to meet the performance requirements but the complexity of adjusting power during the climb phase was not added to the simulation.

Analysing the blade pitch angle shows a variation from a large negative value of -17.9 degrees at the start of the mission (after the pre-acceleration to 27 m/s) to a 8.7 degrees positive angle as the propeller attempts to absorb the available engine power while at a true airspeed close to three times that of the equivalent airspeed at altitude. See Figure 5.4.

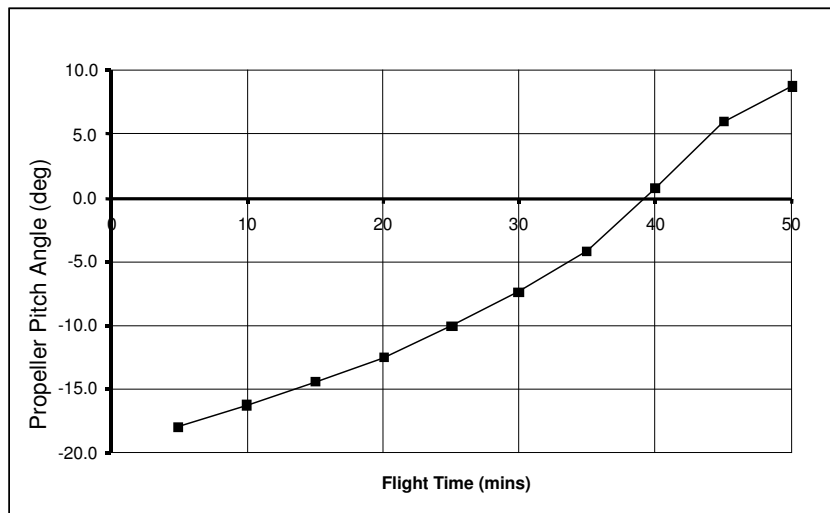


Figure 5.4 Propeller pitch angle variation over flight time

The propeller tip Mach number increased from 0.63 to 0.81 during the climb phase illustrating that the 3.3:1 gear ratio could be increased further to keep the tip to below Mach 0.8. This was not done as exceeding the Mach limit by 0.01 was felt to not be significant for the purposes of this study.

Once the cruise altitude has been reached the engine power and the pitch angle of the propeller are reduced to a point where the radial distribution of lift coefficient is closer to

that of the design point and its overall efficiency increases dramatically. This radial distribution of lift coefficient is however not the same as that of the original design. The propeller is operating at a speed of approximately 59 m/s, different from that of its design point 50 m/s and absorbing approximately 17 kW as opposed to the 34 kW for which it was designed.

The radial blade loading distribution is largely constant over the duration of the cruise phase due to small variations in required power and airspeed as the mass decreases as illustrated in Figure 5.5.

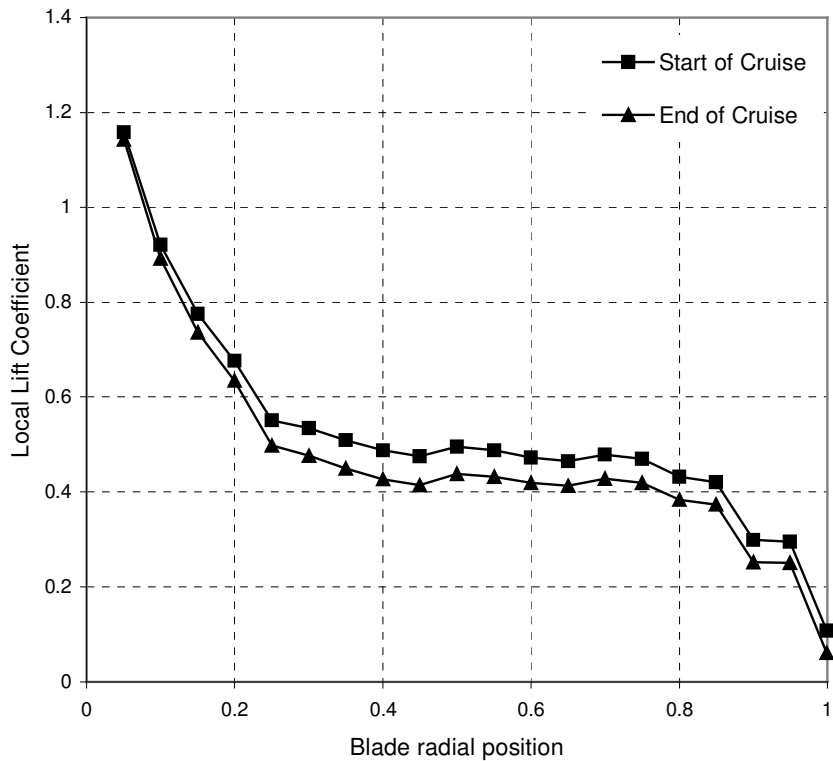


Figure 5.5 Propeller radial lift coefficient distribution during cruise

The analysis showed that the predicted advance ratio varied from 0.116 to 0.23 in the climb phase and maintained a value of a little less than 0.40 over the cruise phase, Figure 5.6.

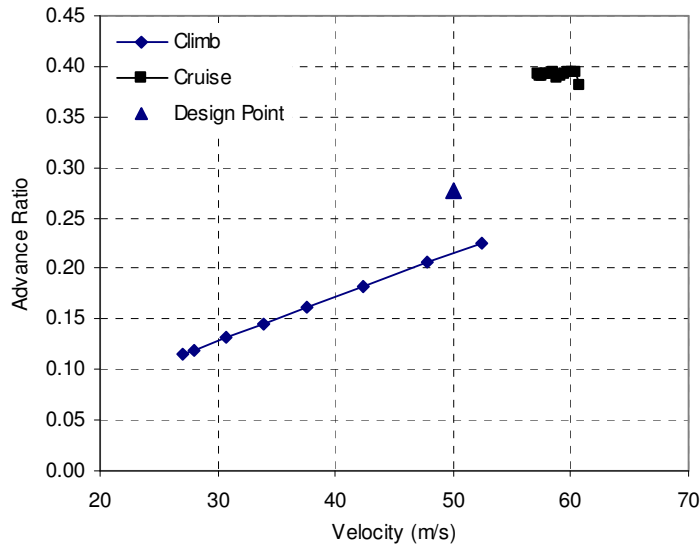


Figure 5.6 Variation in advance ratio over the mission

## 5.6. Comment on Design Capability

It appears that despite the propeller operating at blade angles far from its design point for portions of the mission, Larrabee's method can be successfully used to design propellers that are capable of sufficiently high performance for these missions. i.e. a minimum induced loss propeller can be designed that works over the wide operating speed range and appears to be efficient during the cruise flight. What is still required is to validate the accuracy with which Larrabee's analysis methods predicts the behaviour of the designed propeller at operating points far removed from the initial design point for which it was intended. This validation was done using a scale model of the propeller in the CSIR 2 Metre Wind Tunnel (2MWT).

It is possibly worth noting here some details that may have an effect on the outcomes of the simulation work. The initial estimates of propeller pitch angle used to assist convergence of the iterations in the performance prediction code were kept unchanged for calculations in both flight phases (climb and loiter). The final pitch angle required to match the particular flight phase was thus approached from the same direction at every time step. This may have resulted in an offset to the results for a number of reasons:

- The performance improvements brought about by changing the input parameters were often dependent on the largely non-linear post stall behaviour of the various aerofoil sections during the climb phase of the mission.

- The time steps in the simulation caused incremental steps in the output data. The time predicted to attain an altitude might occur either just before or just after a time increment. The time increments were decreased to reduce the magnitude of the problem but the difference in predicted performance between designs was relatively small due to the relatively large effect of the cruise phase.
- The termination criteria in the code were set within reasonable tolerances in order to reduce run times and ensure convergence, i.e. predicted propeller thrust typically of within 10 N (approximately 3.6 % of cruise drag) of the aircraft drag figure. These finite tolerance values result in outputs that were fixed increments different from the next nearest solution.

Subsequent investigation (Himmelskamp,1945) showed that the local aerofoil sections exhibit a significantly different behaviour from that expected of a rotating aerofoil. Some of the important differences identified were:

- The local lift coefficient increases at the blade hub
- The lift-curve slope of the rotating aerofoil is lower than that of the two-dimensional aerofoil yet stalls at a higher angle of attack and hence larger lift coefficient than the two-dimensional aerofoil.
- The centrifugal effects are important for low aspect-ratio propellers and negligible for slender propellers, helicopter rotors and wind turbines.
- More important are the Coriolis effects and the apparent pressure gradients due to potential cross-flow.
- The flow is essentially chord wise in regions of attached boundary layers, and strongly radial beyond the separation line.

## **5.7. Prediction of Wind Tunnel Propeller Performance**

Both the parametric propeller design and analysis spreadsheet and the UAV mission performance programs were modified to predict the performance of the reduced scale wind tunnel test propeller at various advance ratios. The spreadsheet version of the analysis code was utilised to provide an understanding of the analysis convergence behaviour and to assist in the prediction of the blade loads. The UAV performance estimation procedures were removed from the mission programme and replaced with a simple procedure to set the propeller rotational speed and pitch angle to fixed values. The tunnel airspeed was then incremented to model the expected advance ratio range from

0.116 to 0.40 through varying the tunnel speed to match the propeller rotational speeds of typically 800 or 1200 rpm.

The Reynolds numbers of the performance predictions matched those of the propeller exactly due to the modelling of the actual wind tunnel model as opposed to the original design. The range of Reynolds numbers being modelled is similar but not identical to those that would have been experienced by the HALE UAV propeller. At the 70% radial station the HALE UAV propeller would have been operating at a Reynolds number of approximately 480 000 while the wind tunnel propeller would be operating at a Reynolds number of 440 000 at 20 m/s tunnel speed (advance ratio of 0.4).

The predicted performance of the wind tunnel test propeller from the mission analysis code is illustrated in Figure 5.7 for pitch angles from -12 degrees to 12 degrees at both 800 and 1200 rpm in the format of thrust coefficient versus advance ratio. A portion of the 800 rpm and 1200 rpm lines overlap showing that Reynolds number has a very small effect on the thrust coefficient. This is due to there being a very small change in lift curve slope or zero lift angle due to Reynolds number.

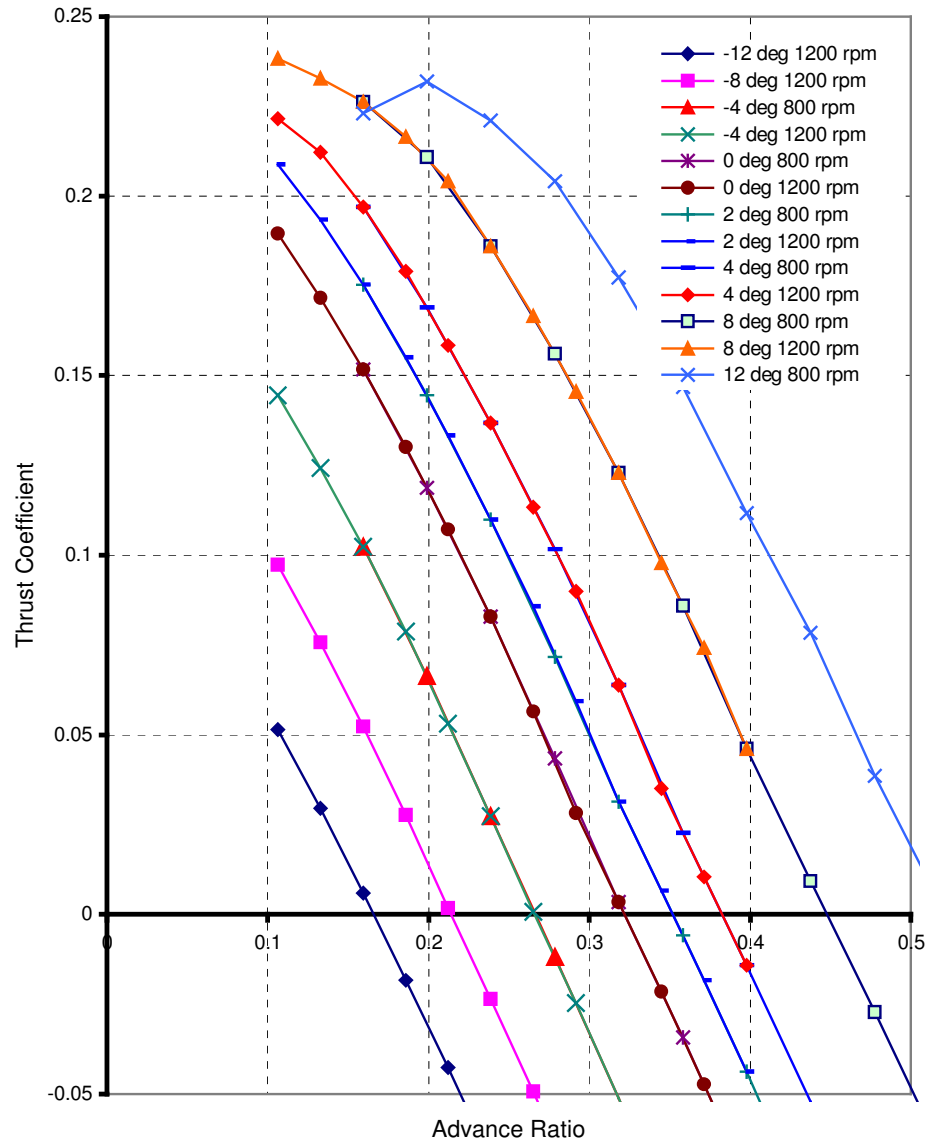


Figure 5.7 Predicted thrust coefficient vs. advance ratio for pitch angles from -12 to 12 degrees

## **6. DESIGN AND MANUFACTURE OF THE TEST EQUIPMENT**

The reduced scale model of the designed propeller was manufactured for testing in the CSIR 2 metre open return wind tunnel (2MWT). A propeller test rig was designed in support of this project but due to limited funding being available the motor sizing and torque measurement capabilities was sized for the planned testing of propellers of greater size. The thrust measurement capabilities were made to be variable through the use of standard load cells of different ratings. Details of the scale test propeller, propeller test rig and wind tunnel are described below.

### **6.1. Sizing of propeller**

The information sourced on the applicable correction factors required when wind tunnel testing propellers revealed that, in general, testing in wind tunnels with open test sections requires relatively small interference or boundary corrections if applied at all (Rae & Pope, 1984).

The CSIR 2MWT is of the open test section type. The boundary layer thickness at the exit of the contraction has been conservatively estimated by test personnel to be less than 100 mm thick. Based on an assumed 2 m inlet diameter, a propeller diameter of 1.7 metres was initially considered. Choosing the largest possible diameter for the test propeller would better match the test rig torque and thrust measurement capabilities and hence improve the accuracy of the tests.

Initial calculations however demonstrated that the existing ground adjustable propeller hub would not have withstood the centrifugal loads of a 1.7 m diameter wooden propeller turning at the rotational speeds required to model the advance ratios. A lightweight construction method such as that utilising carbon fibre composites may have solved this problem but the cost constraints on the project precluded the options of manufacturing either a stronger hub or a lightweight propeller. It was determined that a propeller of 1.2 m diameter or smaller, if manufactured of wood, would impose acceptably low centrifugal loads on the hub.

### 6.1.1 Choice of Materials

Having chosen the diameter of the propeller the next consideration was the method of construction with two options being considered and costed; a CNC cut wooden propeller or a hand crafted wooden propeller manufactured by one of the local manufacturers. The CNC machined blades were chosen due to their higher accuracy yet similar cost to the project.

European Beech was chosen as the construction material as it is frequently used in the manufacture of wooden propellers (Clutton, 1993). This wood is classified as a medium density (relative density of 0.6 to 0.8 kilograms per cubic metre), hard and strong wood with a high shock resistance (Bektas, 2002).

### 6.1.2 Test Propeller Geometric Definition

The coordinate data of the selected aerofoils was captured in Rhinoceros<sup>®</sup> (Version 3.0), a NURBS (Non-uniform Rational B-Spline) surface modelling CAD package. The aerofoil sections were first positioned at their respective radial stations. The origin for all the sections was originally defined at their respective leading edges. The sections were moved forward in a chord wise direction until their quarter chord points coincided with a radial line emanating from the centre of the hub. This ensured that there was no quarter chord sweep in the blade as this could have potentially induced a radial flow component other than that induced naturally by the rotation of the propeller blades.

The sections were then individually rotated about their quarter chord points to the design local pitch angle with respect to their local zero lift angles to coincide with what was modelled as illustrated in Figure 6.1.

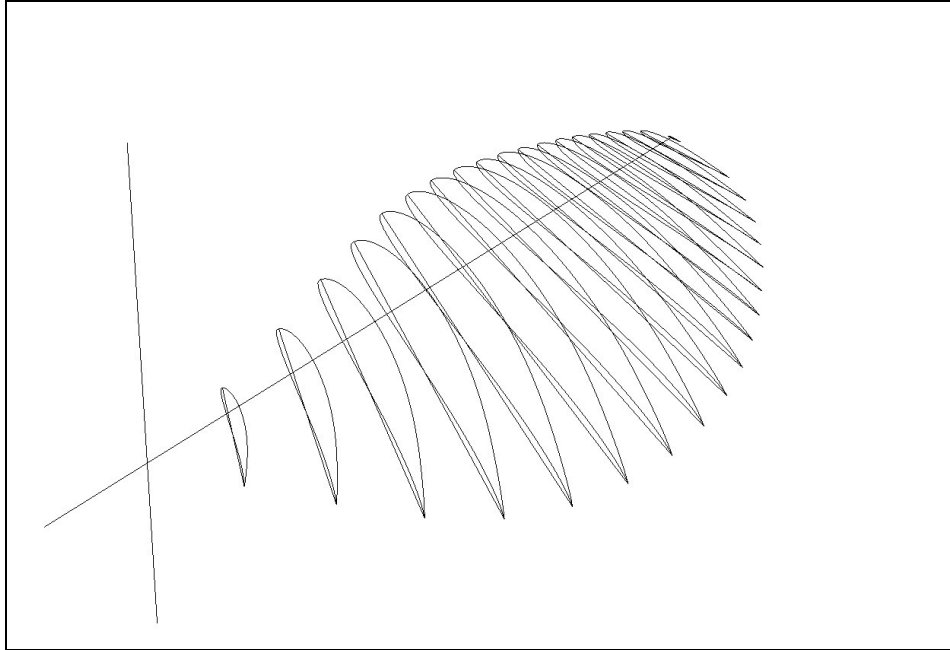


Figure 6.1 Rotation of the aerofoil sections around their quarter chord location

The trailing edges of the series of MH aerofoils are designed to have zero thickness, to enable practical manufacture of the propeller the aerofoil trailing edges were truncated at the point where the thickness was 0.1 mm. This trailing edge thickness was increased on the actual blades with the addition of a thin (0.08mm) protective fibreglass cloth covering to approximately 0.3 mm. The aerodynamic effects of the increased trailing edge thickness were determined. The MH 116 section, which is used at the 70% radial position, was analysed in XFOIL and the result was a predicted increase in drag of the order of 0.3 % and a negligible increase in maximum lift coefficient. These errors were accepted as being well within the accuracy of the prediction methods and insignificant enough for the current research.

The top and bottom surfaces were then lofted in Rhinoceros<sup>®</sup> a NURBS based surfacing CAD package and a thin strip surface was added to join the top and bottom surfaces at the trailing edge to form the solid geometry required for cutter path generation.

The root attachment of the blade was designed to fit an existing ground adjustable aluminium hub. This attachment was then faired into the new blade surface over a distance of 150 mm from the centre of rotation. In so doing the aerofoil shapes up to 76 mm along the blade were altered in a way that would considerably affect their aerodynamic characteristics. (See Figure 6.2). However as these effects are relatively close to the centre of rotation of the propeller the overall effect of the change in lift and

drag on the performance of the propeller was expected to be small and no corrections were made to the predictions.

The root attachment was positioned with respect to the blade to ensure that the blade centre of mass was aligned with the rotational axis of the hub to reduce inducing bending moments from the centrifugal loads into the hub.

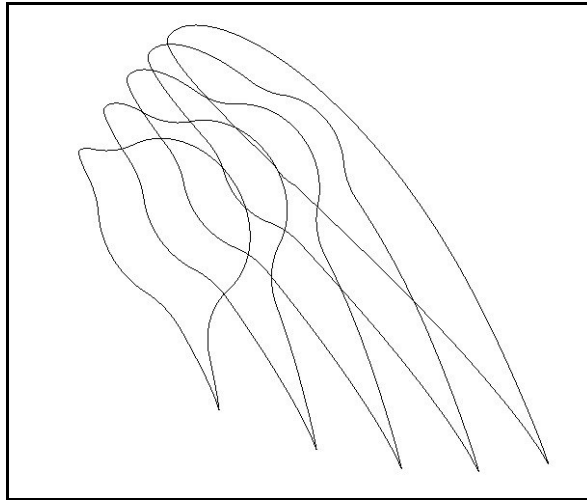


Figure 6.2 Cross sections through the blade root area showing effect of hub geometry

The cross sectional areas of the blade were calculated at a 5% radial spacing to ensure that no point was less than that of the 20 mm diameter hub. The final blade geometry is illustrated in Figures 6.3 and 6.4.

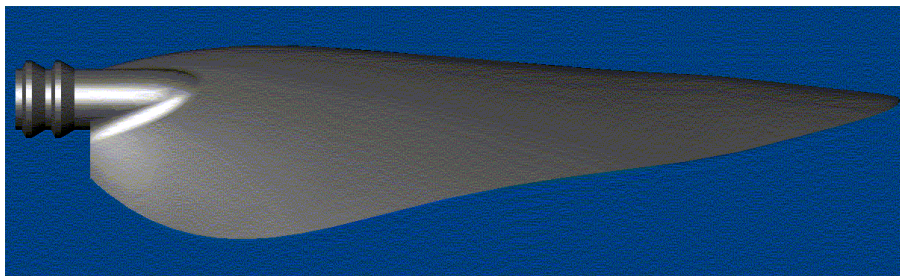


Figure 6.3 Rear view of final blade geometry

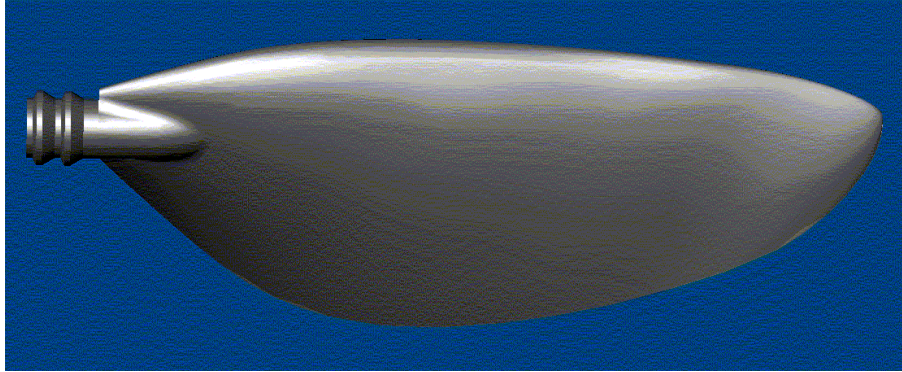


Figure 6.4 Top view of final blade geometry

In order to minimise the amount of material that would require machining, the blade geometry was rotated in the CAD package through a 30 degree angle about its pitch axis to fit within the shape of the wood blank from which the blades were to be cut (Figure 6.5)

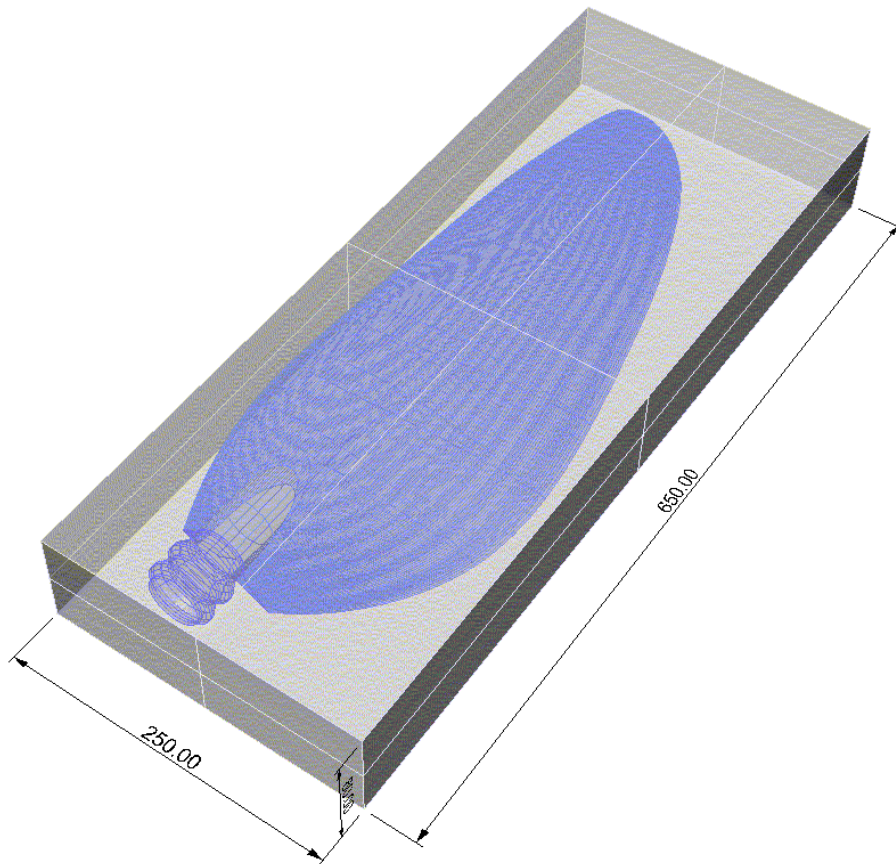


Figure 6.5 Final blade geometry shown with respect to the wood blank

The final propeller geometry was saved in STEP format for generation of the cutter paths by the machine shop.

### 6.1.3 Calculation of the Blade and Hub Stressing

The loads and stresses in the propeller blades were determined from first principles. The blade was discretised into small radial segments, the spacing being varied from 10 mm near the root where the local stresses would be the greatest to increments of 0.05  $r/R$  or 30 mm from 0.3  $r/R$  where the stresses were expected to be lower.

The cross sectional area was determined through sectioning the CAD geometry. The distance from the centre of the hub to the mid point of each element and the volume of the segment outboard of each particular radial position were determined along with the mass of each segment. A conservative figure of 0.8 kg per cubic metre assumed wood density was chosen, the highest stated wood density for Beech according to Bektas (2002).

### 6.1.4 Blade Root Stresses

A maximum blade rotational speed of 1200 rpm was chosen to limit the hub loads yet be sufficiently high to model the required advance ratios within the wind tunnel. The rotational stresses were determined using the blade mass distribution. No additional stresses due to inertial torque, pitching moment or bending caused by the lift generated by the blade were calculated at this point.

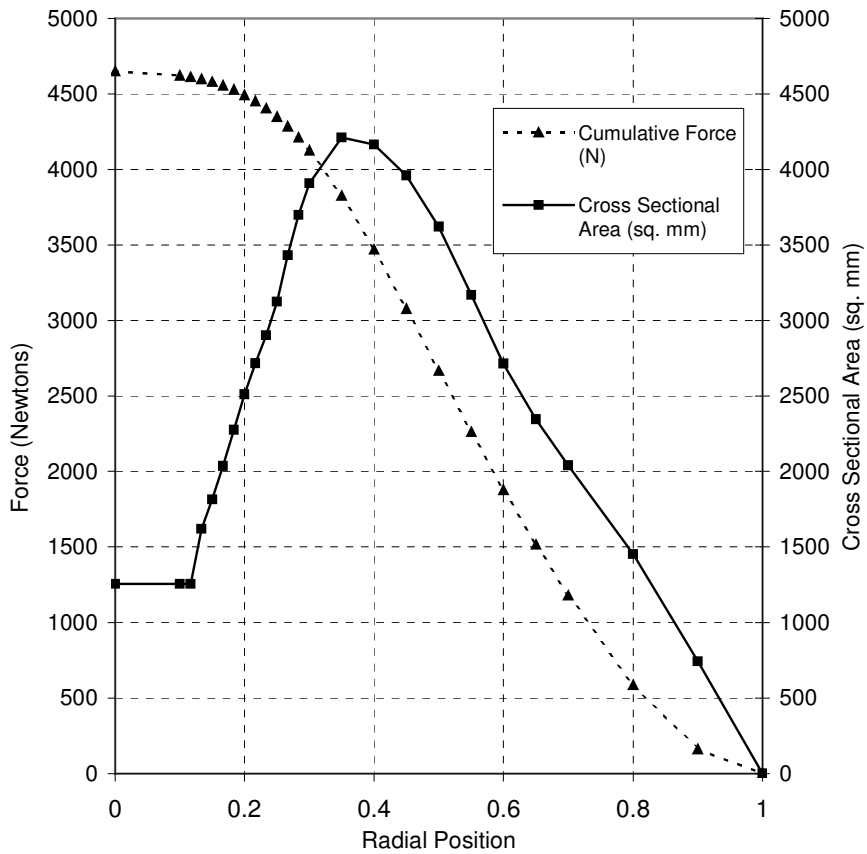


Figure 6.6 Radial distribution of cross sectional area and blade stresses at 1200 rpm

The failure strength of Beech wood was determined to have a large statistical variation of between 564 and 2871 MPa in tension and between 5.5 MPa and 15.3 MPa in shear along its grain (Bektas, 2002). The design of the blade root attachment was required to match those of the existing hub resulting in the shear area under the two annular restraining rings being small compared with the cross section of the blade root. Calculations showed that the most likely failure mode appeared to be that of shear failure of the rings from the blade root due to the shear strength of the wood being two orders of magnitude smaller than the tensile strength.

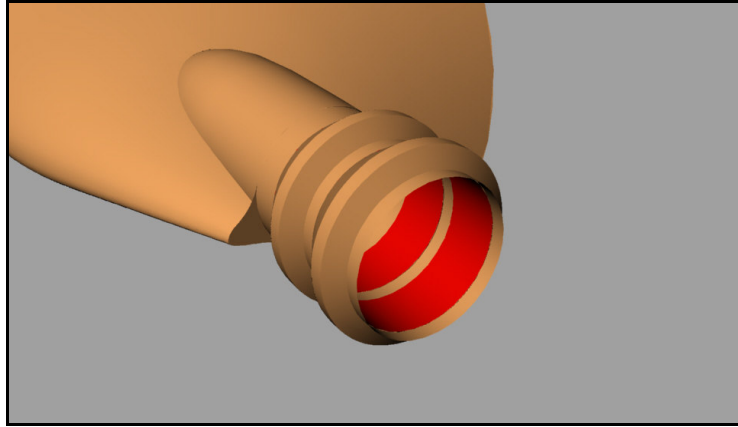


Figure 6.7 Hub shear area shown in red

Due to the large variation in the wood strengths occurring due to moisture content and the natural variability of the wood itself, a test sample was constructed from one of the wood laminates (see Figure 6.8) used to manufacture the propeller and loaded in double shear in a Schenk tensile test rig to confirm the published strength values.



Figure 6.8 The Beech wood shear test sample

The initial shear failure occurred along one shear surface under a load of 2.32 kN and then upon continuation of the testing, on the remaining surface at 1.16 kN. Both failure cases demonstrated an ultimate shear strength of the wood of 18.98 MPa. This value exceeded the upper limit of the expected range provided by Bektas(2002) by 24%. The measured value was used in the stress calculations to determine the reserve factors. The results of the stress calculations are displayed in Appendix G.

Calculations showed that at the maximum planned rotational speed of 1200 rpm the maximum tensile stresses induced into the blade would be 3.70 MPa at the hub edge. The shear stress was calculated to be 1.23 MPa.

The reserve factors for the blade were 152 in tensile stress and 10.45 in shear. Due to the relatively large values no stress concentration factors were taken into account nor were the additional stresses due to blade torque and lift as they are typically relatively small (Amatt, 1973).

### 6.1.5 Ground Adjustable Hub stresses

Figure 6.9 illustrates the aluminium ground-adjustable hub that was used for the wind tunnel tests.

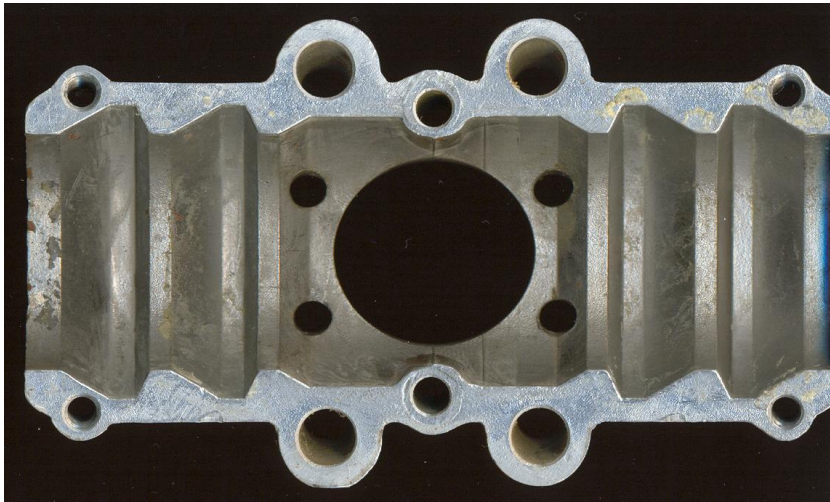


Figure 6.9 View of ground adjustable hub section showing root fittings

This hub fits onto two integral, annular rings around the blade root to retain the blades. The dimensions of the hub were measured and the matching propeller blade root designed to be 0.5 mm smaller in radius. Additional layers of glass composite reinforcement on the blade root made up the difference in size.

The type of aluminium alloy used in the hub was not known. For safety reasons an ultimate tensile strength (UTS) of 70 MPa was assumed, slightly lower than the UTS of A02080 aluminium alloy in the 'F' state, one of the weakest cast aluminium alloys (Kaufman, 2004).

The results of the stress calculations showed that the test propeller could be safely rotated at rotational rates of up to 1200 rpm. At this speed the reserve factors for the hub

were determined to be 8.42 in tension. The blade reserve factors were 3.52 due to tension and 5.83 due to shear.

The structural loads induced at rotational speed of 1200 rpm were thus determined to be within limits for the weakest specification of cast aluminium.

### 6.1.6 Manufacture of the Test Propeller

Planks of carefully selected European Beech wood were planed to a thickness of 20 mm each and laminated with Epolam 2022 epoxy resin and then further trimmed and planed to form two blocks of 650 mm x 260 mm x 85 mm high. The two test propeller blades were machined from these blanks on a 3-axis CNC machine using a wood router tool rotating at high speed.

The trailing edge geometry was thickened by 1 mm over the rear 10 mm of the chord so as to preserve the trailing edge while cutting. This thickened trailing edge was later removed by hand sanding down to the required 0.1 mm thickness.

While being machined the blade was supported at various locations along its leading and trailing edges by small portions of the wood to inhibit movement of the block away from the cutter due to the cutting forces. These too were removed once the CNC machining was completed.

The machined surfaces were hand finished to a smooth finish and the blades covered with a 49 g/m<sup>2</sup> fibreglass cloth and Epolam 2022 epoxy resin for protection from moisture and handling damage.

The blades were finally hand finished to a smooth surface finish. A thin coat of clear sanding sealer was applied to the blades to fill the slight weave pattern of the fibreglass cloth.

The blade roots were glassed with two layers of 110 g/m<sup>2</sup> glass cloth and Epolam 2022 epoxy resin for additional structural support and to close the 0.5 mm gap in the geometry between the hub and the blade. The aluminium hubs were coated in a release wax and loosely clamped over the glassed blade roots. Thus a tight fit on the blade roots was assured when the hubs were bolted together for wind tunnel testing.

The propeller hub and blades were mounted on a freely rotating shaft and the blades were balanced statically about their rotational axis. The lighter of the two blades was sprayed with additional thin coats of clear sanding sealer that was allowed to dry before the assembly was checked again. This process was repeated until the blades balanced. Both blades were then given a similar amount of sanding to improve the surface finish and finally balanced.

The blades, labelled A and B for individual identification during testing, were weighed on a digital scale with a 5 g resolution, their respective masses determined to be 1.000 kg and 1.005 kg respectively. This compared sufficiently well with the predicted mass of 1076g based on an assumed wood relative density of 0.8 kilograms per cubic metre. It was thus unlikely that the predicted stresses due to the rotating of the mass of the propeller would be exceeded during the wind tunnel tests.

## **6.2. Conceptual Design of the Propeller Test Rig**

A propeller test rig was designed to use existing load cells for thrust measurement and a commercial torque cell and transducer system for torque and rotational speed measurement.

No temperature compensation over and above that provided by the balanced strain gauge bridge was incorporated in either the load cell or the torque transducer system.

The functional concept of the propeller test rig for thrust measurement is that of a teetering frame hanging from a transverse set of flexures positioned close to the longitudinal centre of gravity of the motor and frame combination and mounted close to the floor. The thrust (or drag) forces of the propeller cause a vertical load in the load cell mounted at the rear of the rig as illustrated in Figure 6.10.

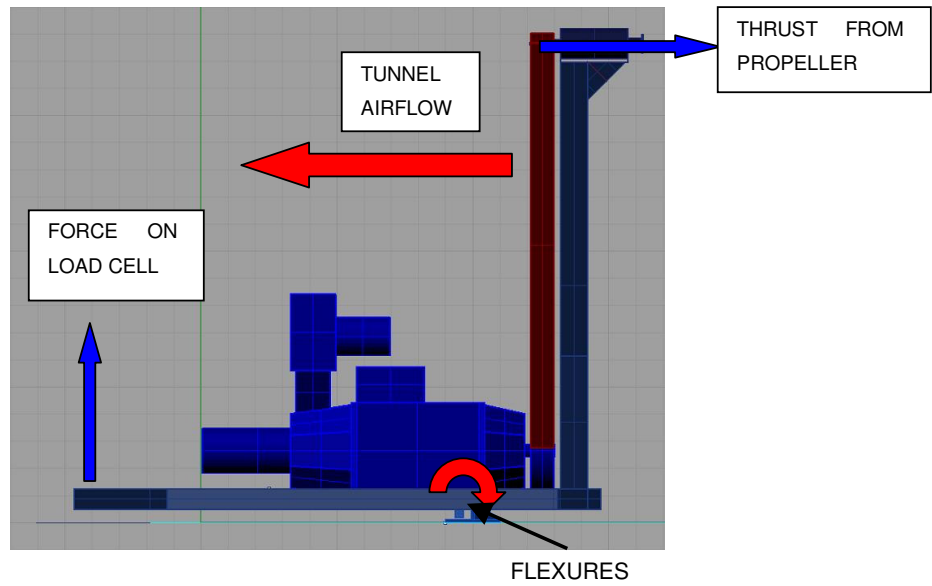


Figure 6.10 Conceptual design of propeller test rig

### 6.3. Manufacture of the Propeller Test Rig

The propeller test rig frame was manufactured largely of rectangular steel tubing including the vertical tube that supports the propeller bearing housing, see Figure 6.11.

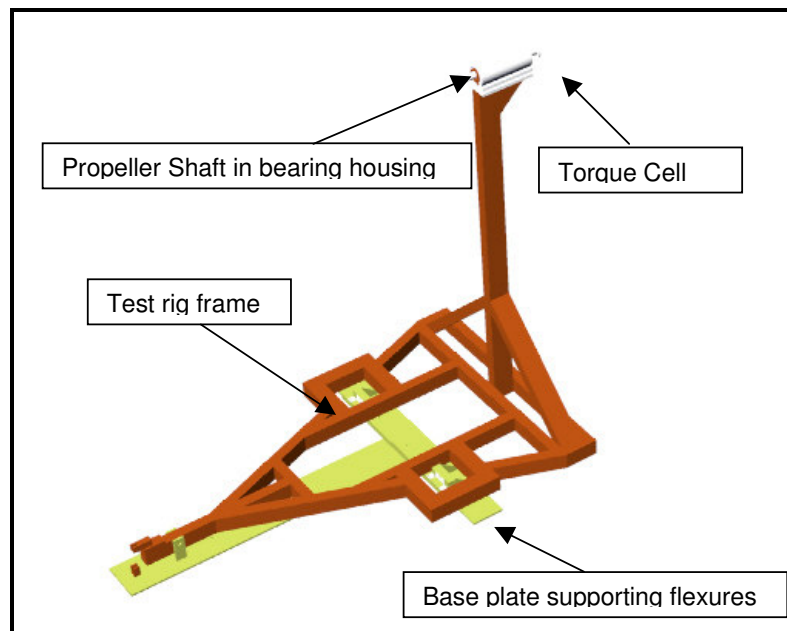


Figure 6.11 Propeller test rig frame

The test rig was equipped with a DC, brushed 75 kW Bull electric motor controlled by a Thorn EMI Automatic Stardrive controller with speeds variable from 0 to a maximum of approximately 2000 rpm. The propeller shaft is driven through a 85 mm wide Powergrip GT2 toothed belt drive from a 116-toothed pulley to one of 30 teeth, providing a 3.87:1 speed step-up ratio. The maximum available propeller test speeds attainable are over 7500 rpm, sufficient for testing of small UAV two stroke engine propellers for the UAV industry and far above the structural capabilities of the current propeller. For safety reasons the functionality of the speed control was tested before mounting the propeller.

The electric motor was mounted as low as possible in the frame (85 mm off the wind tunnel floor) to ensure that it did not protrude into the wind tunnel airflow. Belt tension was adjusted by adjusting the height of the propeller shaft bearing housing of the top tube. The offset of the propeller shaft from the wind tunnel centre line was typically of the order of less than 20 mm vertically with the belt at operational tension. The driven (top) pulley is fitted with flanges on both sides to ensure the tracking and hence retention of the toothed belt on the larger, unflanged pulley mounted on the motor.

The motor cooling fan housing was positioned on the top of the drive motor at a height just below the inlet lower lip but possibly not low enough to rule out its having an effect on the drag tare values. See Figure 6.12.

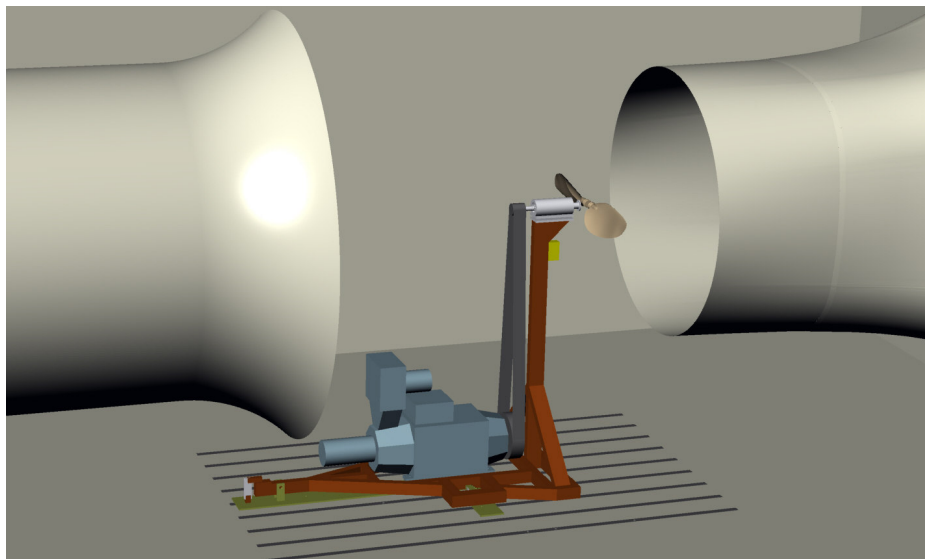


Figure 6.12 CAD rendering of propeller test rig installation in 2MWT

The propeller test rig assembly was also designed in Rhinoceros<sup>®</sup> version 3.0, and electronically transmitted to the manufacturers for manufacture and assembly. No paper drawings were created and as Rhinoceros<sup>®</sup> does not have the capability to produce

detailed drawings only rudimentary dimensioning was added. Details of the test rig geometry can be found in Appendix F.

### 6.3.1 Propeller Drive Shaft

The propeller drive shaft was designed specifically for small UAV propeller testing with a maximum torque of 50 Nm. Stress calculations were made with respect to the combined loading of the propeller torque and the offset lateral load due to the belt tension on the opposite end (Struthers, 2003). The shaft was designed to interface via an SAE 2 propeller flange with the rear of the load cell, the other end supported the driven pulley. The belt and pulley sizing was carried out with the testing of larger propellers up to a power of 75 kW in mind, whereupon only a larger shaft would need to be manufactured. Details of the shaft stress calculations can be found in Appendix G.

### 6.3.2 Flexure Design

The main test rig frame and engine was hung from four flexures manufactured from 316L stainless steel, see Figure 6.13. These were attached to the test rig cross member through dowel pins. A single, central bolt kept each flexure in place. The motor frame was constrained in the axial (thrust/drag) direction by an additional four horizontal flexures, two per side. See Figure 6.14

The stress calculations are to be found in Appendix G.



Figure 6.13 Close up detail of flexures

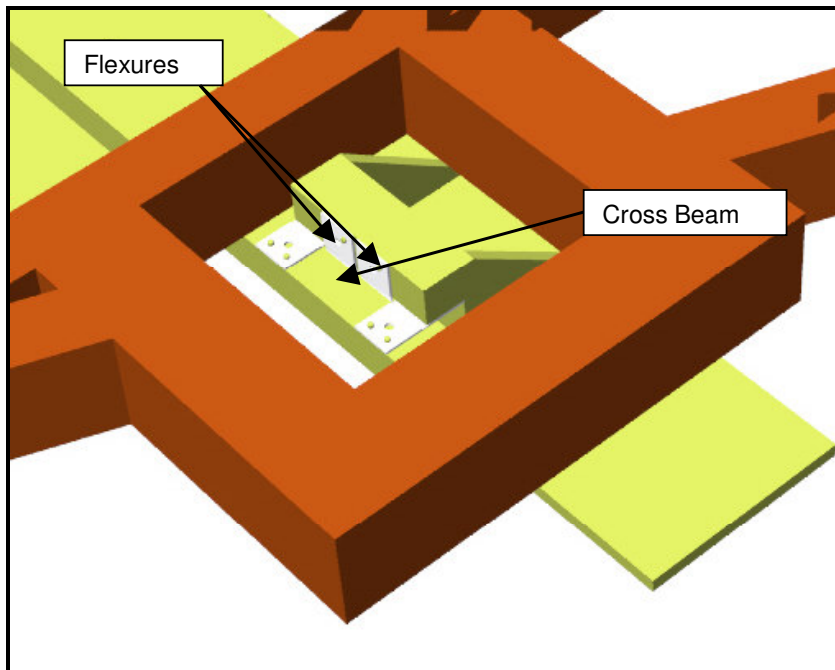


Figure 6.14 Base plate and test rig cross beam supported by flexures

### 6.3.3 Thrust measurement

A 750 N load cell mounted at the rear of the structure was used to record the propeller axial thrust loads imposed on the rig. A 5 kg mass was mounted on the front of the rig to ensure that the load cell at the rear was loaded in tension at all times to avoid possible hysteresis due to imperfect fitting of the rear pins.

A pin passing through the rear end of the test rig frame and two vertical supports protect the flexures from damaging deflections due to accidental loads applied to the frame or during transportation of the frame with the load cell removed.

The heavy-duty power cables from the motor were routed from the test rig via a floor mounted bracket to the speed controller. The effect of the stiffness of the cable on the thrust measurements was reduced through looping the cable once between the motor and the bracket and positioning the bracket in line with the flexure hinge line. The thrust calibrations were carried out with the motor cables in place.

#### 6.3.4 Fairing geometry

A fairing with a cross sectional shape created from the NACA 65012 aerofoil section, was manufactured from expanded Polystyrene covered with an adhesive vinyl skin. This was mounted on the vertical frame support member to reduce the overall drag of the frame and the magnitude of the tare corrections, improving accuracy of the thrust readings.

The maximum thickness point of the section was placed at the rear of the torque cell conditioning box that was mounted at the front of the vertical support. The trailing edge of the vertical fairing fitted between the two drive belts.

This fairing was not large enough to cover the drive belts situated behind the vertical strut but their drag was expected to be relatively small as the frontal aspect of their exposed portions was relatively small. During the initial wind tunnel tests without the fairing there was limited lateral movement of the belts from the airflow influence even at maximum tunnel speed.

The top bearing housing fairing and spinner were also formed from high density expanded polystyrene shaped to the profile of the top surface of a NACA 64015 series aerofoil section rotated about its chord line. This fairing was attached to the top bearing housing through the use of double sided adhesive tape.

A spinner manufactured from high density expanded polystyrene without any covering material was fitted to the propeller hub to reduce its drag and influence on the drag tare corrections. The spinner was fitted 5 mm upwind of the main fairing and mounted on the propeller hub, see Figure 6.15.

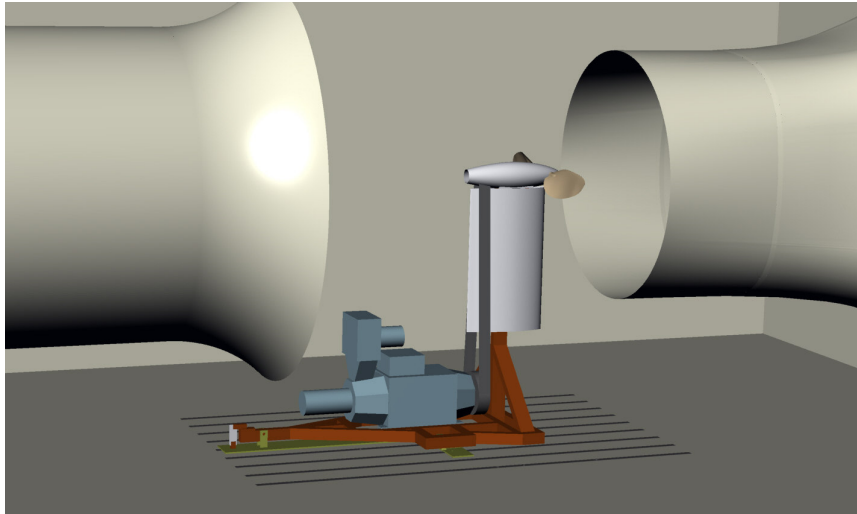


Figure 6.15 CAD rendering of the propeller test rig with fairing installed in the 2MWT



Figure 6.16 View of the propeller test rig partial installation in the 2MWT

### 6.3.5 Torque Measurements

Due to project budgetary constraints the manufacturing of a custom two-component load cell measuring thrust and torque transmitted at the propeller flange could not be considered. Instead a commercial torque cell and rotational speed sensor (model TS10) was acquired from a local manufacturer, Libra Measuring Instruments CC.

The torque transducer is fitted between the propeller drive shaft and the propeller, its load cell transmitting a digital RF signal to a larger diameter pick-up unit that is coaxially mounted close to but not contacting the load cell. The cables from this sensor run over a short distance to a conditioning box from where the output cables are routed via the cable attachment on the floor to a display unit. The conditioning box was mounted within the vertical support fairing in front of the vertical support.

The torque cell was designed for the testing of larger propellers with torques of up to 130 Nm. As the peak torque of internal combustion engines at the power stroke is up to three times the mean torque, the maximum torque capacity was specified to be 390 Nm. This was far in excess of the 30 Nm torque expected from the UAV wind tunnel model propeller driven by an electric motor. The manufacturers indicated that the torque cell resolution that could be expected at 30 Nm was 0.1 Nm. This would be approximately one third of a percent of the maximum expected load but would be a higher percentage of the lower loads.

## 6.4. Calibration of Load Cells

### 6.4.1 Torque Transducer

The torque cell was calibrated at the South African National Metrology Laboratory (NML). The results of these tests are presented in Appendix C

### 6.4.2 Thrust load cell

The calibration of the thrust load cell mounted at the rear of the test rig was carried out through the application of calibrated loads applied to the centre of propeller flange.

Calibrated masses were added to a weight tray supported by a thin steel cable that passed over a pulley that pivoted about a knife-edge, to the centre of the propeller hub. The voltage supplied to the strain gauged load cell was measured using an HP 3456A digital voltmeter to be 10.000 volts before calibration and 10.003 volts afterwards.

At every load case fifty readings were taken over a space of approximately 5 seconds and then averaged to produce the final result. Five sets of readings were taken at each load. The loads were increased in 10 kg increments up to 60 kg and then carefully reduced in the same 10 kg increments. Zeroes were taken at the start and end of the calibration. The results of the calibration can be found in Appendix C. The calibration coefficient was determined to be 0.0508 mV/N.

The repeatability between readings appeared to be extremely good, sufficiently so for the current tests. The hysteresis exhibited between the increasing loadings and the decreasing of the load was assumed to be partly due to some bluntness of the knife-edge system.

## **6.5. Electromagnetic Interference effects**

The electromagnetic interference (EMI) effect of the motor power supply on the thrust readings was investigated. The output of the thrust load cell was monitored while the motor power supply and the motor were turned on independently. No changes in output were noted.

It wasn't possible to measure any EMI effects on the torque cell or conditioning box due to the high update frequency on the electronic display. It was also not possible to connect to the raw data emitted from the torque sensor.

## **6.6. Data Acquisition**

The torque cell and thrust load cell voltages were captured by a HP 3456A digital voltmeter. To reduce the effects of noise and vibration on the results, one hundred readings were taken and averaged by the voltmeter at each data point. The voltages were converted into physical units through the application of the calibration coefficients as described previously. The results were both stored on a PC and simultaneously displayed on the data acquisition system.

## **7. WIND TUNNEL TESTS**

### **7.1. Correction Factors - tare and Interference**

Any model supports inserted into a wind tunnel test section affect both the free flow of air and cause drag themselves. The former is called *interference* and the latter *tare*. Corrections are required to the force and moment readings due to these two factors.

The interference drag is usually isolated by testing the model both upright and inverted in the test section and utilising mirrored dummy struts. In the case of a propeller test this interference would induce a normal force component. As normal force was not being measured, tests requiring dummy struts were not carried out.

The flow of air through the supports onto the models can have the effect of causing flow separation on the strut or model which not only can cause a drag increase but also unsteady loads making accurate force measurements more difficult. Whether this would be a large factor in the downwash of a propeller remained to be seen.

### **7.2. Description of the First Wind Tunnel Test Series**

Two wind tunnel test series were carried out in the course of this work. Equipment failures during the first test series necessitated a second series of tests during the following financial year.

#### **7.2.1 Wind Tunnel Set-up**

The propeller test rig was mounted in the tunnel through the attachment of its base plate to the mounting slots in the test section floor. The propeller tip path plane at the local quarter chord was positioned within an accuracy of approximately 10 mm to a position 500 mm rear of the inlet lip. This is close to the most rearward position possible limited only by the base plate support moving beyond the rear limits of the floor support rails. The effect of the close proximity horizontally of the wind tunnel inlet on the propeller in-flow pattern was a cause for concern.

The rig was originally designed to position the centre of the propeller shaft on the wind tunnel centre line and the belt tension was to be adjusted through the vertical movement of the electric drive motor. However it was discovered that the lifting or lowering of the motor was difficult due to its large mass and the decision was made to allow some vertical adjustment to take place at the head of the test rig. The final position of the propeller rotational axis was a relatively insignificant 20 mm below the tunnel centre line.

Vertical and horizontal wires were positioned at the inlet and diffuser faces defining the centre of each duct. Horizontal wires were then placed between these wires on either side of the top bearing housing in order to assist with the alignment of the rig. The vertical alignment of the test rig head housing was measured using an inclinometer to be just 0.1 degrees from horizontal. The propeller efficiency typically reduces approximately as the cube of the cosine of the misalignment angle (Larrabee, 1984). This inaccuracy would result in a negligible error for the planned tests.

The vertical support appeared to be slightly twisted as the base plate was rotated slightly more than a degree clockwise in azimuth on the tunnel floor to align the top housing in line with the wind tunnel centre line. This rotation in itself would induce no significant error in the thrust readings due to the offset angle of the flexures from normal to the tunnel centre line as the rotation was carried out prior to the calibration of the thrust load cell.

## 7.2.2 Tare and Interference prediction / measurements

Following initial functional tests of the test rig, during which the drive belts were observed to remain reasonably steady, a vertical frame fairing and a top bearing housing fairing were fitted.

The propeller hub was initially installed without the blades and the spinner was mounted. The openings in the ends of the hub were taped closed to reduce the additional drag that they would have created as discussed by Barber (1983). The tunnel was run at various speeds from 4 m/s to the maximum tunnel speed of 30 m/s. The load cell readings were captured by the HP 3456A digital voltmeter under the control of the HP 3497A data acquisition system. This in turn was controlled by a PC running a custom LabView ® application that displayed the data at each test point. 100 readings were taken at each test point and the results averaged in the data acquisition system. At least two sets of readings were taken at each test point.

As the tunnel airspeed was increased to speeds above 16 m/s the drive belts began to both oscillate and twist about their longitudinal axes. The effect of this action caused a noticeable increase in the magnitude and variability of the drag, especially at the higher speeds where the belt movement and shaking became quite pronounced.

Previously at the higher tunnel speeds this belt behaviour had not been observed. It was observed that with the fairings mounted, the airflow was directed over the drive belts at an angle so that they generated a significant amount of force normal to flow direction causing the belts to shake inwards and outwards from the fairing. The result of this belt flapping motion is that the tare corrections were not only larger than expected but also had a greater temporal variation despite the averaged readings.

The variations in and the size of the tare corrections had a large influence on the accuracy of the final results, in particular at the higher test speeds where the test propeller thrust had been reduced to values close to zero. The variation in the tare corrections was of the order of 5 N.

Time and project budgetary constraints at the time precluded the possibility of either modifying the fairing geometry or in any other way reducing the aerodynamic and possibly inertial effects of the oscillatory belts on the readings.

### 7.2.3 Prop-wash effects on tare corrections

It was assumed that the increased air velocity imparted by the propeller over the fairings would increase the drag tare corrections. In order to calculate this effect, the spreadsheet version of the propeller analysis code was used to determine the induced axial velocity factors.

The pitch angle for each test run was entered followed by the various velocities from the wind tunnel tests. The average induced velocity factor over the region of the blade from  $r/R = 0.2$  to the tip was determined and the axial component multiplied by the velocity in the results spreadsheet. This product was added to the wind tunnel velocity term. This velocity was used in the tare drag calculations. The correction is naturally largest when the thrust from the propeller is smallest i.e. at the higher advance ratios.

### 7.2.4 Test Methodology

The propeller was tested at two rotational speeds of 800 rpm and 1200 rpm at a range of tunnel speeds from 4 m/s up to 30 m/s resulting in an advance ratio variation of between 0.068 and 0.40 a wider range than the 0.12 to 0.39 required to model the propeller over the simulated HALE UAV mission.

The wind tunnel test plan included testing the propeller blades at positive pitch angles of 0, 4 and 8 degrees followed by -4 degrees at the lower rotational speed. The 2 degree positive and 2 degree negative angles were later added to provide more data about the zero pitch angle design point. These runs were then repeated at the 1200 RPM rotational speeds. Finally -8 degree and -12 degree pitch angles were tested as was a 12 degree pitch angle. The pitch angles of the blade were measured at the 70 % radial position on the blades which is the internationally accepted radial position at which propeller pitch angles are measured.

Before each test, the blade pitch angles were set in the adjustable hub. This was done utilising a calibrated hand-held Pro3600 Digital Protractor inclinometer capable of a 0.1 degree resolution. A chord wise line marked on each propeller blade at the 70 % radial position ensured the consistent placement of the inclinometer. The inclinometer's internal reference zero was utilised as there were no level reference surfaces in the wind tunnel building.

In order to accurately ascertain the blade's angle, the angle of a line tangent to the blade lower surface (not the blade chord line) was measured at the 70 % radial position in the CAD geometry to ascertain the required inclinometer reading related to a specific pitch angle. That angle was determined to be 17.8 degrees from the tip path plane. When setting the pitch angle of a blade in the hub, a reading using the inclinometer placed on the chord wise tangential line of 72.2 degrees from horizontal would translate into a pitch angle of zero.

The adjustment of the propeller blade pitch angles was made manually using the inclinometer. A setting angle of within 0.1 degrees of that required for the particular test was generally achieved after the hub bolts were tightened. The actual blade angles were measured and recorded for each test run and can be seen at the top of the wind tunnel test data sheets in Appendix D.

The wind tunnel airspeeds were varied from the lowest speed, being that induced by the propeller at the required test rotational rpm, up to and slightly beyond speeds at which point the net thrust was estimated to have passed through zero. This point was estimated during the tests as the thrust reading displayed on the monitor was not corrected for the

rig drag tare values. When the propeller torque decreased through zero the motor would allow the rotational speed to be driven by the propeller to values greater than that set by the controller. As this had safety implications the displayed thrust data was closely monitored during the tests.

Once the maximum test speed had been reached, the velocity was decreased through the same increments until the tunnel could be turned off. The last reading was recorded with the tunnel fan stopped and again after a further delay of 30 seconds to allow any further residual airflow to dissipate.

For safety reasons the power to both the propeller test rig motor and the wind tunnel motor was turned off between tests. During this time the propeller and hub would be inspected and any insect debris on the propeller blade leading edges was removed. Insect debris was seldom found on the blade leading edges over the course of the tests.

The test procedure was typically as follows:

1. Zero-load readings were recorded from the two airspeed pressure transducers, the air temperature thermocouple and the thrust load cell with the tunnel and propeller test rig motors off.
2. The propeller test rig motor was started and the speed set on the controller to produce a propeller speed close at the required 800 or 1200 rpm required by that particular test. The lowest possible wind tunnel speed at which tests were carried out was that induced by the propeller for that particular test run.
3. The wind tunnel main drive motor was started and the tunnel speed increased in 2m/s increments between test points. The wind tunnel speed was consistently held within 0.2 m/s of the test point speed for the duration of each test. An approximate speed was displayed on the data acquisition PC monitor.
4. The actual wind tunnel airspeed was recorded by a data acquisition system developed for the wind tunnel. This data was written directly to the PC hard disc, the names of these data files being captured on the test sheets.
5. Once full wind tunnel speed was attained the airspeed was reduced in 2 m/s increments until the tunnel motor was turned off. The speed induced by the propeller was allowed to stabilise.
6. Finally the propeller was stopped and after a delay for the wind in the wind tunnel to stop moving, zero readings were again obtained.

The TS10 torque transducer operated intermittently during the tests as did the rotational speed sensor with neither producing any useable data throughout the wind tunnel test

series. The manufacturer could not solve the problem during the week leading up to the allocated time for the wind tunnel tests. Due to this failure the propeller rotational speed was set at a speed estimated from the controller setting dial and then verified with an optical, portable tachometer at every second test point. During the day the contrast between the outside sunshine beyond the wind tunnel inlet and the passing propeller blade was sufficient for the tachometer to register the rotational speed. At night an aluminium strip was placed at the root, near the trailing edge to minimise aerodynamic effects on one of the blades to reflect the tachometer light.

The propeller test rig drive motor maintained a consistent rotational speed despite changes in its load due to the variations in the wind tunnel speed. Variations in motor speed were typically less than 1% of the set speed over the complete wind tunnel speed range. The electrical current drawn by the motor was noted at each test point in the hope that an estimate of the motor torque could be calculated. This was not achieved as it was not possible to calibrate the motor within the allocated tunnel test slot time.

Being an open circuit wind tunnel, the results can be affected by the outside wind and weather. Fortunately during the three day test period the outside weather conditions were essentially windless and dry.

### **7.3. Test Matrix**

The record of the wind tunnel tests is displayed in Table 7.1 below. The data acquisition software allocates the test numbers sequentially starting with an increment to the previous test's final number.

Table 7.1 Test record of first test series

Test No.	Pitch Angle	Rpm	Comments
1032	-	-	Test file to confirm data recording
1034	-	-	Initial tare run
1035	0	800	Tare run with motor running at 800 rpm
1036	0	800	Zero pitch run
1037	4	800	
1038	8	800	
1039	-4	800	
1040	-	-	Test file to confirm torque cell functionality
1041	-4	800	Test of a few points with torque readings
1042	-4	800	Full test with torque readings
1043	-	-	Check on calibration values
1044	0	800	200 readings averaged for torque
1045	2	800	No torque readings
1046	2	1200	No torque readings
1047	0	1200	No torque readings
1048	4	1200	No torque readings
1049	8	1200	No torque readings, tests terminated
1050	-4	1200	No torque readings
1051	-8	1200	No torque readings
1052	-12	1200	No torque readings
1053	12	800	No torque readings, tests terminated
1054	-	800	Final Tare run

The two highest pitch angle tests at 1200 rpm, 8 degrees and 12 degrees were terminated before completion due to one of the blades altering pitch angle under inertial and aerodynamic loads in the hub during the test. The effect of the pitch change was observed when the slope of the 8 degree pitch angle, 1200 rpm case followed a more negative gradient above an advance ratio of 0.3 and after reaching an advance ratio of 0.4 followed a different return path to the lower advance ratios. The data for the 8 degrees 800 rpm case had shown no such trend. The data for the 12 degrees 1200 rpm case follows a similar trend with the change in slope starting with the last data point and returning along a path similar to the 8 degrees case. In both of these cases the one blade had rotated to a lower angle of attack.

There are three moments imposed on the blade during rotation, two from the centripetal acceleration and one from the typically negative pitching moment of the aerofoil (Bass,

1984, Bass et al 1985). The net effect is typically to reduce the pitch as was seen during the tests. No damage was caused to the test rig through either incident and the tests were terminated as soon as the offset data had been noticed on the display.

#### 7.4. Wind Tunnel Test Results

The results of the wind tunnel tests are presented in graphical form below in Figures 7.1 and 7.2 as plots of thrust coefficient against advance ratio for each of the tested pitch angles. The results are displayed on two separate graphs. Pitch angles from  $-12$  to  $0$  degrees are shown on the first graph and  $2$  to  $10$  degrees on the second. The data points are from both the increasing and decreasing advance ratios. This data is presented in more detail in tabular form in Appendix D, Tables D1 to D14.

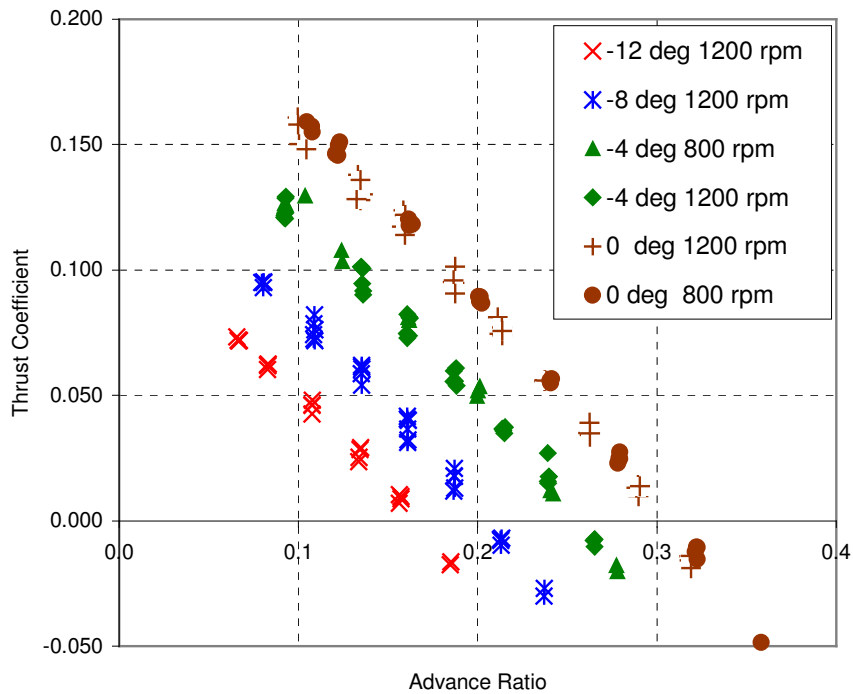


Figure 7.1 Measured propeller thrust coefficients for pitch angles of -12 to 0 degrees

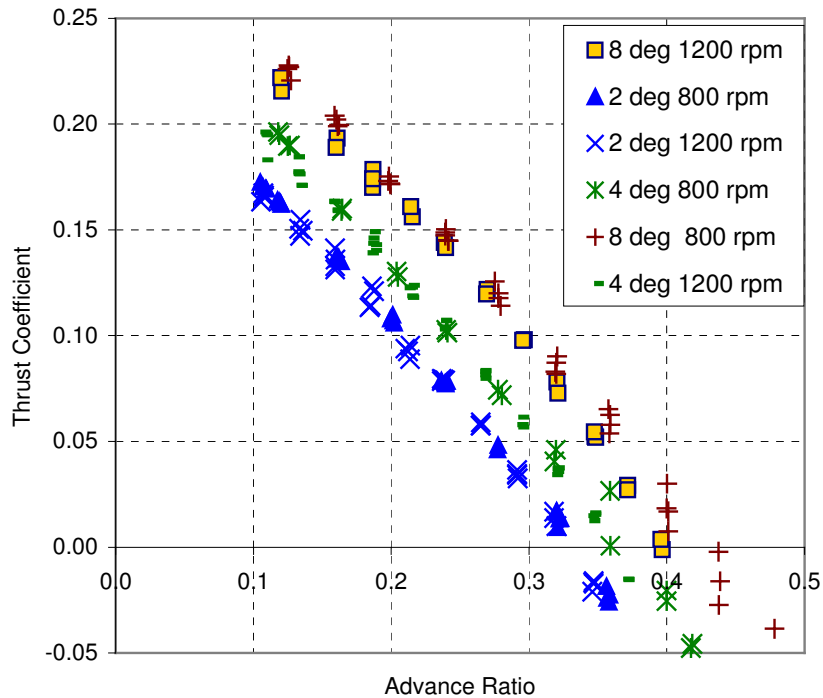


Figure 7.2 Measured propeller thrust coefficients for pitch angles of 2 to 18 degrees

The results from the same pitch angles but different propeller speeds appear to be very similar in value. The larger differences between the curves appear typically at the lower thrust coefficient values at higher advance ratios.

The scatter of the data is most likely due to the effects of the buffeting of the drive belts and while very noticeable during the tests it has had a smaller than expected effect on the final results. At the lower pitch settings, the scatter appears to be similar throughout the thrust coefficients and advance ratios with possibly a small increase in the mid-range of the thrust coefficients. For the higher pitch setting the scatter increases at the lower thrust coefficients and higher advance ratios.

## 7.5. Comparison between Theoretical and Predicted Results

Only thrust data is presented from the first test series due to the failure of the torque load cell equipment. The results from  $-12$  degrees to  $0$  degree pitch angle are plotted in Figures 7.3 and from  $2$  degrees to  $8$  degrees pitch angle in Figure 7.4. In both figures the

predicted thrust coefficient values are plotted as the continuous line and the wind tunnel test data as discrete points.

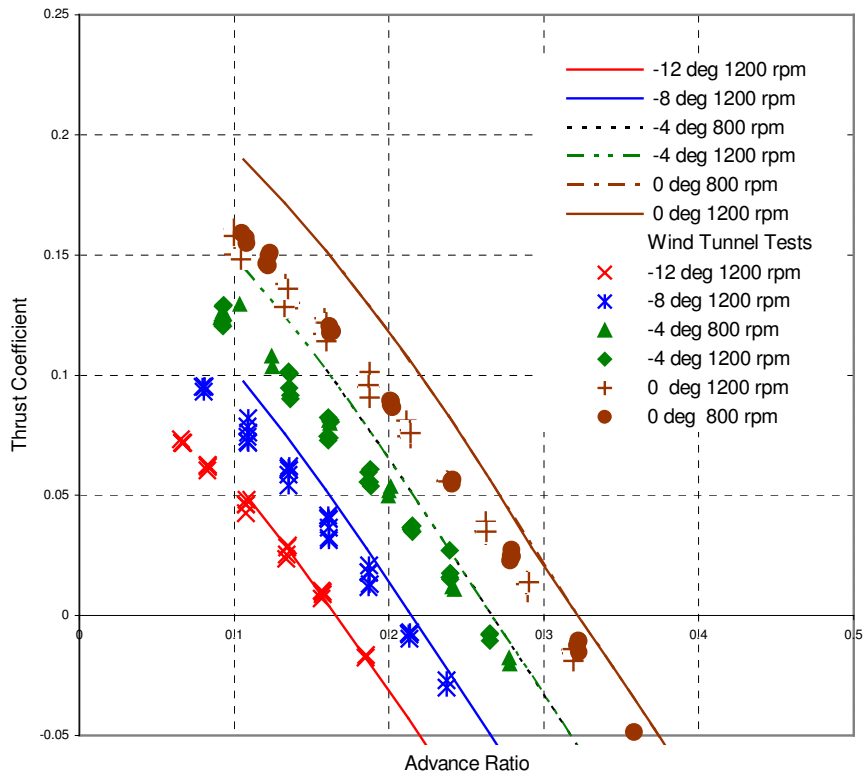


Figure 7.3 Comparison of predicted and measured propeller thrust coefficients for pitch angles of -12 to 0 degrees

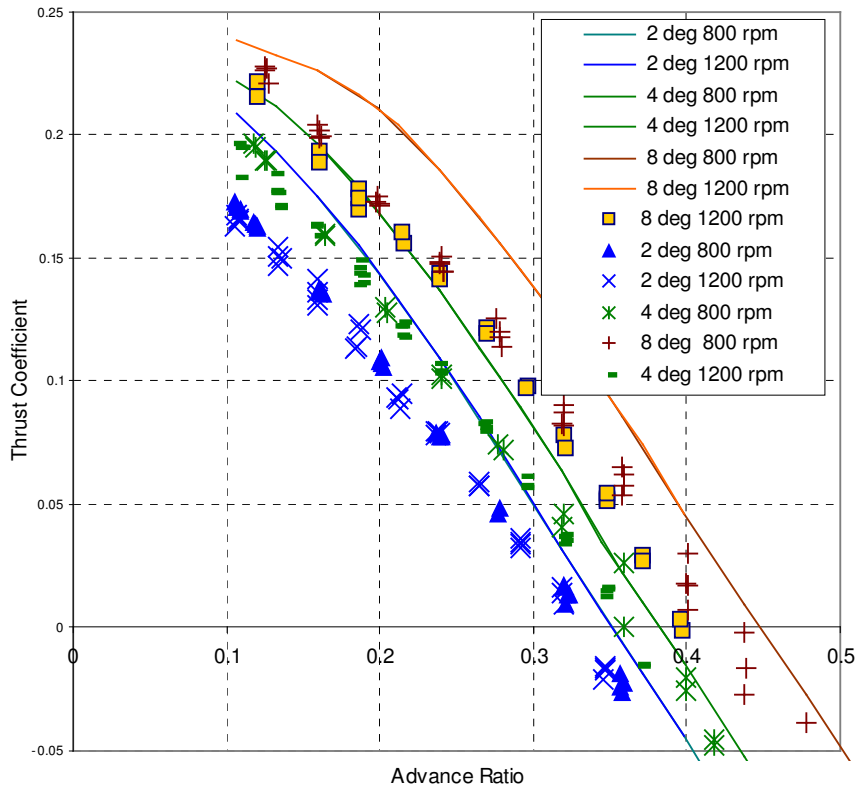


Figure 7.4 Comparison of predicted and measured propeller thrust coefficients for pitch angles of 2 to 8 degrees

There are noticeable differences in the predicted and measured thrust coefficient curves. At the higher pitch angles and higher thrust coefficients the error between the predicted and measured data is at its largest. The gradient of the thrust coefficient of the predicted curves are also greater than those of the measured. This would typically indicate that the results of the predictions are of a higher aspect ratio blade than that of the tested blade that the three dimensional effects on the blade geometry are sufficiently large to cause this effect.

## 7.6. Propeller Geometric Error

As the blade geometry had been verified against the CAD geometry the design was compared against the original propeller geometric data. Here an error in the chord wise dimensions of the blades was observed.

When the propeller diameter was reduced from the 1.7 m to 1.2 m diameter for reasons previously explained, the blade chord lengths were scaled down from 850 mm radius to 600 mm. During this scaling process the original radial chord distribution of the 850 mm blade was erroneously retained. This type of high altitude propeller design inherently has a broad chord due to the low air density, an extreme case being those used on the Pathfinder UAV (Bieryla, 2007). For that reason the relatively broad chord did not appear to be obviously incorrect and the relative increase in width was not discovered until after the wind tunnel tests were completed and the data analysed.

The difference between the manufactured geometry and the as designed geometry is illustrated in Figure 7.5.

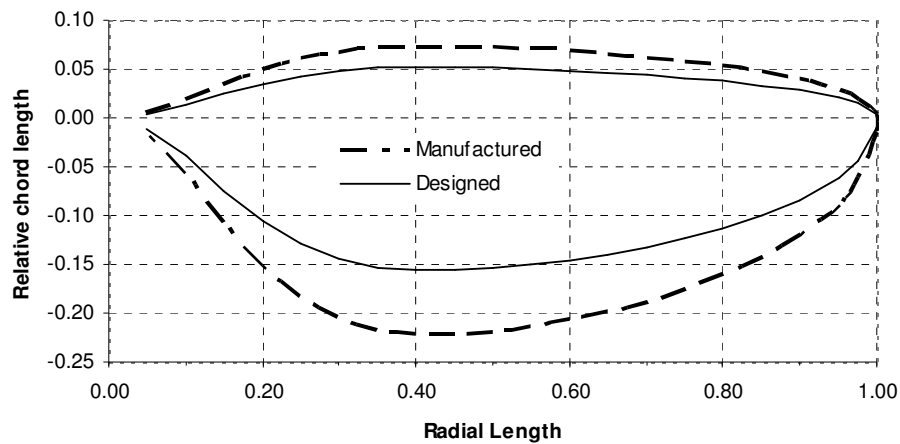


Figure 7.5 Comparison between designed and manufactured blade geometries

The manufacture of new propeller blades could not be considered due to the lack of availability of a wind tunnel test slot within the remainder of the year in which funding was available and no further funding was available for the manufacture of a new blade. It was thus decided to run the performance prediction code for the new geometry and to compare against the performance of the propeller as tested.

The propeller geometry analysed in the modified mission simulation code was adjusted in chord length to represent the manufactured blade. Fortunately as the chord length distribution is an inverse function of design lift coefficient, modification thereof has the effect of a linear alteration of the chord independent of any other variables. The corrected chord wise distribution in the designed propeller was attained through reducing the local design lift coefficient by the ratio of the two blade lengths. The new chord lengths were

compared with that of the actual propeller and differences of less than 2 mm at all stations were observed.

It is important to note that the blades, as manufactured, were still of the minimum induced loss design as only the local aerofoil section design lift coefficients were altered. The evaluation of the design and analysis methods could still be carried out. The expected wind tunnel performance predictions were repeated using the modified mission simulation code for the adapted propeller geometry.

The agreement between the measured data curves for different propeller speeds at the same pitch angle and advance ratio was greatly improved. A more detailed comparison will be made for the second set of tests.

## **7.7. Second Wind Tunnel Test Series**

Due to the lack of the torque data required to complete this work, a second wind tunnel test series was planned for the following year. This opportunity was utilised to modify the test rig to improve the quality of the data.

### **7.7.1 Modifications to Test Rig for Second Test Series**

Failure of the torque transducer system during the first test series necessitated a second series of tests that took place the following year once funding had been approved. The propeller test rig was modified during the period leading up to the second test series.

During the first wind tunnel test series the drive belts were observed to oscillate in the airflow. For the second series of tests a larger vertical fairing was created from vinyl covered expanded polystyrene. The cross sectional shape was created from the NACA 65012 aerofoil section, thickened by 10 % to ensure the containment of the two drive belts. The aerofoil's maximum thickness point was located at the position of the drive belts, see Figure 7.6.

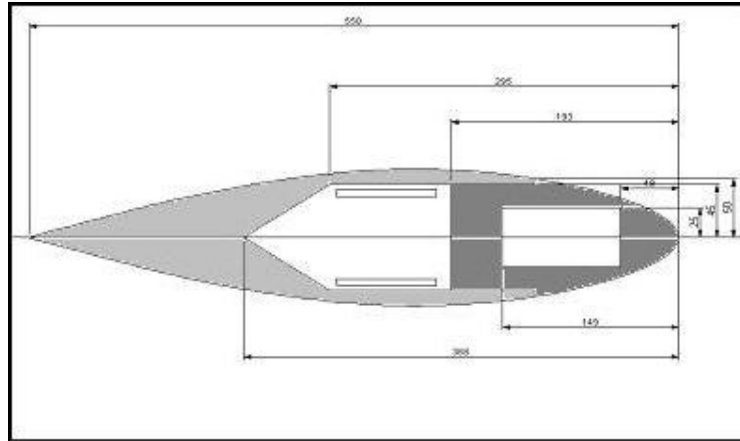


Figure 7.6 Cross section through new vertical fairing

The torque cell conditioning box could not fit within the new fairing in its original position and was moved from the front of the rig vertical support to a position behind, between the drive belts where it was housed within the new fairing. The top bearing housing fairing and spinner were retained from the previous test series.

Figure 7.7 illustrates the new guide rollers that were installed behind the vertical support directing the drive belts within the fairing.

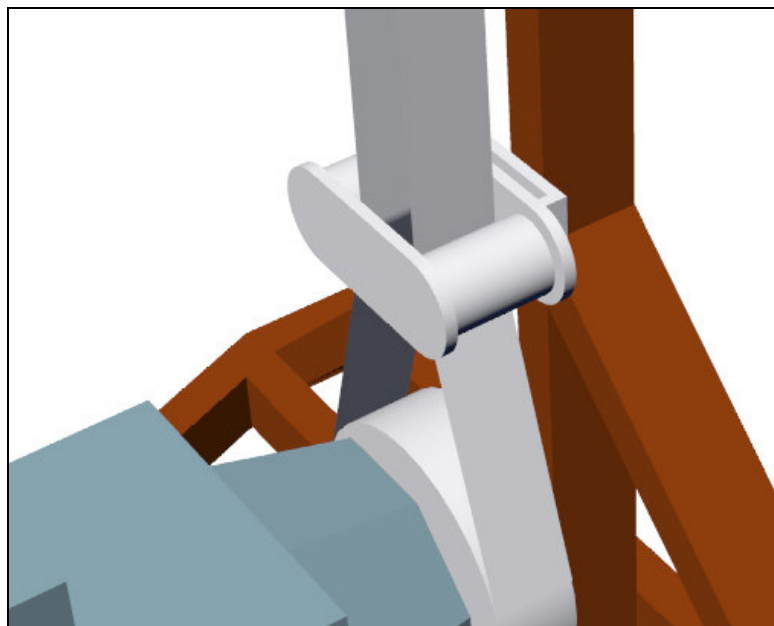


Figure 7.7 Rollers directing the drive belts behind the vertical support

The motor rear housing was rotated so that the fan was positioned on the side of the drive motor, moving its housing further out of the airflow to reduce any effects on the drag tare values, see Figures 7.8 and 7.9.

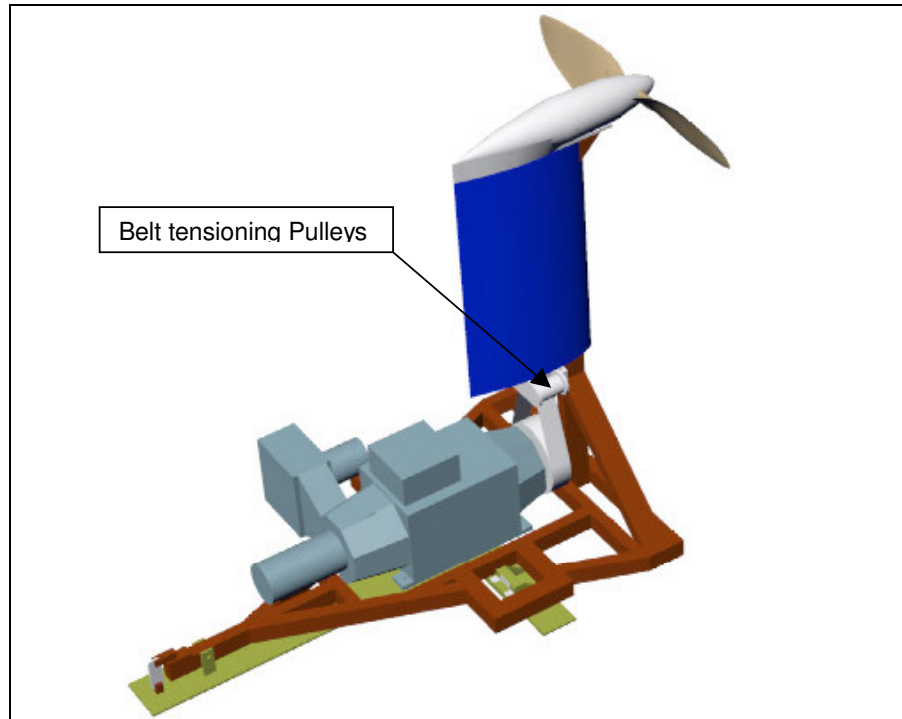


Figure 7.8 CAD rendering of the propeller test rig with fairing

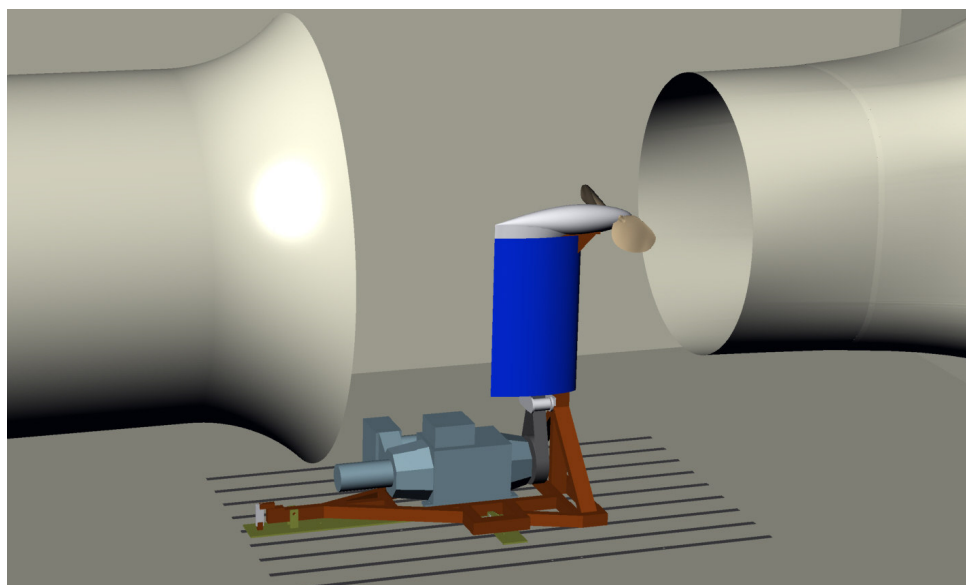


Figure 7.9 CAD rendering of the installed new test rig geometry

### 7.7.2 Wind Tunnel Set-up

The propeller was again positioned at 500 mm  $\pm$ 10 mm from the rear of the tunnel inlet so as to allow for direct comparison with the previous test series. The angular offsets of the rig to the tunnel centre line were again corrected to less than 1 degree of azimuth.

A different load cell was used for thrust measurement during this test series due to its being installed on the test rig and the original load cell being unavailable. The calibration of the new load cell had been carried out on the test rig on a previous commercial propeller test. The voltage applied to the new load cell during this calibration was 12.00 volts. This was once again monitored by the HP 3456A digital voltmeter. The gradient of the calibration curve, now 0.04102, had already been incorporated into the data acquisition program. The calibration data can be found in Appendix C.

### 7.7.3 Tare and Interference prediction/measurements

The propeller hub was once again installed without blades and the spinner mounted with the openings in the ends of the hub closed off. The tunnel was run at speeds increasing from 4 m/s to 30 m/s. The load cell output was captured on a HP 3457A digital voltmeter under the direct command of the wind tunnel data acquisition program running in LabView<sup>®</sup> on a local PC. Readings were taken at each test point at approximately 3 Hz over a twenty second interval and those results averaged.

The magnitude of the tare corrections was typically less than one third of those recorded in the previous test series at high tunnel speeds and less than one half of those recorded at lower tunnel speeds. In the previous test series the drag coefficient increased with increasing tunnel speed due to the increased oscillation of the belts.

There was once again a small increase in the drag coefficient of the new fairing with increasing tunnel speed. This increase, albeit counter-intuitive, was small and is believed to come from the somewhat flexible fairing being deformed by the surrounding low pressure. At higher tunnel speeds the lateral deformation of the fairing could be observed. It is speculated that the small drag coefficient increase could have resulted from the earlier separation of the flow from the rear of the fairing as a result of the steeper pressure gradients brought about by these deformations. These effects created no significant errors in the wind tunnel tests as these values were the corrections that were consistently removed from the measured data.

#### 7.7.4 Propeller induced velocity effects on tare corrections

The velocities induced by the action of the propeller were again computed only this time the mission code was modified to produce the radial distribution of induced velocity ratios at each tunnel speed. The average of these ratios was multiplied by the respective velocity and added to the total velocity from which the tare corrections for the support were calculated.

As the magnitude of the tare corrections was reduced from that of the previous test series, the effect of the induced velocities on these corrections was relatively minor.

#### 7.7.5 Test Methodology

Due to time and budget constraints the tests in the second series were carried out only on five pitch angles. During this time some resonance of the test rig vertical support was observed at the 1200 rpm propeller speeds that appeared to increase the scatter in the thrust data. A new propeller test speed of 1000 rpm was chosen for the second test series. It was observed that there were insignificant differences in the propeller thrust coefficient data between the tests previously carried out at 800 rpm and 1200 rpm, (Figures 7.4 and 7.5) illustrating that the Reynolds number effects on the results over this speed range appeared to be insignificant. The lack of Reynolds number effects could also be an indication of the extent of laminar flow on the aerofoils not being achieved either through surface finish on the propeller or through turbulent levels being too high in the test section.

The second test series covered a smaller number of propeller tests due to budget constraints. Tests were conducted at pitch angles of  $-8^\circ$ ,  $-4^\circ$ ,  $0^\circ$  and  $4^\circ$  as these covered most of the expected pitch angle range during the UAV mission.

Once again the torque transducer did not function correctly despite being modified by the manufacturer to solve the problems encountered during the previous test series. Two early shakedown tests were performed to test the equipment and in particular the torque transducer and speed sensor. During the first of these tests both the display of the torque and the recorded torque readings were showing large variations during a steady state test and the manufacturer was contacted to repair the system.

During the second shake down test the conditioning box displayed an error indicating that there was a problem with the connection to the sensor. Once again this problem could not be fixed by the manufacturer in the remaining time before the test slot was over. The decision was made to record the motor voltage supply and current draw at every test point and then determine the torque through the subsequent characterisation of the electric motor.

### 7.7.6 Motor Characterisation

During the wind tunnel tests the motor armature current and voltage were monitored via voltmeters connected to the motor power supply. Subsequent to the completion of the tests, a Prony brake, (See Figure 7.10) was manufactured consisting of a 218 mm diameter aluminium drum with mounting holes drilled to fit the propeller flange.

A 750 N load cell was attached between a floor-mounted frame and via ropes that passed over the drum to a weight cradle. Due to excessive wear the ropes were later replaced with a more wear resistant seat belt strap.

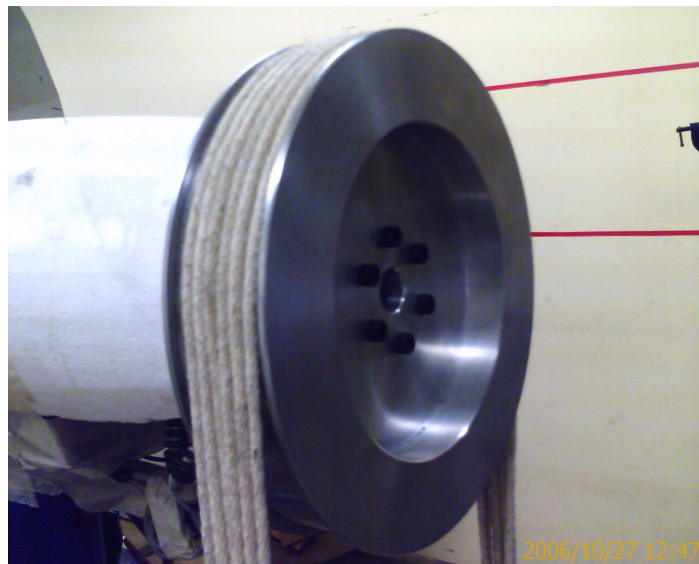


Figure 7.10 Prony brake drum mounted on propeller test rig

The motor was set to various rotational speeds while calibrated weights were added to the cradle increasing the torque. At each test point the motor armature current and

voltage and the motor tachometer voltage were recorded. The tachometer voltage was related to the drum speeds measured by means of a calibrated optical tachometer.

The aluminium drum had to be left to cool between successive tests especially at the highest test speeds where the power output from the friction was approaching 4 kW.

The current draw of the motor demonstrated an approximately linear relationship with the torque for a given rotational speed. Four speeds of nominally 400, 600, 800 and 1000 rpm were tested. The tests were terminated at the highest speed and load conditions when the heating of the seat strap became excessive to the point of damage to the aluminium drum.

The current draw at the lower rotational speeds was typically less than that of the higher speeds for a given torque. The results of these tests are shown in Figure 7.11.

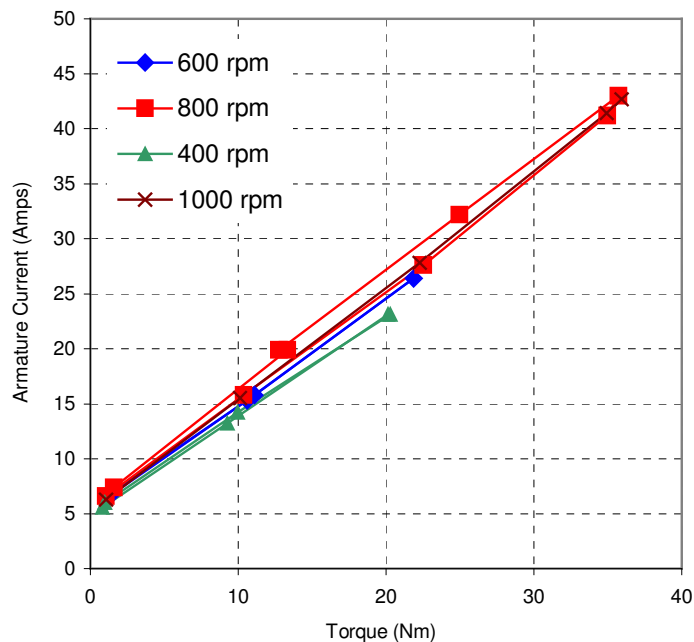


Figure 7.11 Motor torque versus measured armature current for various speeds

These tests provided the relationship of current to applied torque at various rotational speeds but could not provide the offset of the calibration curve due to the friction of the motor drive system. No consistent zero reading could be recorded by the Prony brake load cell either, due to this friction.

The motor was then run with no load applied to determine the no-load current of the motor at various rotational speeds. These currents are displayed in Figure 7.12.

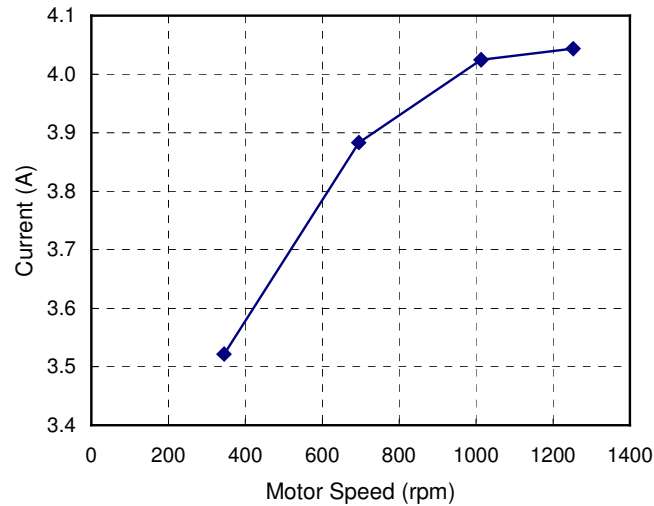


Figure 7.12 No-load motor current at various speeds

These values were combined to characterise the motor torque in terms of the measured current draw.

## 7.8. Torque Prediction

Having characterised the motor current against the applied torque, the torque values imposed by the propeller during testing could be ascertained. The product of these values and the rotational speed of the propeller provide the power absorbed by the propeller. These results are illustrated in the following section.

## 7.9. Results from the second test series

The correlations between the predicted and the actual thrust and power coefficients are not as close as expected possibly due to differences between the flow field induced by the propeller in the wind tunnel test section and the unconstrained flow field assumed in the predictions. The incoming flow field to the propeller is constrained by the tunnel inlet geometry to almost parallel streamlines as opposed to the converging inflow pattern of a propeller in isolation.

The wind tunnel pitot-static probe was positioned approximately 150 mm away from the side wall and 600 mm in front of the propeller disc. It is possible that the gradient of the velocities induced by the propeller in the wind tunnel could provide a different velocity reading from that through the propeller disc. The horizontal offset in the curves at zero thrust and power coefficients in Figures 7.13 and 7.14 respectively are possibly due to these induced velocity effects on the measured values of advance ratio as seen.

### 7.9.1 Thrust Coefficient

There is a reasonably close correlation between the predicted and measured thrust coefficient data from the second test series, Figure 7.13. At the higher pitch angles and higher advance ratios, the measured thrust coefficients are of the order of 10 to 15 percent lower than those predicted. The gradients of the measured thrust coefficient curves are almost identical to those of the predictions. The results would correlate better if the thrust curves were adjusted to correct for the error in the advance ratio.

It was not possible to obtain experimental results at low advance ratios due to the air velocity induced by the propeller in the wind tunnel. The predicted thrust losses due to local stalling of the blades at the lower advance ratios could thus not be modelled.

The scatter in the data is noticeably lower than that of the previous test series due to the lower drag tare variability ascribed to the drive belts being within the fairing.

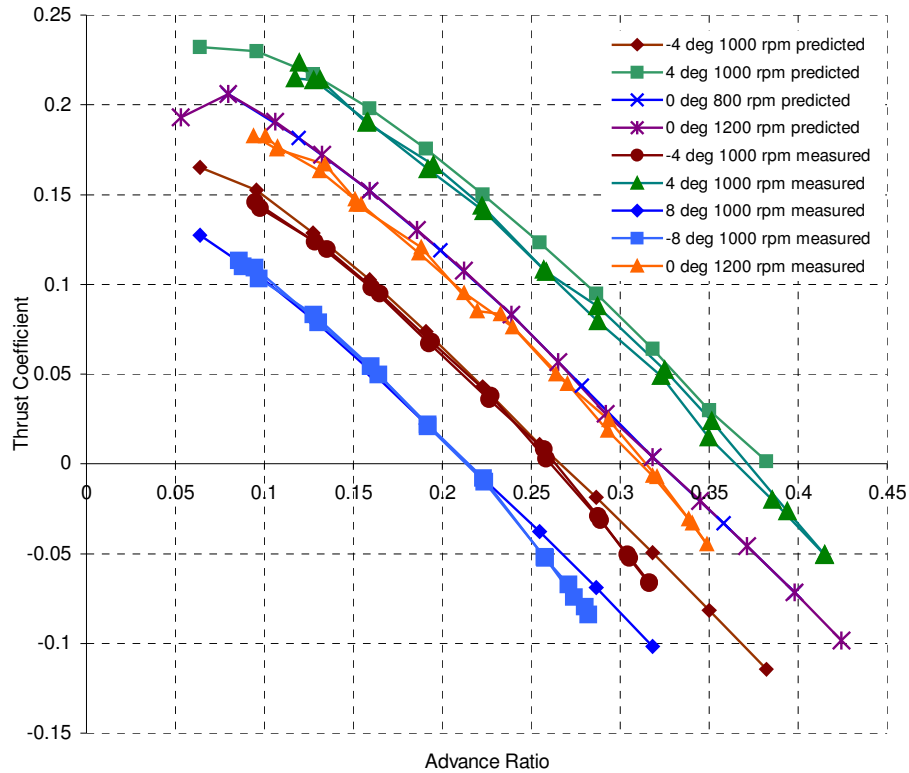


Figure 7.13 Comparisons between results of predicted and measured thrust coefficients at pitch angles from  $-8$  degrees to  $4$  degrees

### 7.9.2 Power Coefficient

At low power coefficient values there is a good correlation between the measured and the predicted power coefficient curves, see Figure 7.14. With decreasing advance ratios, the measured power coefficient curves are typically higher than those predicted for all pitch angles. The measured propeller performance data indicates that more power is being absorbed at a given advance ratio than that predicted, possibly through the aerodynamic losses associated with the increase in air velocity induced by the propeller through the wind tunnel.

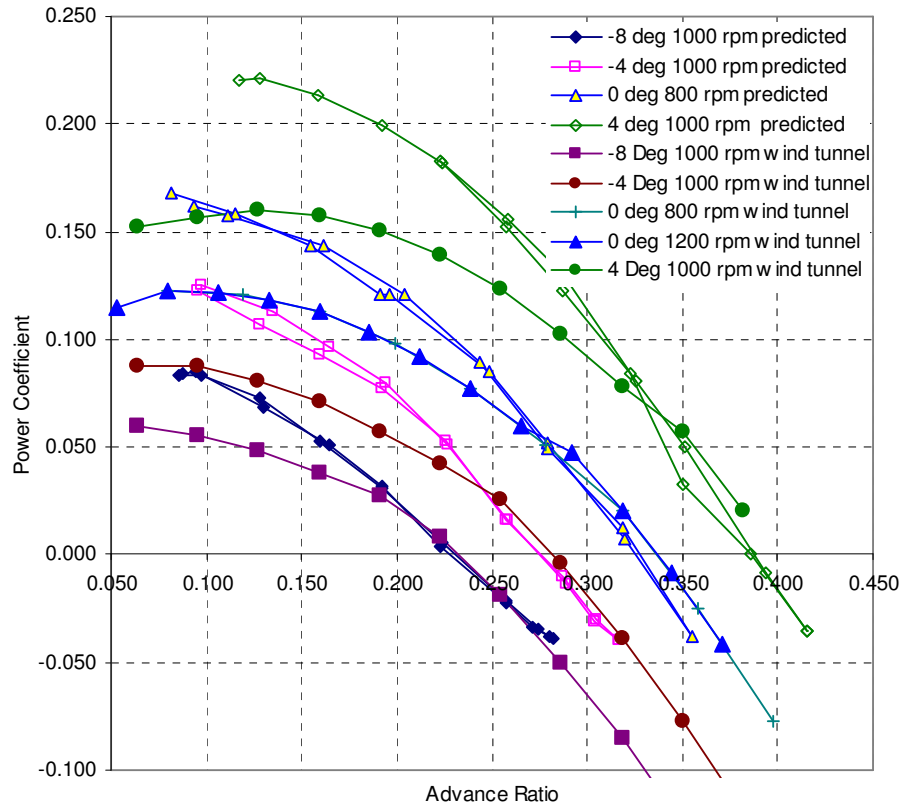


Figure 7.14 Comparisons between results of predicted and measured power coefficients at pitch angles from -8 degrees to 4 degrees

The measured propeller efficiency is proportional to the ratio of thrust coefficient to power coefficient for a given advance ratio. These values would be a great deal lower than predicted due to the high power coefficient data. These comparisons are not presented here due to the uncertainty in the advance ratio data and the higher than predicted power coefficients.

## 8. DESIGN METHODOLOGY ASSESSMENT

This study investigates the applicability of a simple propeller design method for use on a high altitude aircraft. The aircraft described in this work was the subject of a study into a high altitude platform completed some years previously.

Limited project funding was available for the manufacture of the research equipment and the experimental portion of this work was carried out on a propeller test rig designed for the testing of propellers capable of absorbing much greater power than the test propeller designed here. As such the load limits of the torque transducer were an order of magnitude larger than what would have been preferred. The accuracy of the torque results obtained through relating the voltage and current measured during tests to a calibration of the electric motor's torque characteristics is less than what would have been preferred.

The propeller was able to induce a relatively large velocity into the relatively small diameter wind tunnel test section, effectively ruling out low advance ratio testing and noticeably affecting the resultant power coefficient measurements. It was not possible at the time to measure the actual flow field during the propeller tests to obtain a quantitative assessment of the influence. The CSIR 7m wind tunnel would have been better suited to the testing of the model propeller due to the larger test section cross section and hence smaller influence on the flow field but financial resources were insufficient to allow consideration of that option.

The test propeller geometry was not measured and compared with the geometry as designed to confirm the accuracy of its manufacture. The CNC machining methodology and other manufacturing techniques should have ensured a reasonably accurate geometry. Although smooth to the touch, the propeller blade surface roughness was not measured.

The aerofoil analysis work was limited to XFOIL code due to its availability to the author. No two-dimensional aerofoil tests were performed to verify the XFOIL results, nor was a sensitivity analysis carried out on the default value of 9 chosen for the transition factor  $n_{crit}$ . According to Drela (1989) this value is typical for an "average wind tunnel". XFOIL is capable of accurately predicting high angle of attack behaviour provided there are "limited separation regions" (Drela, 1989). As the extent of the separation bubbles increases or if

the aerofoil stalls, the accuracy of the performance predictions and hence the propeller performance predictions would become questionable.

No Mach effects could be modelled in the wind tunnel.

Despite the limitations mentioned above, the minimum induced loss design methodology of Larrabee (1979a) was capable of producing a feasible propeller design for the chosen HALE UAV application. The method produced a propeller capable of flying the mission and the analysis method used to predict the performance at operational points far removed from the design point was able to produce acceptable results at the lower thrust coefficients (lower disc loadings) and lower advance ratios experienced during the climb phase, see Figure 7.13. It was difficult to assess the ability of the method to predict the required power coefficients due to the influence of the wind tunnel on the measured results.

The differences between the predicted values and those obtained from the wind tunnel tests are due to a number of reasons. The additional power absorbed by the wind tunnel losses, the influence of the incoming flow field on the propeller and the wind tunnel pitot-static system and the possibility even that of higher than predicted aerofoil section drag all added to these differences.

At the lower advance ratios and high power settings experienced during the climb phase the radial loading is quite dissimilar to that predicted for the propeller at the design point, see Figure 5.3. The blade loading near the root is typically far above the 1.3 assumed for the root at the design point and the tip aerofoil operates at lift coefficients ranging from slightly negative to more than double that of the design point value. This is due to the propeller pitch angle being varied through very large angles during this phase of flight, see Figure 5.4. This reduces the applicability of the radially graded momentum theory analysis and would explain the dissimilarities.

## 9. CONCLUSIONS AND RECOMMENDATIONS

The selection, design, construction and testing of a minimum induced loss propeller based on the method of Larrabee (1979a) was carried out. A mission simulation code was used to predict a number of similar propeller designs for the mission, one of which was selected based on its overall mission performance. A scale model of this propeller was tested in the CSIR 2 Metre Wind Tunnel.

The useful application of Larrabee's minimum induced loss method to the design of a propeller for a HALE UAV has been proven. A number of propellers designed by the method were capable of meeting the required performance specifications despite the wide range of operating conditions. The propeller design that produced the longest predicted range was selected for testing.

The radially graded momentum theory of Larabee (1984a) was able to reasonably accurately predict thrust coefficients for the propeller over the required wide range of propeller pitch angles, thrust settings and advance ratios in the UAV mission simulation.

Once corrected for the wider chord of the wind tunnel test propeller geometry, the predicted thrust coefficient values closely matched those from the wind tunnel tests at all tested pitch angles although there is a small offset from the predicted thrust coefficient data that increases with blade pitch angle, see Figure 7.13. This may be due to differences in the advance ratio used in the predicted propeller performance and that measured in the tunnel due to the induced flow field.

The predicted power coefficient values are likewise close to the measured values for the lower power coefficient ranges typically slightly over-predicting at values around zero. They are however not as accurately predicted at the higher coefficients with the error between the predicted and measured values increasing as the blade pitch angles increase as the propeller operates further from its design point.

The difference between the predicted and measured propeller power coefficients may be due to a number of effects:

- The additional power required of the propeller to overcome the losses incurred by the higher velocity induced in the wind tunnel.

- The velocity flow field induced by the propeller in the wind tunnel test section being somewhat different from that assumed by the theory due to the ducting effect of the tunnel inlet.
- The limitations of the assumption of an optimally graded radial loading in the analysis code when applied to a propeller operation far from the design point.
- Unlike the thrust coefficient which is largely affected by the blade section lift coefficient with a negligible effect from drag, errors in the prediction of the blade section drag has a relatively large effect on the power coefficient through the propeller torque. The predicted drag for the propeller aerofoils may be affected by the tunnel turbulence levels, blade skin smoothness, aerofoil accuracy etc.

It is recommended that further research be done into the comparison between the flow field of a static propeller in isolation and that of the flow field induced through the wind tunnel inlet in order to obtain a quantitative assessment of the size of the effect. Further work could also be carried out on determining the errors induced through utilising a radially graded blade loading based on the design case when determining the loading of a propeller operating far from its design point. Finally the effect of the wind tunnel on the performance of the propeller should be investigated.

## REFERENCES

1. Abbott, Ira H.; and Von Doenhoff, Albert E., 1959. *Theory of Wing Sections*. Dover Publishers, Inc.
2. Adkins, C. N., and Liebeck, R. H., 1983. *Design of optimum Propellers*, AIAA Paper 83-90.
3. Althaus, Dieter; and Wortmann, Franz Xaver., 1981. *Stuttgarter Profilkatalog I. (Stuttgart Profile Katalog I.)*, Friedr. Vieweg & Sohn (Braunschweig).
4. Amatt, W., 1973. *Summary of propeller Design Procedures and Data, Volume II Structural analysis and blade design*. Henry V. Borst & associates, Distributed by NTIS.
5. Ash, R.L., Miley, S.J., Landman, D and Hyde, K,W., 2001. *Evolution of Wright Flyer Propellers between 1903 and 1912*. AIAA Paper 2001-0309.
6. Barber, D., 1983. *Large Scale Propeller Testing in the NRC 9 Metre Wind Tunnel in Canada*, SAE Technical Paper 830751.
7. Barber, D.J., 1984. *Performance Evaluation Of Full Scale Propellers By Wind Tunnel Test*. AGARD CONFERENCE PROCEEDINGS No.366, Aerodynamics And Acoustics Of Propellers.
8. Bass, R.M, Munniksmas B. and van Hengst J., 1985. *Aerodynamic And Structural Aspects Of Propeller And Drive For A 1/5 Scale Model Wind Tunnel Programme*. AGARD, Aerodynamics and Acoustics of Propellers.
9. Bass, R. M., 1986. *Small Scale Wind Tunnel Testing of Model Propellers*. AIAA-86-0392, Presented at the AIAA 24th Aerospace Sciences Meeting, Reno, Nevada.
10. Bektas, C. Guler and M.A. Basturk, 2002. *Principal mechanical properties of Eastern Beech wood (Fagus orientalis Lipsky) naturally grown in Andirin Northeastern Mediterranean region of Turkey*. Turkish Journal of Agriculture and Forestry 26.
11. Betz, A., 1919. *"Schraubenpropeller mit geringstem Energieverlust"*. University of Göttingen Aerodynamic Laboratory.
12. Betz, A., 1922. *The Theory of the Screw Propeller*, NACA Technical Note 83, (Reprint from 'Die Naturwissenschaften' 1921, No 18).
13. Bieryla, D., Penn State Engineering, Center for Engineering Design and Entrepreneurship, Available at:  
<http://www.ecsel.psu.edu/~dbieryla/pathfinder/pathpropellers.html>

[Accessed 11 Feb 2007]

14. Borst, H. V., 1973. *Summary of propeller Design Procedures and Data, Volume I - Aerodynamic Design and Installation*. Henry V. Borst & associates, Distributed by NTIS.
15. Carroll, T. J. and Carroll, T R., 2005. *Wright Brothers' Invention of 1903 Propeller and Genesis of Modern Propeller Theory*, Journal of Aircraft, Vol. 42, No.1.
16. Carmichael, Ralph, 2006. *Public Domain Aeronautical Software*, <http://www.pdas.com>  
[Accessed on 11 August 2006]
17. Clutton, E., 1993. *Propeller making for the amateur*. Published by E. Clutton; Revised edition.
18. COESA, 1976. *U.S. Standard Atmosphere*, published by the U.S. Government Printing Office, Washington, D.C.
19. Colozza, A., 1998. *High Altitude Propeller Design and Analysis Overview*, Federal Data Systems, Cleveland Ohio.
20. Drela, M. and Giles, M.B., 1987. *ISES: A two-dimensional viscous aerodynamic design and analysis code*. AIAA Paper 87-0424.
21. Drela, M., 1989. *XFOIL: An Analysis and Design System for Low Reynolds Number Airfoils*. Low Reynolds Number Aerodynamics: Proceedings of the Conference, Notre Dame, Indiana, June 5-7. Springer-Verlag, New York.
22. Dryden Flight Research Centre – Fact Sheets Edited by Marty Curry.  
Available at: <http://www.nasa.gov/centers/dryden/news/FactSheets/FS-020-DFRC.html>  
[Accessed on 9 March 2008]
23. Eppler, R. and Hepperle, M., 1984. *A Procedure for Propeller Design by Inverse Methods*, International Conference on Inverse design Concepts in Engineering Sciences, pp. 445-460, Austin TX, October 17-18.
24. Eppler, Richard, 1990. *Airfoil Design and Data*. Springer-Verlag (Berlin).
25. Eppler, Richard, 1998. *Airfoil Program System "PROFIL98" User's Guide*. Richard Eppler.
26. Eppler, Richard; and Somers, Dan M., 1980. *A Computer Program for the Design and Analysis of Low-Speed Airfoils*. NASA TM-80210.
27. Federal Aviation Regulations Part 23.69, 1996. *Enroute climb / descent*, Doc. No. 27807, 61 FR 5187,

Accessed at <http://ecfr.gpoaccess.gov/cgi/t/text/text-idx?c=ecfr&sid=1741cfe6498c886bfdbec10978fc4e5c&rgn=div5&view=text&node=14:1.0.1.3.10&idno=14#14:1.0.1.3.10.2.60.19>

[Accessed on 9 March 2006]

28. Glauert, H., 1926. *The Analysis of Experimental Results in the Windmill Brake and Vortex Ring States of an Airscrew*. Report. 1026. Aeronautical Research Committee Reports and Memoranda, London.

29. Glauert H., 1943. *Airplane Propellers, Vol. 4*, Div. L in *Aerodynamic Theory*, edited by Durand W.F., Dover ed.

30. Glauert H., 1959. *The Elements of Airfoil and Airscrew Theory*. Cambridge University Press, Second Edition, reissued in 1983

31. Goebel G., 2008. *The NASA ERAST HALE UAV Program - v1.4.1 / chapter 15 of 19 / greg goebel / public domain*

Available at: [http://www.vectorsite.net/twuav\\_15.html](http://www.vectorsite.net/twuav_15.html)

[Accessed 19 March 2008]

32. Goldstein, S., 1929. *On the Vortex Theory of Screw Propellers*. Proceedings of the Royal Society Series A Vol. 123, London.

33. Hepperle M, 2004. *Designing an Airfoil*.

Available at: <http://www.mh-aerotoools.de/airfoils/methods.htm>

[Accessed 2 May 2005]

34. Himmelskamp, H., 1947. *Profile Investigations on a Rotating Airscrew*. Ph.D Dissertation, Gottingen Univ. 1945, Reports and Translations No.832.

35. Kaufman, J. Gilbert, 2004. *Aluminum Alloy Database*. Electronic ISBN: 1-59124-671-7, Knovel

Accessed at <http://www.knovel.com/knovel2/Toc.jsp?BookID=844>

[Accessed on 9 March 2008]

36. Koch, L.Danielle. 'Design and Performance Calculations of a Propeller for Very High Altitude Flight', Lewis Research Center, Cleveland Ohio, NASA TM - 1998-206637, February 1998

37. Larrabee, E.E., 1979a. *Practical design of Minimum Induced Loss Propellers*, SAE Technical Paper 790585

38. Larrabee, E.E., 1979b. *Design of Propellers for Motorsoarers*, NASA CP-2085, Part 1.

39. Larrabee, E. Eugene and French, Susan E., 1983. *Minimum induced loss windmills and propellers*. Journal of Wind Engineering and Industrial Aerodynamics, 15 p317-327, Elsevier Science Publishers B.V., Amsterdam

40. Larrabee, E.E., 1984a. *Five Years Experience with Minimum Induced Loss Propellers - Part 1: Theory; Part 2 - Applications*, SAE Technical Paper 840026 & 840027

41. Larrabee, E.E., 1984b. *Propellers for Human-Powered Vehicles*, Human Power, Journal of the IHPVA, Vol3., No2., pp. 9-11

42. Lock, C.N.H.; Batemen, H.; Townsend, H.C.H., 1926 *An Extension of the Vortex Theory of Airscrews with Applications to Airscrews of Small Pitch, Including Experimental Results. No. 1014*. Aeronautical Research Committee Reports and Memoranda, London, 1926

43. Monk, J. S., 1995. *Initial Design of a HALE UAV*, Internal Technical report, CSIR.

44. MT-Propeller, 2006.

Available at: <http://www.mt-propeller.com/imgs/photos/pages/strato.jpg>

[Accessed December 2008]

45. NASA Dryden Flight Research Center Photo Collection, <http://www1.dfrc.nasa.gov/Gallery/Photo/Helios/Medium/EC99-45140-11.jpg>

[Accessed 2003]

46. NASA Dryden Flight Research Center Photo Collection, NASA Photo EC95-43207-8, 1995, *Pathfinder – closeup of flight preparation on lakebed at sunrise*, <http://www.dfrc.nasa.gov/gallery/Photo/Pathfinder/Small/EC95-43207-8.jpg>, [Accessed 2003]

47. NASA Dryden Flight Research Center, NASA Photo EC98-44776-52, Oct 1998, <http://www.dfrc.nasa.gov/Gallery/photo/Centurion/Small/EC98-44776-52.jpg> [Accessed 2003]

48. NASA Dryden Flight Research Center Photo Collection, NASA Photo EC99-45152-6, Sept 1999,

Available at <http://www.dfrc.nasa.gov/Gallery/Photo/Perseus/Small/EC99-45152-6.jpg>

[Accessed 2003]

49. Prandtl, L. and Betz, A., *Schraubenpropeller mit geringstem Energieverlust*, (*Screw Propellers with Minimum Energy Loss*), Reports of the Kaiser Wilhelm Institute for Flow Research, 1919.

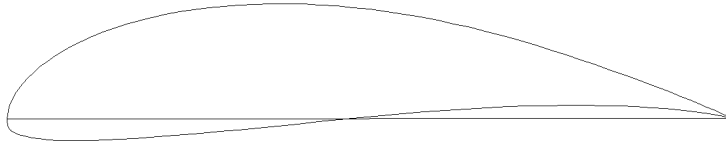
50. Rae, W. Jnr. & Pope, A., *Low-Speed Wind Tunnel Testing*, Wiley and Sons, 1984.
51. Riegels, F. W. *Aerofoil Sections*, Butterworth, London, 1961.
52. Roncz, J., *Propeller Development for the Rutan Voyager*, SAE Technical Paper 891034, 1989.
53. Rotax Aircraft, 2009. *Rotax 914 UL DCDI, engine performance, torque and fuel consumption brochure*, <http://www.rotax-aircraft-engines.com/downloadarea/914/914UL/performance/perf914UL.PDF>, Accessed on Jan 2009
54. Sand, E., 1973. *Summary of propeller Design Procedures and Data, Volume 3 - Hub, actuator, and control design*. Henry V. Borst & associates, Distributed by NTIS.
55. Schawe, D., Rohardt, C. and Wichmann, G., 2002. *Aerodynamic design assessment of Strato 2C and its potential for unmanned high altitude airborne platforms*, *Aerospace Science and Technology* 6, pp 43-51.
56. Schlichting, Hermann, 1955. *Boundary Layer Theory*. (J. Kestin, transl.): McGraw-Hill Book Co., Inc.
57. Selig, M.S., Donovan, J.F., Fraser, D.B., 1989. *Airfoils at low Speeds*, Soartech 8.
58. Selig, M. et al, 1997. *Camberline No. 5, Newsletter of the UIUC Low Speed Airfoil Test Program*.  
Available at: [http://www.ae.uiuc.edu/m-selig/uiuc\\_Isat/Isat\\_5bulletin.html](http://www.ae.uiuc.edu/m-selig/uiuc_Isat/Isat_5bulletin.html)  
[Accessed 2003]
59. Struthers, G., 2003. *Structural Calculations to Check a Prop Shaft Design*. Report CSIR-03001.
60. Welch, William A., 1979. *Lightplane Propeller Design, Selection, Maintenance & Repair*, Tab Books, First Edition
61. Zimmer H., Hoffmann R. and Horstmann K.H., *Investigations Of Modern General Aviation Propellers*

## **APPENDIX A AEROFOIL DATA**

The aerofoil geometries and aerodynamic characteristics as predicted by the XFOIL analyses are presented below. The lift and drag coefficients results are presented for the Reynolds numbers of 100 000, 250 000, 500 000 and 1 Million.

The “Notes” on the recommended aerofoil positions and “Characteristics” of the aerofoil in terms of maximum thickness and camber percentages are included as presented by Hepperle (2004) as well as his comments on the use of each aerofoil.

## MH 112



**Notes:** Designed for the inboard region of propellers, followed by section MH 113

Characteristics:

- Thickness: 16.2%
- Max. camber: 7.2%
- Can be used at Reynolds numbers of 300'000 and above.

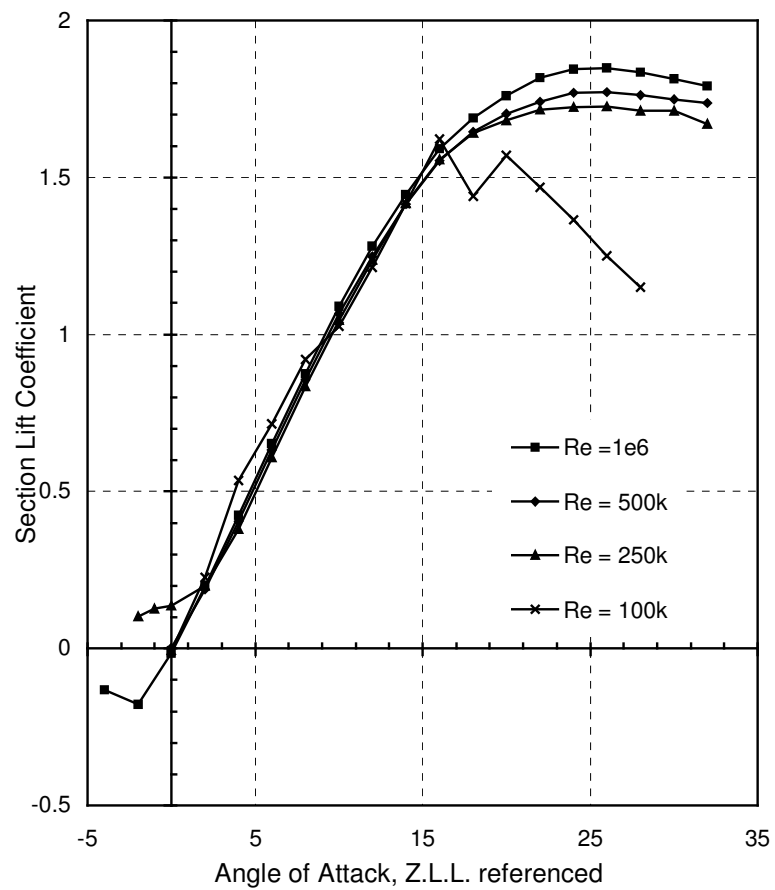


Figure A1 MH 112 lift coefficient versus angle of attack

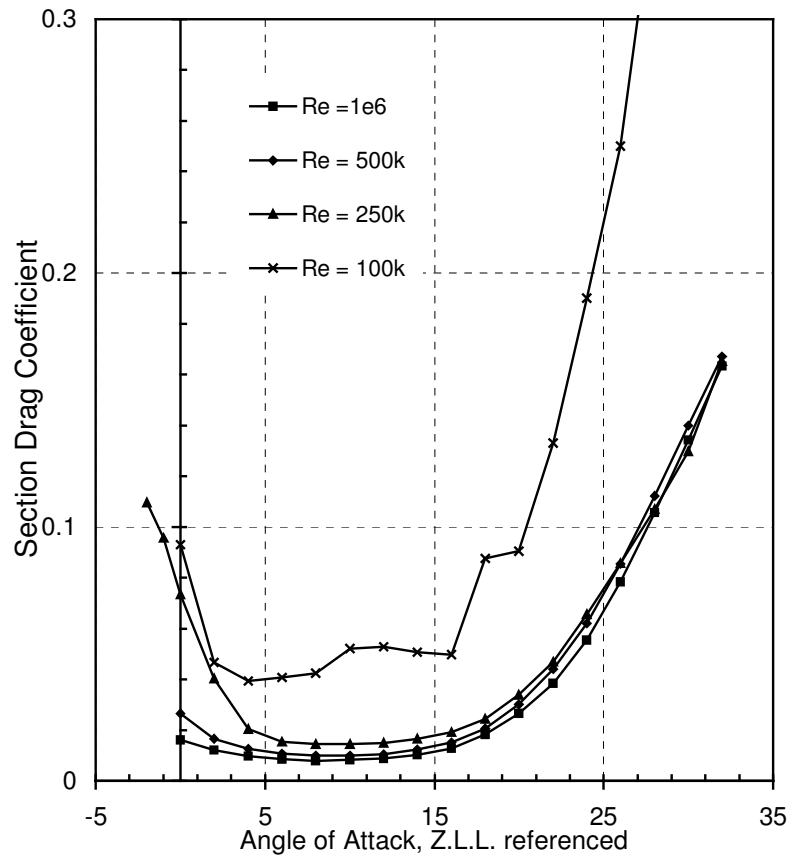
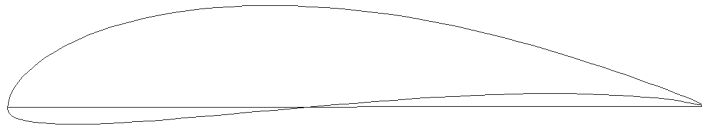


Figure A2 MH 112 drag coefficient versus angle of attack

## MH113



Notes: Designed for the inboard region of propellers, between MH 112 and MH 114

### Characteristics

- Thickness: 14.6%
- Max. camber: 6.9%
- Can be used at Reynolds numbers of 300'000 and above.

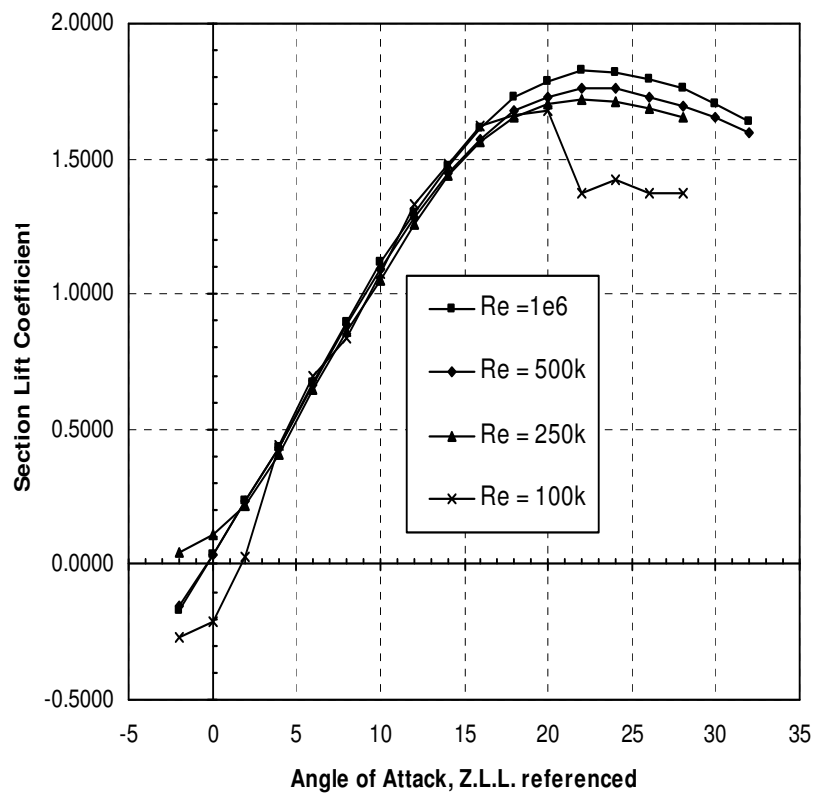


Figure A3 MH 113 lift coefficient versus angle of attack

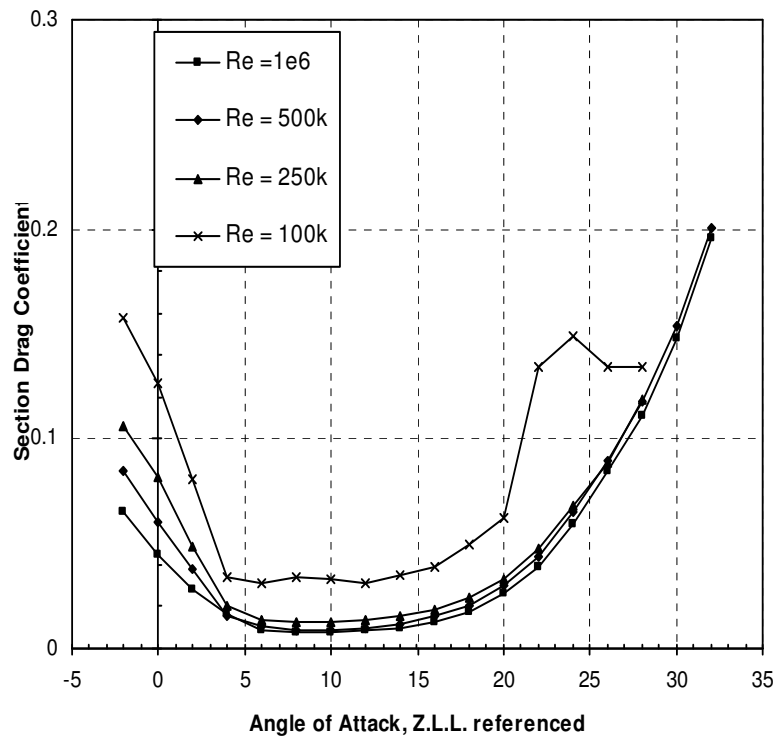


Figure A4 MH 113 drag coefficient versus angle of attack

## MH 114



Notes: Designed for the centre region of propellers, between MH 113 and MH 115

### Characteristics

- Thickness: 13.0%
- Max. camber: 6.5%
- Can be used at Reynolds numbers of 250'000 and above.

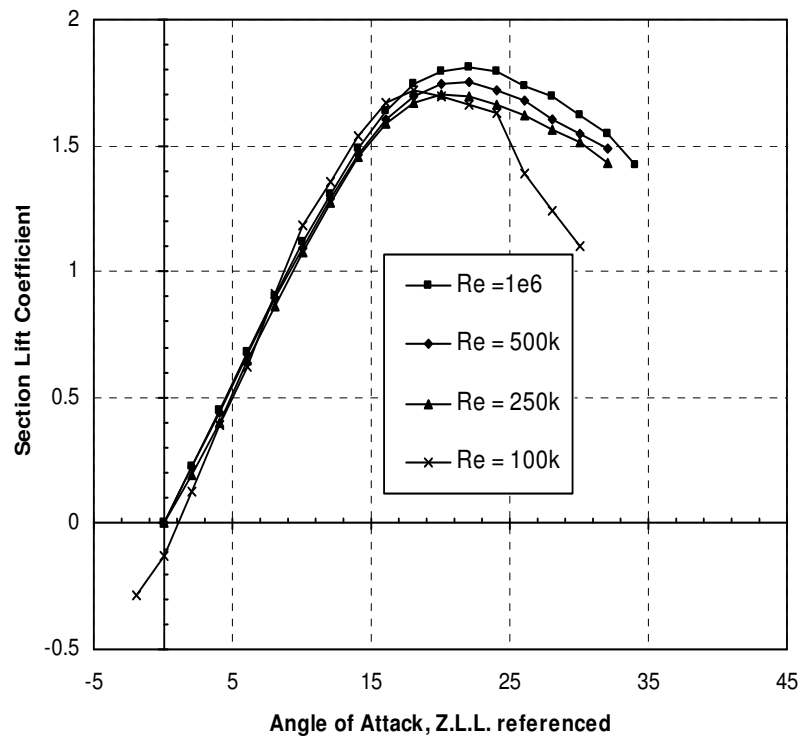


Figure A5 MH 114 lift coefficient versus angle of attack

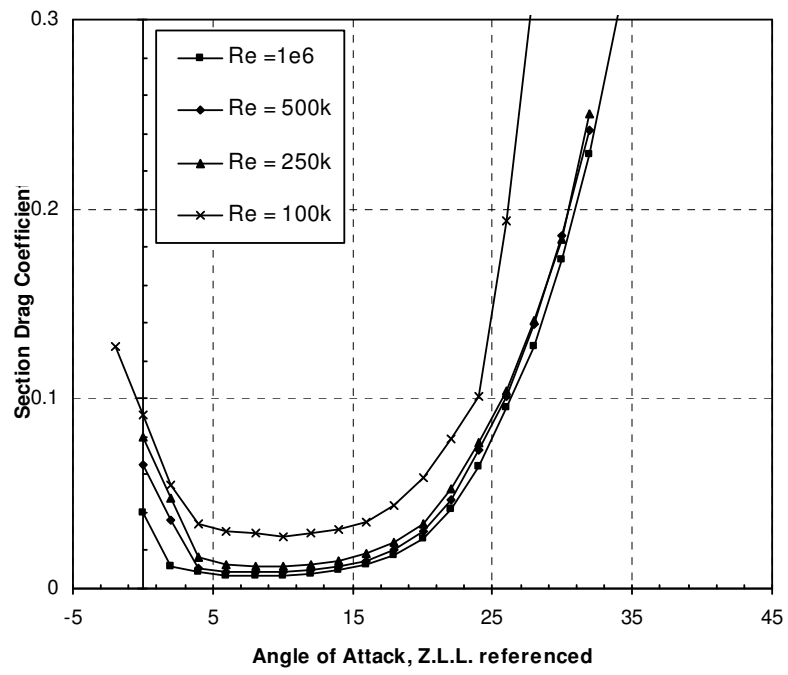


Figure A6 MH 114 drag coefficient versus angle of attack

## MH 115



**Notes:** Designed for the centre region of propellers, between MH 114 and MH 116

### Characteristics

- Thickness: 11.0%
- Max. camber: 5.5%
- Can be used at Reynolds numbers of 200'000 and above.

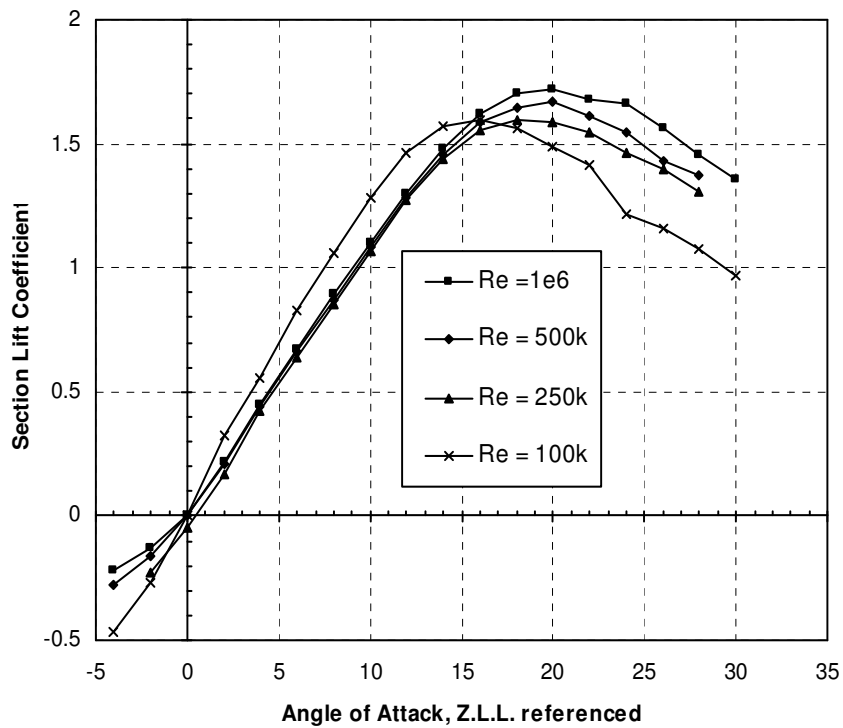


Figure A7 MH 115 lift coefficient versus angle of attack

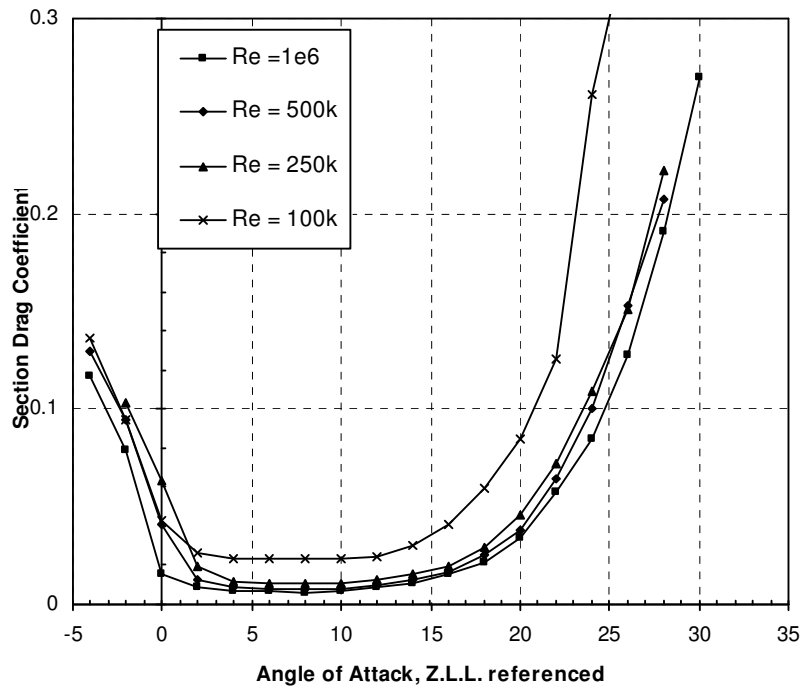
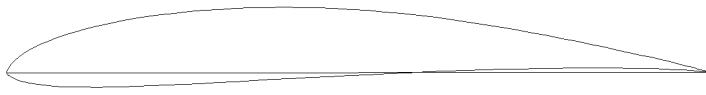


Figure A8 MH 115 drag coefficient versus angle of attack

## MH 116



**Notes:** Designed for the outboard region of propellers, between MH 115 and MH 117

### Characteristics

- Thickness: 9.8%
- Max. camber: 4.0%
- Can be used at Reynolds numbers of 200'000 and above.
- Design Mach number: 0.5 and below.

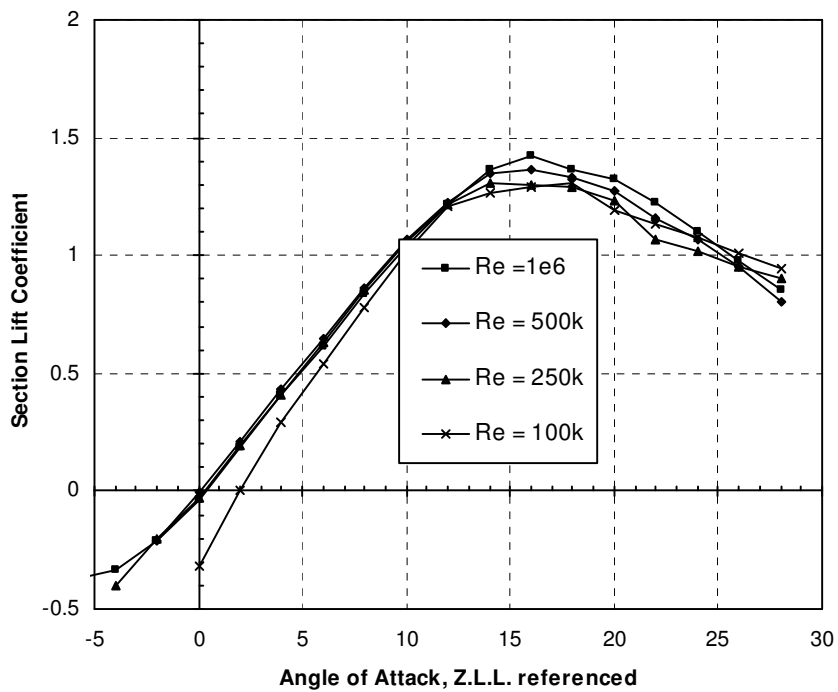


Figure A9 MH 116 lift coefficient versus angle of attack

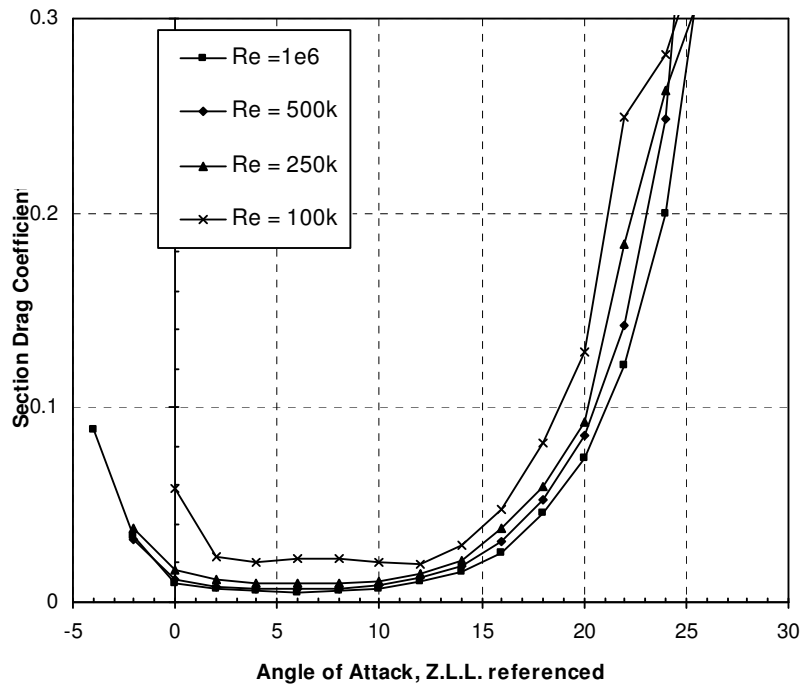
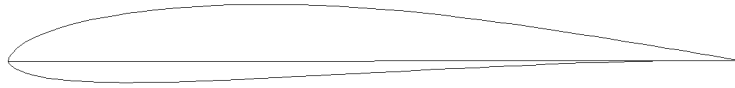


Figure A10 MH 116 drag coefficient versus angle of attack

## MH 117



**Notes:** *Designed for the tip region of propellers, outboard of MH 116*

### Characteristics

- Thickness: 9.8%
- Max. camber: 2.7%
- Can be used at Reynolds numbers of 100'000 and above.
- The Mach number should lower than 0.5.

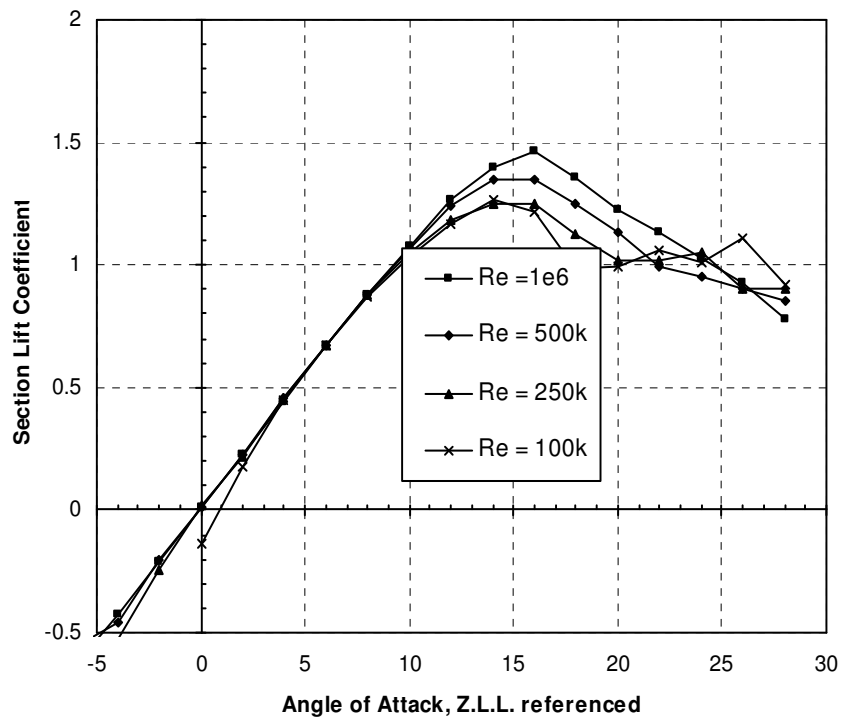


Figure A11 MH 117 lift coefficient versus angle of attack

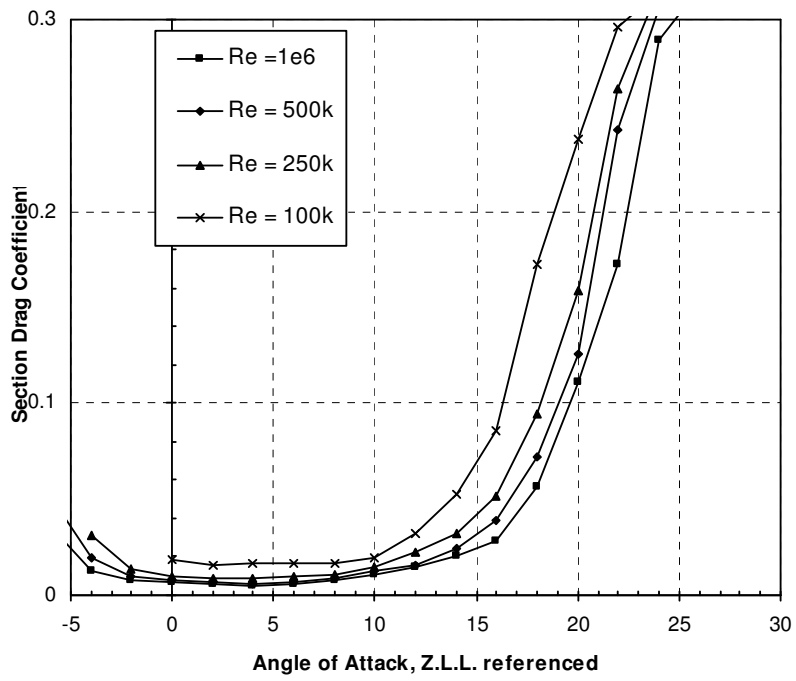


Figure A12 MH 117 drag coefficient versus angle of attack

## MH 121



**Notes:** Designed for the high speed tip region of propellers

### Characteristics

- Thickness: 8.8%
- Max. camber: 3.0%
- Can be used at Reynolds numbers of 100'000 and above.
- The Mach number should lower than 0.8.

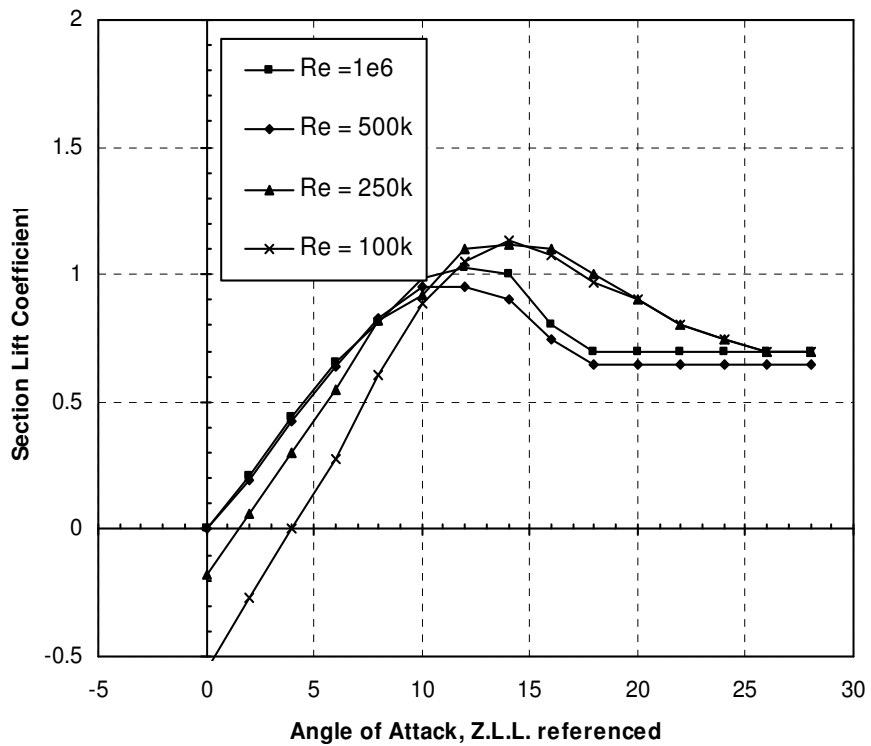


Figure A13 MH 121 lift coefficient versus angle of attack

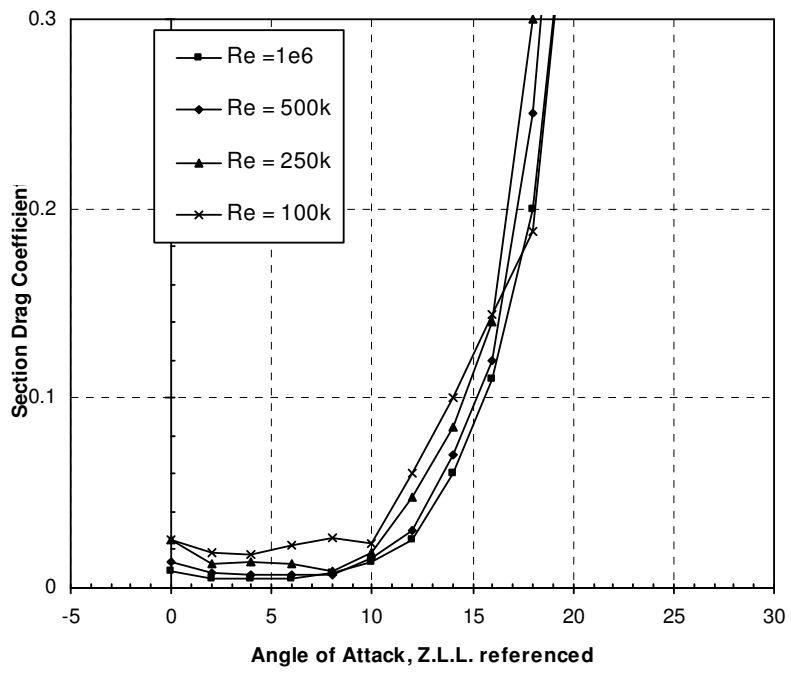


Figure A14 MH 121 drag coefficient versus angle of attack

## APPENDIX B TARE CORRECTIONS

### First Test Series

The drag on the test rig was determined at various tunnel speeds with the propeller removed and the hub end holes covered to minimise any transverse flow. During the first test series the oscillatory action of the drive belts at the higher tunnel speeds caused relatively large variations in the drag force data which increases with increasing tunnel speed. Typically the variation in drag readings remained within 5% of the mean readings. This spread in the data is illustrated in Figure B1.

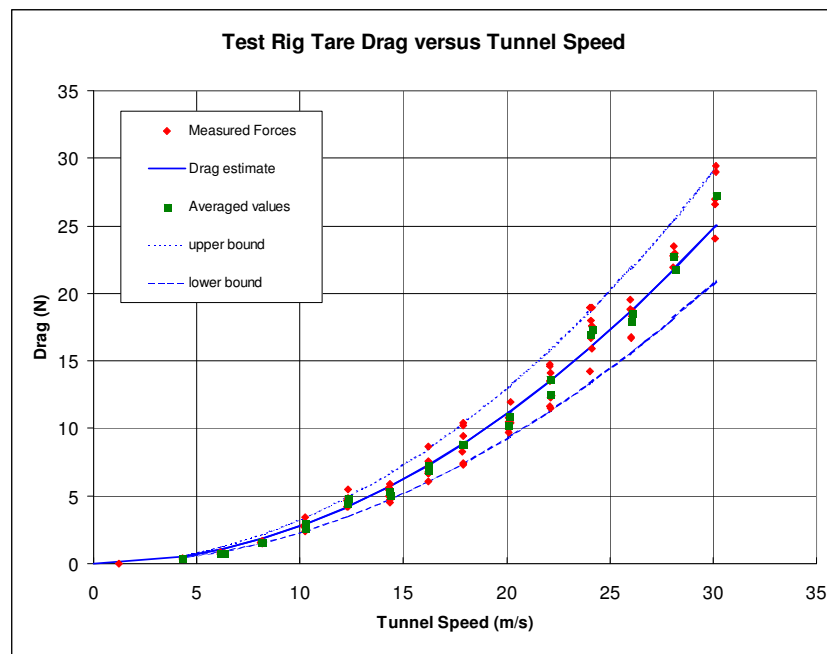


Figure B1 Measured test rig drag against tunnel speed

The range of tare drag coefficient values are plotted in Figure B2

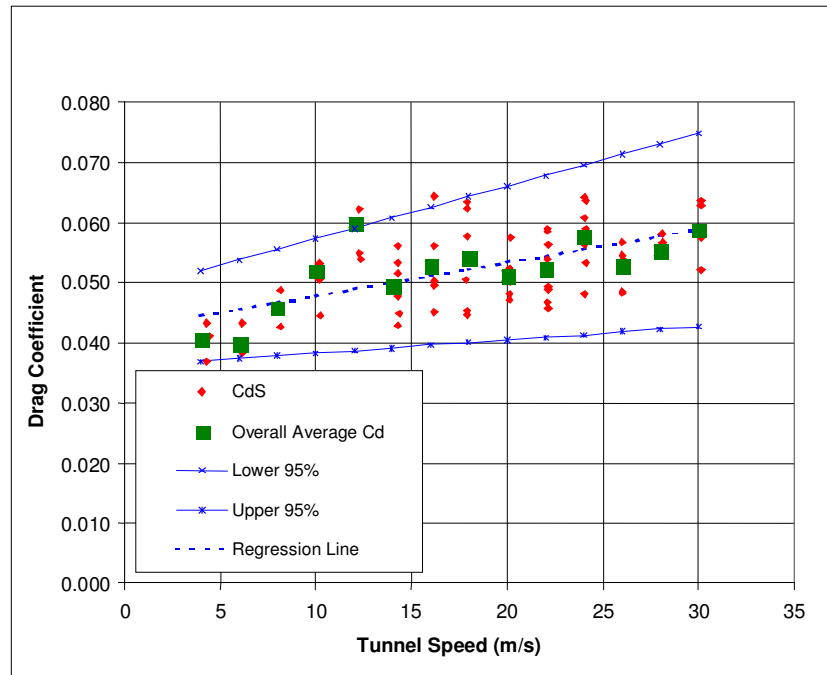


Figure B2 Influence of wind tunnel velocity on test rig drag coefficient

The curve produced by the regression line results in the Tare Correction Coefficient = - 0.042193 - 0.0005507\*Tunnel Velocity (m/s).

The upper and lower 95% lines are added to provide an indication of the relative magnitude of the scatter.

## Second Test Series

With the new fairing of the second test series enclosing the drive belts, the total drag is reduced and the oscillatory forces from the belts are removed offering less scatter in the results. See Figures B3 and B4.

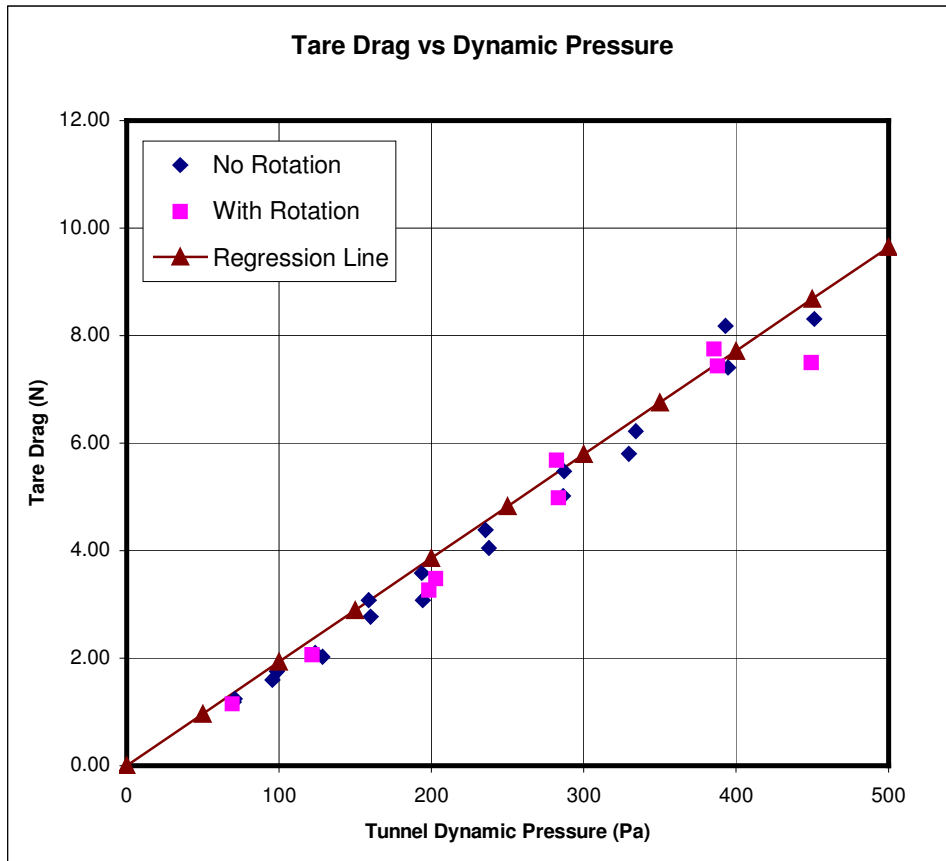


Figure B3 Increase in test rig tare drag with tunnel dynamic pressure

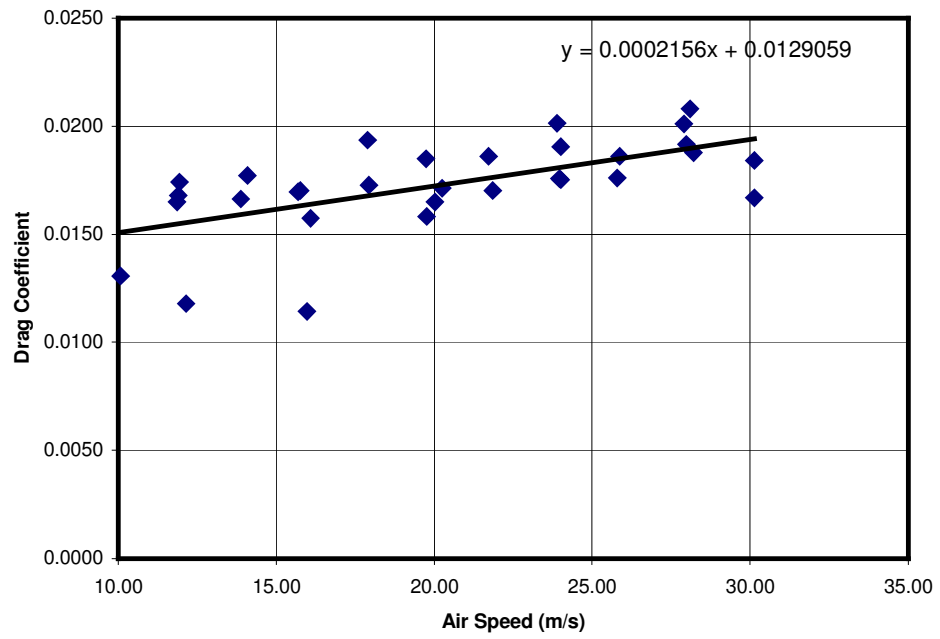


Figure B4 Variation of test rig drag coefficient with tunnel speed with the new fairing

## APPENDIX C THRUST LOAD CELL CALIBRATION

The voltmeter outputs for each of the five readings taken during the thrust load cell calibration are tabulated against the applied load, see Figure C1.

Table C1 Calibration of Thrust Load Cell at 10 Volts

Applied Mass	Equivalent Load	Reading 1	Reading 2	Reading 3	Reading 4	Reading 5
Kg	N	mV	mV	mV	mV	mV
0	0	6.6322	6.6040	6.6050	6.5890	6.5960
10	98.1	11.5190	11.5040	11.5090	11.5085	11.5058
20	196.2	16.2040	16.2150	16.2106	16.2151	16.2164
30	294.3	21.2558	21.2596	21.2600	21.2616	21.2624
40	392.4	26.2554	26.2759	26.2811	26.2832	26.2878
50	490.5	31.2792	31.3044	31.3116	31.3099	31.3088
60	588.6	36.3092	36.3291	36.3410	36.3452	36.3481
50	490.5	31.5838	31.5779	31.5744	31.5706	31.5708
40	392.4	26.5988	26.5941	26.5898	26.5862	26.5862
30	294.3	21.5230	21.5231	21.5178	21.5202	21.5254
20	196.2	16.4224	16.4209	16.4207	16.4213	16.4197
10	98.1	11.3220	11.3116	11.3141	11.3145	11.3145
0	0	6.5789	6.5750	6.5690	6.5788	6.5770

A linear regression applied to the calibration data provided a calibration curve of slope 0.0508 and with intercept 6.511. Plotting the differences in outputs between the calibration curve and the actual values from the various data curves illustrates the error between the curves for each set of readings. The maximum error above the measured data is 1.6 %, the maximum error below the measured data is -1.8%. See Figure C2

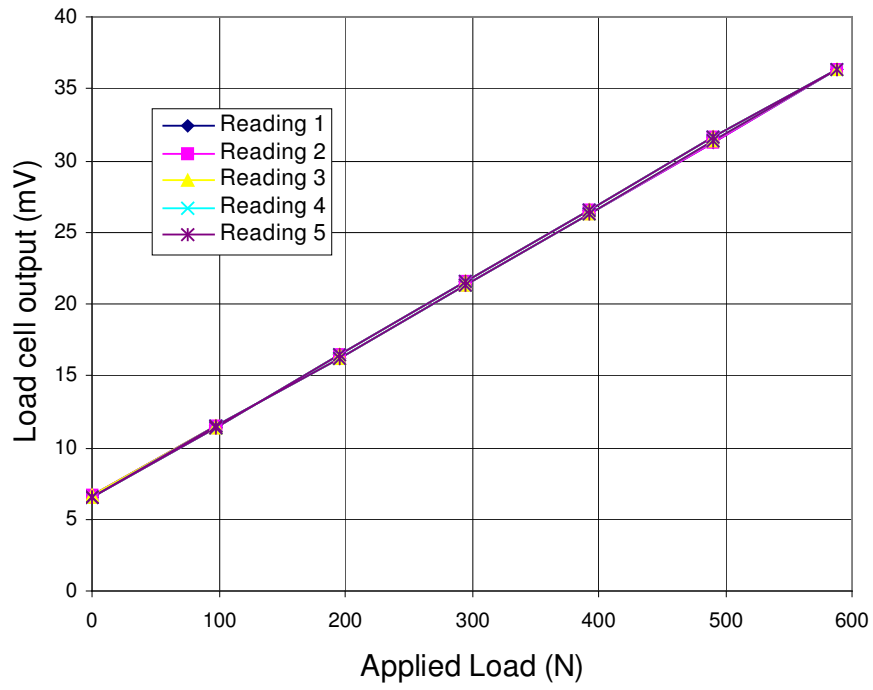


Figure C1 Thrust cell calibrations at 10 Volts

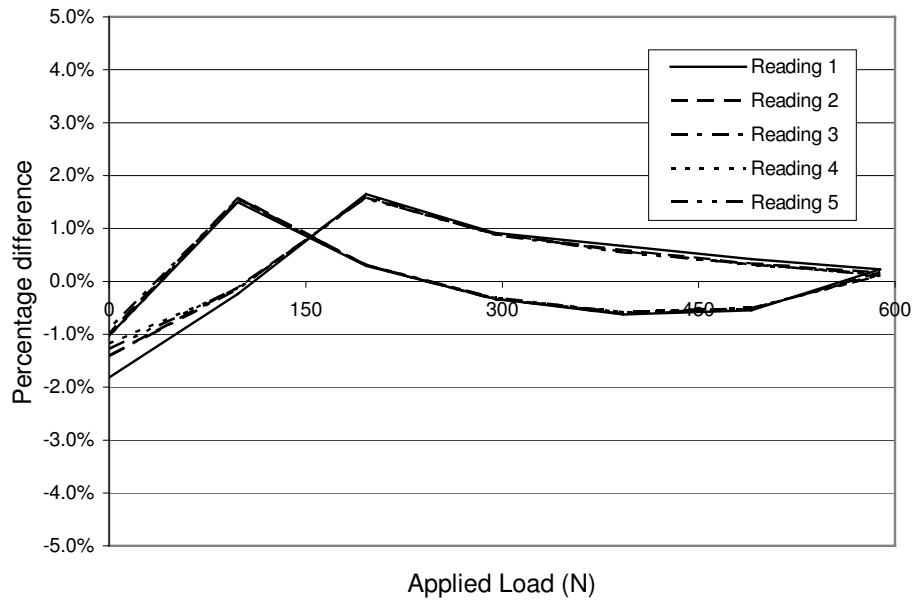


Figure C2 Thrust cell calibration differences at 10 Volts

Table C2 Determination of gradients and offsets

	Reading 1 mV/N	Reading 2 mV/N	Reading 3 mV/N	Reading 4 mV/N	Reading 5 mV/N
Offset	6.606	6.590	6.587	6.584	6.587
Gradient	0.05071	0.05077	0.05078	0.05078	0.05078

In the wind tunnel data post processing, the zero reading is subtracted from the remainder of the data obviating a need for an intercept. The gradient of **0.0508** was applied to all the wind tunnel raw thrust data to convert to actual thrust.

For the second wind tunnel test series, the load cell characteristics had already been incorporated into the data acquisition program for a commercial propeller test. Figure C3 and Table C3 illustrate the data used in that calibration.

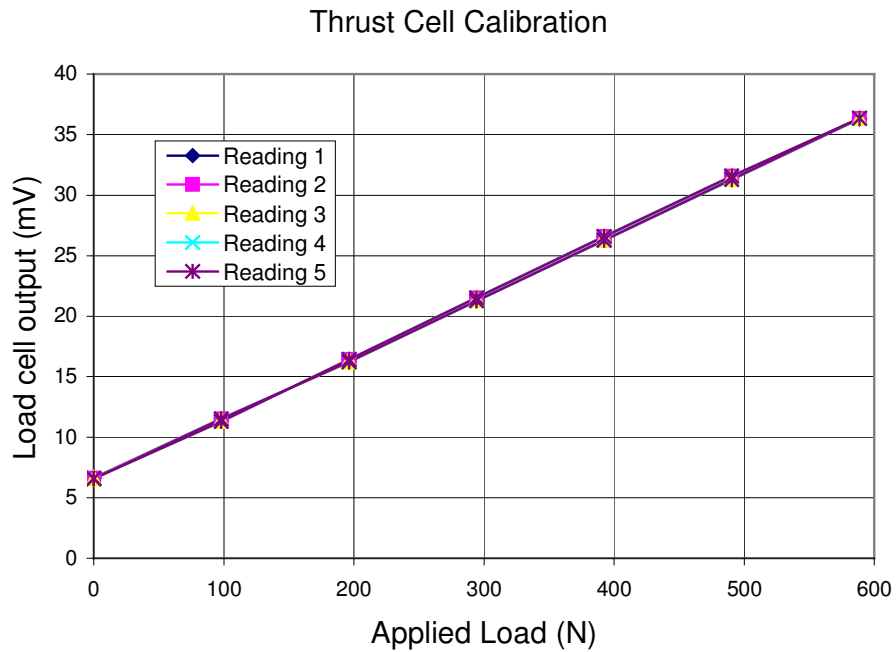


Figure C3 Second test series thrust cell calibration

Table C3 Calibration of thrust load cell at 12 Volts

Applied Mass Kg	Equivalent Load N	Reading mV
0	0	-4.3427
5	48.931	-6.3355
10	97.861	-8.3274
15	146.792	-10.3426
20	195.722	-12.3716
30	293.583	-16.3759

As before the zero reading is subtracted from the recorded data obviating a need for an intercept value. The gradient of **0.04102** was applied to the wind tunnel raw thrust data to convert to actual thrust in N.

## APPENDIX D WIND TUNNEL TEST DATA FIRST TEST SERIES

The wind tunnel test plan included testing the propeller blades at pitch angles of 0 degrees, 4 degrees and 8 degrees followed by - 4 degrees at the lower rotational speed. The two 2 degrees positive and negative angles were included later to add more data about the design point (zero pitch). These runs were then repeated at the 1200 RPM rotational speeds. Finally -8 degrees and -12 degrees pitch angles were tested as was the final 12 degrees pitch angle.

The torque readings were not available throughout the tests due to a faulty sensor. At one point during the tests (test 1039) it appeared that the torque readings were once again working but the availability of useful data was so low that the noise corrupted the data averages to the extent that no useful torque values were available.

Test No.	Angle	rpm	Comments
1032	-	-	Test file to confirm data recording
1034	-	-	Initial tare run
1035	0	800	Tare run with motor running at 800 rpm
1036	0	800	
1037	4	800	
1038	8	800	
1039	-4	800	
1040	-	-	Test file to confirm torque cell functionality
1041	-4	800	Test of a few points with torque readings
1042	-4	800	Full test with torque readings
1043	-	-	Check on calibration values
1044	0	800	200 readings averaged for torque
1045	2	800	
1046	2	1200	
1047	0	1200	
1048	4	1200	
1049	8	1200	
1050	-4	1200	
1051	-8	1200	
1052	-12	1200	
1053	12	800	
1054	-	800	Final Tare run

The results of the wind tunnel tests are presented below in the following order of increasing pitch angle. This is not the order in which the tests were carried out. The tests were carried out at different times of the day and night in thankfully, largely windless conditions.

Table D1 List of wind tunnel test points

Table No.	Pitch Angle	RPM
E 2	-12	1200
E 3	-8	1200
E 4	-4	800
E 5	-4	1200
E 6	0	800
E 7	0	1200
E 8	2	800
E 9	2	1200
E 10	4	800
E 11	4	1200
E 12	8	800
E 13	8	1200
E 14	12	800

Air density, in  $\text{kg/m}^3$ , was calculated in the data acquisition system from the ideal gas

equation  $\rho = \frac{P}{RT}$

where the values of  $P$ , the static pressure, and  $T$ , the ambient temperature, were recorded from the 2MWT static pressure transducer and temperature probe respectively.

Air velocity, in m/sec, was calculated from the equation  $V = \sqrt{\frac{2P}{\rho}}$

The advance ratio at each test point was calculated from the equation  $\lambda = \frac{V}{\pi ND}$

with the actual rotational speed,  $N$  ( $\Omega/\text{sec}$ ) and tunnel velocity  $V$  (m/s) used at each test point.

The thrust coefficient was determined from the equation  $T_c = \frac{T}{\rho N^2 D^4}$

Table D2 -12° Pitch Angle at 1200 RPM

Pitch Angle (deg)	Prop Speed (rpm)	Blade A (deg)	Blade B (deg)
-12	1200	-11.9	-12.0

Static Pressure (Pa)	Dynamic Pressure (Pa)	Temp. (K)	Measured Load (N)
86786.5	-1.7	297.3	99.6

Static Pressure (Pa)	Dynamic Pressure (Pa)	Temp. (K)	Corrected Load (N)	Air Density (kg/cu. m)	Tunnel Velocity (m/sec)	Induced Vel. Component (-)	Tare Drag (N)	Thrust (N)	Advance Ratio (-)	Thrust Coefficient (-)
86775.5	13.08	296.9	57.3	1.018	5.1	1.69	-4.7	62.0	0.067	0.0734
86776.8	12.78	296.8	58.5	1.018	5.0	1.71	-4.7	63.2	0.066	0.0748
86777.4	13.07	296.7	57.2	1.019	5.1	1.69	-4.7	61.9	0.067	0.0732
86771.5	20.25	296.6	48.3	1.019	6.3	1.30	-5.4	53.7	0.084	0.0635
86771.5	20.25	296.5	46.7	1.020	6.3	1.30	-5.4	52.1	0.084	0.0616
86757.2	34.26	296.5	30.1	1.019	8.2	0.95	-6.6	36.7	0.109	0.0434
86756.6	34.21	296.5	33.3	1.019	8.2	0.95	-6.6	39.9	0.109	0.0472
86737.4	52.80	296.4	12.2	1.019	10.2	0.72	-8.1	20.3	0.135	0.0241
86737.4	52.97	296.1	13.7	1.020	10.2	0.72	-8.2	21.8	0.135	0.0258
86717.8	72.41	296.1	-0.6	1.020	11.9	0.58	-9.5	8.9	0.158	0.0106
86717.8	72.26	296.1	-3.5	1.020	11.9	0.59	-9.5	6.0	0.158	0.0071
86689.8	101.05	296.0	-26.6	1.020	14.1	0.45	-11.4	-15.2	0.187	-0.0179
86689.6	101.27	296.1	-25.6	1.020	14.1	0.45	-11.4	-14.1	0.187	-0.0167
86718.5	73.08	296.2	-1.2	1.020	12.0	0.58	-9.6	8.4	0.159	0.0099
86718.7	73.06	296.3	-2.1	1.020	12.0	0.58	-9.6	7.5	0.159	0.0089
86738.1	53.73	296.2	16.9	1.020	10.3	0.72	-8.2	25.1	0.136	0.0297
86738.1	53.48	296.2	16.3	1.020	10.2	0.72	-8.2	24.5	0.136	0.0289
86759.4	34.23	296.2	33.1	1.020	8.2	0.95	-6.6	39.7	0.109	0.0470
86759.8	34.35	296.2	34.9	1.020	8.2	0.95	-6.6	41.5	0.109	0.0491
86775.3	20.49	296.1	48.5	1.021	6.3	1.30	-5.4	54.0	0.084	0.0637
86775.3	20.36	296.0	48.0	1.021	6.3	1.30	-5.4	53.4	0.084	0.0630
86782.9	13.32	296.0	57.4	1.021	5.1	1.67	-4.7	62.1	0.068	0.0733
86783.7	13.24	295.7	57.4	1.022	5.1	1.67	-4.7	62.1	0.068	0.0732

Table D3 – 8° Pitch Angle at 1200 RPM

Pitch Angle (deg)	Propeller speed (rpm)	Blade A (deg)	Blade B (deg)	Zero Values:	Static Pressure	Dynamic Pressure	Temp.	Pre load
					(Pa)	(Pa)	(K)	(N)
-8	1200	-8.0	-8.1		86759.1	-1.78	299.1	99.6

Static Pressure	Dynamic Pressure	Temperature	Corrected Load	Air Density	Tunnel Velocity	Induced Vel. Component	Tare Drag	Thrust	Advance Ratio	Thrust Coefficient
(Pa)	(Pa)	(K)	(N)	(kg/cu. m)	(m/sec)	(-)	(N)	(N)	(-)	(-)
86742.9	18.22	298.9	78.7	1.011	6.0	0.76	-2.71	81.4	0.080	0.0970
86744.2	18.58	299.1	77.0	1.010	6.1	0.76	-2.77	79.7	0.080	0.0951
86729.1	34.18	299.0	62.0	1.011	8.2	0.43	-3.39	65.4	0.109	0.0780
86730.5	34.19	299.1	58.2	1.010	8.2	0.43	-3.39	61.6	0.109	0.0736
86730.7	34.11	299.2	66.9	1.010	8.2	0.43	-3.38	70.3	0.109	0.0839
86732.0	33.85	299.0	58.9	1.010	8.2	0.43	-3.35	62.2	0.109	0.0743
86713.5	52.61	299.0	49.1	1.010	10.2	0.25	-4.06	53.1	0.135	0.0634
86713.9	52.57	298.8	42.5	1.011	10.2	0.25	-4.06	46.6	0.135	0.0555
86714.8	52.53	298.7	46.3	1.011	10.2	0.25	-4.05	50.4	0.135	0.0601
86694.1	74.62	298.5	23.0	1.012	12.1	0.14	-4.84	27.8	0.161	0.0332
86694.4	74.67	298.7	29.6	1.011	12.2	0.14	-4.84	34.4	0.161	0.0411
86695.0	74.28	298.8	30.8	1.011	12.1	0.14	-4.82	35.7	0.161	0.0425
86695.7	74.53	298.2	22.2	1.013	12.1	0.14	-4.83	27.0	0.161	0.0322
86671.7	100.59	298.8	9.4	1.011	14.1	0.06	-5.75	15.2	0.187	0.0181
86671.7	100.18	298.5	4.6	1.011	14.1	0.06	-5.72	10.3	0.187	0.0123
86672.2	100.33	298.6	9.7	1.011	14.1	0.06	-5.73	15.4	0.187	0.0184
86642.2	130.38	298.0	-13.4	1.013	16.0	0.01	-6.78	-6.6	0.213	-0.0079
86642.4	130.65	298.0	-15.2	1.013	16.1	0.01	-6.80	-8.4	0.213	-0.0100
86612.2	161.73	298.1	-33.9	1.012	17.9	-0.03	-7.84	-26.1	0.237	-0.0311
86611.9	161.62	298.4	-31.3	1.011	17.9	-0.03	-7.83	-23.5	0.237	-0.0280
86643.5	130.72	297.7	-13.7	1.014	16.1	0.01	-6.80	-6.9	0.213	-0.0082
86643.7	131.13	298.2	-12.9	1.012	16.1	0.01	-6.83	-6.1	0.213	-0.0072
86674.4	100.96	298.3	5.5	1.012	14.1	0.06	-5.77	11.2	0.187	0.0134
86675.6	100.85	298.1	12.0	1.013	14.1	0.06	-5.76	17.8	0.187	0.0212
86702.6	74.55	298.3	26.6	1.012	12.1	0.14	-4.83	31.5	0.161	0.0375
86703.5	74.54	297.9	30.1	1.014	12.1	0.14	-4.83	34.9	0.161	0.0415
86725.9	52.82	298.3	48.1	1.013	10.2	0.25	-4.08	52.2	0.135	0.0621
86726.3	52.76	297.7	48.7	1.015	10.2	0.25	-4.07	52.8	0.135	0.0627
86746.1	34.07	297.9	64.3	1.014	8.2	0.43	-3.37	67.6	0.109	0.0804
86746.3	34.00	297.4	60.7	1.016	8.2	0.43	-3.37	64.1	0.109	0.0761
86763.1	18.78	297.4	79.3	1.016	6.1	0.76	-2.80	82.1	0.081	0.0974
86763.3	18.80	297.5	79.1	1.016	6.1	0.76	-2.80	81.9	0.081	0.0971

Table D4 – 4° Pitch Angle at 800 RPM

Pitch Angle (deg)	Propeller speed (rpm)	Blade A (deg)	Blade B (deg)
-4	800	-4.0	-4.1

Zero Values:	Static Pressure (Pa)	Dynamic Pressure (Pa)	Temperature (K)	Pre load (N)
	87158.9	-0.79	295.4	99.4

Static Pressure (Pa)	Dynamic Pressure (Pa)	Temperature (K)	Corrected Load (N)	Air Density (kg/cu. m)	Tunnel Velocity (m/sec)	Induced Vel. Component (-)	Tare Drag (N)	Thrust (N)	Advance Ratio (-)	Thrust Coefficient (-)
87157.1	13.12	294.1	47.4	1.032	5.0	0.67	-1.72	49.1	0.100	0.1290
87157.1	9.98	294.1	48.1	1.032	4.4	0.82	-1.55	49.6	0.087	0.1304
87158.4	10.58	294.0	47.1	1.033	4.5	0.79	-1.58	48.7	0.090	0.1278
87150.4	19.07	294.1	39.7	1.032	6.1	0.47	-1.95	41.7	0.121	0.1095
87152.3	19.23	294.0	40.0	1.033	6.1	0.47	-1.96	42.0	0.121	0.1102
87138.8	32.62	293.9	29.0	1.033	7.9	0.26	-2.47	31.5	0.158	0.0826
87140.2	33.17	293.9	28.6	1.033	8.0	0.26	-2.50	31.1	0.159	0.0817
87125.2	50.13	293.8	16.5	1.033	9.9	0.13	-3.12	19.7	0.196	0.0516
87125.2	51.32	293.8	16.3	1.033	10.0	0.13	-3.16	19.4	0.198	0.0511
87103.4	75.62	293.7	1.3	1.033	12.1	0.04	-4.03	5.3	0.241	0.0140
87101.5	74.84	293.7	0.1	1.033	12.0	0.04	-4.01	4.1	0.239	0.0109
87077.5	100.92	293.6	-13.1	1.033	14.0	-0.01	-4.94	-8.2	0.278	-0.0215
87078.0	100.27	293.6	-13.5	1.033	13.9	-0.01	-4.91	-8.5	0.277	-0.0224
87048.0	131.11	293.6	-32.2	1.033	15.9	-0.05	-6.02	-26.2	0.317	-0.0687
87049.9	131.35	293.5	-31.8	1.033	15.9	-0.05	-6.03	-25.7	0.317	-0.0675
87052.3	132.63	293.5	-33.1	1.033	16.0	-0.05	-6.08	-27.0	0.319	-0.0708
87084.9	101.72	293.6	-12.8	1.033	14.0	-0.01	-4.97	-7.8	0.279	-0.0206
87084.5	100.75	293.6	-13.3	1.033	14.0	-0.01	-4.93	-8.4	0.278	-0.0219
87112.5	75.23	293.5	0.7	1.034	12.1	0.04	-4.02	4.7	0.240	0.0124
87115.6	75.10	293.5	0.3	1.034	12.1	0.04	-4.02	4.3	0.240	0.0112
87142.3	51.60	293.4	15.6	1.035	10.0	0.13	-3.17	18.8	0.199	0.0492
87143.8	51.74	293.5	15.6	1.034	10.0	0.13	-3.18	18.8	0.199	0.0493
87165.8	33.82	293.5	28.5	1.034	8.1	0.25	-2.52	31.0	0.161	0.0814
87164.9	34.39	293.5	28.0	1.034	8.2	0.24	-2.54	30.6	0.162	0.0802
87165.8	33.55	293.4	28.7	1.035	8.1	0.25	-2.51	31.3	0.160	0.0819
87180.0	20.06	293.4	39.2	1.035	6.2	0.45	-1.99	41.2	0.124	0.1081
87180.8	19.82	293.4	39.0	1.035	6.2	0.46	-1.98	40.9	0.123	0.1073
87191.3	11.15	293.4	48.2	1.035	4.6	0.76	-1.61	49.8	0.092	0.1306
87191.5	11.83	293.5	48.0	1.035	4.8	0.72	-1.64	49.6	0.095	0.1300

Table D5 – 4° Pitch Angle at 1200 RPM

Pitch Angle (deg)	Propeller speed (rpm)	Blade A (deg)	Blade B (deg)
-4	1200	-3.9	-4.1

Zero Values:	Static Pressure (Pa)	Dynamic Pressure (Pa)	Temperature (K)	Pre load (N)
	86731.3	-2.14	299.7	99.6

Static Pressure (Pa)	Dynamic Pressure (Pa)	Temperature (K)	Corrected Load (N)	Air Density (kg/cu. m)	Tunnel Velocity (m/sec)	Induced Vel. Component (-)	Tare Drag (N)	Thrust (N)	Advance Ratio (-)	Thrust Coefficient (-)
86704.3	24.80	300.2	106.5	1.006	7.0	0.75	-3.71	102.8	0.093	0.1232
86703.5	24.61	300.5	105.9	1.005	7.0	0.75	-1.13	104.8	0.093	0.1257
86672.4	53.00	300.3	72.3	1.006	10.3	0.37	-2.54	69.7	0.136	0.0836
86671.7	52.64	300.0	76.1	1.006	10.2	0.37	-2.52	73.6	0.136	0.0882
86672.2	52.08	299.9	81.8	1.007	10.2	0.37	-2.49	79.3	0.135	0.0950
86672.8	52.23	299.8	81.7	1.007	10.2	0.37	-2.50	79.2	0.135	0.0948
86654.6	74.61	300.1	57.6	1.006	12.2	0.25	-3.65	53.9	0.162	0.0646
86655.6	74.87	300.0	63.8	1.006	12.2	0.25	-3.66	60.1	0.162	0.0720
86655.9	75.20	300.3	63.2	1.005	12.2	0.25	-3.68	59.5	0.162	0.0714
86628.9	100.48	300.0	41.0	1.006	14.1	0.16	-5.02	36.0	0.187	0.0431
86629.8	99.62	300.3	44.4	1.005	14.1	0.16	-4.98	39.4	0.187	0.0473
86629.8	99.35	300.1	41.0	1.006	14.1	0.16	-4.96	36.0	0.186	0.0432
86596.7	130.62	299.9	23.5	1.006	16.1	0.09	-6.67	16.9	0.214	0.0202
86597.1	131.57	299.8	22.8	1.006	16.2	0.09	-6.72	16.1	0.214	0.0192
86567.1	163.90	300.5	5.8	1.004	18.1	0.04	-8.55	-2.8	0.240	-0.0033
86566.9	163.92	300.5	5.8	1.004	18.1	0.04	-8.55	-2.8	0.240	-0.0033
86530.0	200.87	300.0	-17.0	1.005	20.0	0.01	-10.69	-27.7	0.265	-0.0332
86530.0	200.25	299.9	-17.4	1.005	20.0	0.01	-10.65	-28.0	0.265	-0.0336
86528.9	200.93	299.8	-19.5	1.006	20.0	0.01	-10.69	-30.2	0.265	-0.0362
86566.0	163.55	299.9	4.3	1.006	18.0	0.04	-8.52	-4.2	0.239	-0.0051
86566.3	163.35	299.9	13.7	1.005	18.0	0.04	-8.51	5.2	0.239	0.0062
86566.5	163.72	300.1	3.7	1.005	18.1	0.04	-8.54	-4.9	0.239	-0.0058
86601.0	132.38	300.1	24.0	1.005	16.2	0.09	-6.77	17.2	0.215	0.0206
86601.3	131.86	300.4	22.0	1.004	16.2	0.09	-6.74	15.2	0.215	0.0183
86633.3	101.00	300.1	45.2	1.006	14.2	0.16	-5.05	40.2	0.188	0.0482
86633.7	101.38	299.8	39.5	1.007	14.2	0.16	-5.07	34.5	0.188	0.0413
86659.8	74.00	299.7	64.7	1.007	12.1	0.25	-3.62	61.1	0.161	0.0731
86659.6	74.02	299.8	56.8	1.007	12.1	0.25	-3.62	53.2	0.161	0.0637
86659.1	73.75	299.7	58.3	1.007	12.1	0.25	-3.60	54.7	0.160	0.0655
86678.9	52.82	299.6	81.2	1.008	10.2	0.37	-2.53	78.7	0.136	0.0941
86678.9	53.08	299.4	73.8	1.008	10.3	0.37	-2.54	71.3	0.136	0.0853
86711.5	24.58	299.6	101.3	1.008	7.0	0.75	-1.13	100.1	0.093	0.1198
86713.0	24.58	299.8	99.3	1.008	7.0	0.75	-1.13	98.2	0.093	0.1175
86711.7	24.29	299.8	99.8	1.008	6.9	0.75	-1.12	98.7	0.092	0.1181

Table D6 0° Pitch Angle at 800 RPM

Pitch Angle (deg)	Propeller speed (rpm)	Blade A (deg)	Blade B (deg)
0	800	0.1	0.0

Zero Values:	Static Pressure (Pa)	Dynamic Pressure (Pa)	Temperature (K)	Pre load (N)
	86910.5	-1.41	298.5	99.1

Static Pressure (Pa)	Dynamic Pressure (Pa)	Temperature (K)	Corrected Load (N)	Air Density (kg/cu. m)	Tunnel Velocity (m/sec)	Induced Vel. Component (-)	Tare Drag (N)	Thrust (N)	Advance Ratio (-)	Thrust Coefficient (-)
86892.5	14.88	298.3	57.1	1.015	5.4	0.72	-2.08	59.2	0.108	0.1583
86890.7	19.11	298.2	53.5	1.015	6.1	0.59	-2.29	55.8	0.122	0.1490
86890.7	18.71	298.4	53.7	1.015	6.1	0.59	-2.24	55.9	0.121	0.1496
86872.9	33.60	298.4	42.2	1.014	8.1	0.34	-2.91	45.1	0.162	0.1206
86872.4	33.74	298.5	42.7	1.014	8.2	0.34	-2.92	45.6	0.162	0.1220
86854.0	52.09	298.2	30.6	1.015	10.1	0.20	-3.67	34.2	0.202	0.0915
86853.5	51.57	298.0	30.7	1.015	10.1	0.20	-3.63	34.3	0.201	0.0916
86834.0	74.01	298.3	16.8	1.014	12.1	0.11	-4.53	21.4	0.240	0.0572
86808.1	99.95	298.2	3.8	1.014	14.0	0.05	-5.57	9.4	0.279	0.0251
86807.4	99.90	298.1	4.9	1.014	14.0	0.05	-5.56	10.4	0.279	0.0279
86775.0	133.38	297.9	-11.2	1.015	16.2	0.01	-6.89	-4.3	0.323	-0.0114
86778.1	133.42	297.9	-12.9	1.015	16.2	0.01	-6.89	-6.0	0.323	-0.0161
86749.4	164.53	298.0	-28.1	1.014	18.0	-0.02	-8.13	-19.9	0.358	-0.0533
86750.7	164.43	298.0	-27.0	1.014	18.0	-0.02	-8.12	-18.9	0.358	-0.0505
86712.2	202.15	297.8	-34.1	1.014	20.0	-0.05	-9.62	-24.5	0.397	-0.0655
86714.1	203.19	297.7	-34.9	1.015	20.0	-0.05	-9.68	-25.2	0.398	-0.0674
86754.8	164.41	297.8	-27.8	1.015	18.0	-0.02	-8.12	-19.6	0.358	-0.0525
86753.9	165.34	297.6	-27.9	1.016	18.0	-0.02	-8.17	-19.7	0.359	-0.0526
86788.7	132.52	297.7	-11.8	1.016	16.2	0.01	-6.84	-4.9	0.321	-0.0132
86790.2	133.24	297.7	-11.1	1.016	16.2	0.01	-6.88	-4.2	0.322	-0.0113
86825.7	99.81	297.8	3.9	1.016	14.0	0.05	-5.56	9.5	0.279	0.0254
86826.3	99.45	297.6	3.2	1.016	14.0	0.05	-5.54	8.7	0.278	0.0233
86850.9	74.74	297.5	17.2	1.017	12.1	0.11	-4.58	21.8	0.241	0.0581
86851.2	74.46	297.6	16.6	1.017	12.1	0.11	-4.56	21.1	0.241	0.0563
86874.2	52.54	297.8	29.7	1.016	10.2	0.20	-3.71	33.4	0.202	0.0890
86875.7	52.02	297.7	30.0	1.017	10.1	0.20	-3.67	33.6	0.201	0.0898
86898.8	34.39	297.7	42.5	1.017	8.2	0.34	-2.98	45.4	0.164	0.1212
86899.2	33.49	297.5	43.3	1.018	8.1	0.34	-2.90	46.2	0.161	0.1232
86917.2	19.46	297.5	55.6	1.018	6.2	0.57	-2.29	57.9	0.123	0.1543
86917.3	19.26	297.5	55.1	1.018	6.2	0.57	-2.26	57.4	0.122	0.1530
86923.8	14.83	297.4	58.2	1.018	5.4	0.72	-2.08	60.3	0.107	0.1606
86923.1	14.15	297.3	58.9	1.018	5.3	0.75	-2.05	61.0	0.105	0.1624

Table D7 0° Pitch Angle at 1200 RPM

Pitch Angle (deg)	Propeller speed (rpm)	Blade A (deg)	Blade B (deg)
0	1200	0.0	0.0

Zero Values:	Static Pressure (Pa)	Dynamic Pressure (Pa)	Temperature (K)	Pre load (N)
	86792.7	-1.84	300.3	99.4

Static Pressure (Pa)	Dynamic Pressure (Pa)	Temperature (K)	Corrected Load (N)	Air Density (kg/cu. m)	Tunnel Velocity (m/sec)	Induced Vel. Component (-)	Tare Drag (N)	Thrust (N)	Advance Ratio (-)	Thrust Coefficient (-)
86759.8	29.23	300.9	123.5	1.004	7.6	0.10	0.79	-4.7	128.182	0.1539
86759.2	31.61	301.5	121.4	1.002	7.9	0.11	0.79	-5.1	126.522	0.1522
86735.5	53.70	300.5	105.5	1.005	10.3	0.14	0.49	-6.0	111.541	0.1338
86734.2	52.71	300.3	103.8	1.006	10.2	0.14	0.49	-5.9	109.660	0.1314
86711.5	74.38	300.4	92.3	1.005	12.2	0.16	0.35	-6.9	99.207	0.1190
86710.9	73.83	299.8	96.7	1.007	12.1	0.16	0.35	-6.8	103.532	0.1239
86710.4	73.11	300.2	99.3	1.006	12.1	0.16	0.35	-6.8	106.052	0.1271
86710.0	72.33	300.2	93.9	1.006	12.0	0.16	0.35	-6.7	100.593	0.1205
86680.2	100.52	300.6	73.9	1.005	14.1	0.19	0.24	-8.0	81.892	0.0983
86680.7	101.83	300.1	73.6	1.006	14.2	0.19	0.24	-8.1	81.675	0.0979
86649.6	130.92	299.5	55.2	1.008	16.1	0.21	0.17	-9.5	64.662	0.0774
86651.1	129.62	300.4	60.6	1.005	16.1	0.21	0.17	-9.4	69.971	0.0839
86618.4	163.60	300.0	37.6	1.006	18.0	0.24	0.12	-10.8	48.471	0.0581
86619.3	163.17	301.0	37.7	1.003	18.0	0.24	0.12	-10.8	48.551	0.0584
86581.3	199.29	300.9	21.8	1.002	19.9	0.26	0.07	-12.4	34.164	0.0411
86578.9	199.83	300.5	17.1	1.004	20.0	0.26	0.07	-12.4	29.510	0.0355
86578.4	198.14	300.8	18.4	1.003	19.9	0.26	0.07	-12.3	30.674	0.0369
86533.4	243.51	300.6	-2.1	1.003	22.0	0.29	0.04	-14.3	12.254	0.0147
86534.5	242.79	301.2	-5.0	1.001	22.0	0.29	0.04	-14.3	9.273	0.0112
86531.3	243.26	299.9	-1.2	1.005	22.0	0.29	0.04	-14.3	13.046	0.0156
86477.3	294.33	299.3	-27.7	1.007	24.2	0.32	0.01	-16.6	-11.025	-0.0132
86478.8	293.50	300.3	-28.9	1.003	24.2	0.32	0.01	-16.6	-12.355	-0.0148
86478.4	294.75	300.0	-27.6	1.004	24.2	0.32	0.01	-16.7	-10.923	-0.0131
86476.9	295.15	300.2	-31.7	1.003	24.3	0.32	0.01	-16.7	-14.967	-0.0180
86526.2	241.22	300.6	-2.1	1.003	21.9	0.29	0.04	-14.2	12.092	0.0145
86526.7	244.02	301.2	-1.8	1.001	22.1	0.29	0.04	-14.3	12.565	0.0151
86569.7	199.99	300.5	17.7	1.003	20.0	0.26	0.07	-12.4	30.116	0.0362
86568.2	199.84	301.2	18.2	1.001	20.0	0.26	0.07	-12.4	30.646	0.0369
86604.8	163.34	300.9	37.7	1.003	18.0	0.24	0.12	-10.8	48.555	0.0584
86606.7	164.66	301.0	37.5	1.002	18.1	0.24	0.12	-10.9	48.457	0.0583
86638.3	132.09	301.3	56.9	1.002	16.2	0.22	0.17	-9.6	66.447	0.0800
86637.6	132.34	301.2	54.3	1.002	16.3	0.22	0.17	-9.6	63.850	0.0768
86637.8	132.26	301.3	55.8	1.002	16.2	0.22	0.17	-9.6	65.365	0.0787
86666.7	102.09	300.4	78.9	1.005	14.3	0.19	0.24	-8.1	87.073	0.1044
86665.2	101.3	300.0	74.5	1.006	14.19	0.19	0.2	-8.1	82.573	0.099
86664.8	101.8	300.9	69.9	1.003	14.25	0.19	0.2	-8.1	78.027	0.094
86689.6	73.9	299.7	97.9	1.008	12.11	0.16	0.3	-6.8	104.702	0.125

Static Pressure	Dynamic Pressure	Temperature	Corrected Load	Air Density	Tunnel Velocity	Induced Vel. Component	Tare Drag	Thrust	Advance Ratio	Thrust Coefficient
(Pa)	(Pa)	(K)	(N)	(kg/cu. m)	(m/sec)	(-)	(N)	(N)	(-)	(-)
86686.3	74.2	299.5	98.0	1.008	12.13	0.16	0.3	-6.9	104.860	0.125
86702.6	51.6	300.1	112.3	1.006	10.13	0.13	0.5	-5.7	118.036	0.141
86701.1	51.0	300.1	104.3	1.006	10.07	0.13	0.5	-5.7	109.994	0.132
86698.7	52.5	300.8	110.3	1.004	10.23	0.14	0.5	-5.9	116.121	0.139
86717.6	28.9	300.3	132.6	1.006	7.57	0.10	0.8	-4.6	137.237	0.164
86717.2	29.0	300.3	130.3	1.006	7.59	0.10	0.8	-4.6	134.903	0.162

Table D8 2° Pitch Angle at 800 RPM

Pitch Angle (deg)	Propeller speed (rpm)	Blade A (deg)	Blade B (deg)
2	800	2.0	2.0

Zero Values:	Static Pressure (Pa)	Dynamic Pressure (Pa)	Temperature (K)	Pre load (N)
	87088.8	-1.08	295.3	99.5

Static Pressure (Pa)	Dynamic Pressure (Pa)	Temperature (K)	Corrected Load (N)	Air Density (kg/cu. m)	Tunnel Velocity (m/sec)	Induced Vel. Component (-)	Tare Drag (N)	Thrust (N)	Advance Ratio (-)	Thrust Coefficient (-)
87072.7	15.51	295.6	63.2	1.026	5.5	0.76	-2.28	65.5	0.109	0.1732
87071.0	14.31	295.0	64.6	1.028	5.3	0.80	-2.21	66.8	0.105	0.1763
87064.7	17.79	296.4	61.0	1.023	5.9	0.68	-2.39	63.4	0.117	0.1680
87063.0	18.27	295.3	60.9	1.027	6.0	0.67	-2.43	63.4	0.119	0.1673
87045.8	33.46	296.7	49.5	1.022	8.1	0.39	-3.12	52.7	0.161	0.1398
87047.5	34.63	296.0	49.2	1.025	8.2	0.38	-3.17	52.4	0.164	0.1386
87028.2	53.08	294.7	37.3	1.029	10.2	0.24	-3.97	41.3	0.202	0.1090
87025.8	51.71	294.4	38.2	1.030	10.0	0.24	-3.92	42.1	0.199	0.1108
87001.8	74.69	294.4	25.3	1.029	12.0	0.15	-4.87	30.2	0.240	0.0795
86999.0	72.28	295.9	25.9	1.024	11.9	0.15	-4.77	30.6	0.236	0.0811
86967.5	100.04	294.0	12.1	1.031	13.9	0.08	-5.93	18.0	0.277	0.0475
86930.7	132.91	294.5	-0.7	1.028	16.1	0.03	-7.27	6.6	0.320	0.0174
86930.1	133.68	294.7	-3.7	1.027	16.1	0.03	-7.30	3.6	0.321	0.0095
86928.3	133.17	294.6	-0.9	1.028	16.1	0.03	-7.28	6.4	0.320	0.0168
86893.6	165.08	293.9	-16.0	1.030	17.9	0.00	-8.61	-7.4	0.356	-0.0194
86892.3	164.94	294.9	-18.0	1.026	17.9	0.00	-8.61	-9.4	0.357	-0.0250
86848.5	202.47	295.7	-35.4	1.023	19.9	-0.03	-10.15	-25.3	0.396	-0.0671
86846.1	202.27	294.7	-34.1	1.027	19.9	-0.03	-10.16	-24.0	0.395	-0.0633
86804.8	244.01	295.5	-41.1	1.023	21.8	-0.05	-11.92	-29.1	0.434	-0.0773
86802.4	243.93	294.4	-36.5	1.027	21.8	-0.05	-11.91	-24.6	0.434	-0.0649
86801.4	243.11	295.4	-38.3	1.024	21.8	-0.05	-11.87	-26.4	0.434	-0.0699
86801.4	244.22	296.0	-40.9	1.022	21.9	-0.05	-11.93	-29.0	0.435	-0.0769
86840.3	206.07	295.7	-35.1	1.023	20.1	-0.03	-10.31	-24.8	0.399	-0.0656
86839.2	205.59	294.9	-34.8	1.026	20.0	-0.03	-10.28	-24.6	0.398	-0.0650
86878.3	166.96	294.5	-17.6	1.028	18.0	0.00	-8.68	-8.9	0.359	-0.0235
86877.5	166.56	294.2	-18.8	1.029	18.0	0.00	-8.66	-10.2	0.358	-0.0268
86907.9	134.47	294.7	-2.2	1.027	16.2	0.03	-7.33	5.2	0.322	0.0136
86909.0	135.04	295.7	-2.2	1.024	16.2	0.03	-7.35	5.2	0.323	0.0137
86937.7	99.90	295.4	12.8	1.025	14.0	0.82	-18.59	31.4	0.278	0.0831
86959.4	74.02	295.6	25.4	1.025	12.0	0.08	-4.28	29.7	0.239	0.0785
86956.6	74.94	295.5	25.6	1.025	12.1	0.08	-4.33	29.9	0.241	0.0792
86980.3	52.29	295.6	38.7	1.025	10.1	0.24	-3.93	42.6	0.201	0.1127
86979.7	52.45	296.0	37.6	1.024	10.1	0.24	-3.95	41.5	0.201	0.1100
86995.3	33.19	296.5	50.1	1.022	8.1	0.39	-3.11	53.2	0.160	0.1413
86996.2	33.8	296.0	49.9	1.024	8.13	0.39	-3.2	53.1	0.162	0.141
87014.7	18.5	296.4	60.4	1.023	6.02	0.66	-2.4	62.8	0.120	0.167
87014.2	18.6	296.8	60.0	1.021	6.03	0.66	-2.4	62.5	0.120	0.166

Static Pressure	Dynamic Pressure	Temperature	Corrected Load	Air Density	Tunnel Velocity	Induced Vel. Component	Tare Drag	Thrust	Advance Ratio	Thrust Coefficient
(Pa)	(Pa)	(K)	(N)	(kg/cu. m)	(m/sec)	(-)	(N)	(N)	(-)	(-)
87013.4	15.3	295.6	63.3	1.026	5.47	0.77	-2.3	65.6	0.109	0.173
87013.4	14.7	295.9	63.6	1.024	5.36	0.77	-2.2	65.8	0.107	0.174

Table D9 2° Pitch Angle at 1200 RPM

Pitch Angle (deg)	Propeller speed (rpm)	Blade A (deg)	Blade B (deg)
2	1200	2.0	2.0

Zero Values:	Static Pressure (Pa)	Dynamic Pressure (Pa)	Temperature (K)	Pre load (N)
	86878.8	-1.90	298.4	99.9

Static Pressure (Pa)	Dynamic Pressure (Pa)	Temperature (K)	Corrected Load (N)	Air Density (kg/cu. m)	Tunnel Velocity (m/sec)	Induced Vel. Component (-)	Tare Drag (N)	Thrust (N)	Advance Ratio (-)	Thrust Coefficient (-)
86838.7	31.11	298.5	238.7	1.013	8.1	0.78	-5.24	144.1	0.107	0.1714
86837.0	31.51	298.3	237.9	1.014	8.1	0.78	-5.31	143.4	0.108	0.1704
86814.0	50.98	299.3	222.4	1.010	10.2	0.53	-6.32	128.9	0.136	0.1538
86812.6	49.71	298.7	227.1	1.012	10.1	0.55	-6.26	133.5	0.134	0.1589
86790.9	70.99	299.4	207.2	1.010	12.0	0.40	-7.32	114.7	0.159	0.1369
86790.9	70.93	300.1	209.6	1.007	12.0	0.40	-7.31	117.1	0.159	0.1401
86760.5	99.09	299.0	195.9	1.011	14.1	0.28	-8.64	104.6	0.187	0.1248
86759.6	97.18	299.4	197.7	1.009	14.0	0.28	-8.47	106.3	0.186	0.1270
86722.8	128.99	299.4	167.1	1.009	16.1	0.20	-10.03	77.3	0.214	0.0924
86717.8	129.30	299.5	172.4	1.009	16.1	0.20	-10.06	82.6	0.214	0.0988
86689.8	161.60	300.3	156.7	1.006	18.0	0.15	-11.59	68.5	0.239	0.0821
86688.3	160.33	299.5	157.5	1.008	17.9	0.15	-11.49	69.1	0.238	0.0827
86644.5	199.02	299.2	137.0	1.009	20.0	0.10	-13.22	50.4	0.265	0.0603
86642.4	199.60	299.6	137.0	1.007	20.0	0.10	-13.27	50.5	0.265	0.0604
86595.8	241.20	299.2	117.2	1.008	22.0	0.06	-15.15	32.5	0.291	0.0389
86595.4	241.60	299.0	115.3	1.009	22.0	0.06	-15.18	30.6	0.291	0.0366
86545.6	290.11	300.3	92.3	1.004	24.1	0.03	-17.46	9.9	0.320	0.0119
86543.4	287.87	299.3	98.2	1.007	24.0	0.03	-17.30	15.7	0.318	0.0187
86485.6	341.62	300.3	66.9	1.003	26.2	0.01	-19.80	-13.1	0.347	-0.0158
86486.0	341.82	299.9	68.0	1.005	26.2	0.01	-19.81	-12.1	0.347	-0.0145
86485.8	341.46	299.6	67.4	1.006	26.1	0.01	-19.78	-12.7	0.347	-0.0152
86483.8	341.19	298.8	63.7	1.008	26.1	0.01	-19.76	-16.4	0.346	-0.0196
86532.5	288.70	298.6	95.7	1.010	24.0	0.03	-17.35	13.2	0.318	0.0157
86579.3	241.40	299.2	115.7	1.008	22.0	0.06	-15.17	31.1	0.291	0.0372
86577.4	241.59	299.8	113.8	1.006	22.0	0.06	-15.18	29.2	0.292	0.0349
86621.7	198.97	299.8	138.2	1.006	20.0	0.10	-13.22	51.6	0.265	0.0618
86658.2	158.12	300.0	157.7	1.006	17.8	0.15	-11.32	69.1	0.237	0.0828
86656.5	158.08	300.0	156.7	1.006	17.8	0.15	-11.32	68.1	0.237	0.0817
86683.1	127.25	299.0	170.4	1.010	16.0	0.20	-9.88	80.5	0.212	0.0961
86683.0	124.64	299.9	171.4	1.007	15.9	0.20	-9.67	81.2	0.210	0.0972
86711.5	96.46	299.3	190.1	1.009	14.0	0.28	-8.40	98.7	0.185	0.1178
86711.5	95.30	299.9	189.3	1.007	13.9	0.28	-8.29	97.7	0.184	0.1170
86734.2	70.64	300.4	205.4	1.006	12.0	0.40	-7.28	112.9	0.159	0.1353
86733.7	70.5	300.1	214.1	1.007	11.99	0.40	-7.3	121.5	0.159	0.145
86751.6	49.4	299.8	220.1	1.008	10.09	0.55	-6.2	126.5	0.134	0.151
86750.0	49.0	298.9	223.3	1.011	10.04	0.55	-6.2	129.6	0.133	0.155
86767.4	29.9	300.4	234.4	1.006	7.95	0.78	-5.0	139.6	0.105	0.167

Table D10 -4° Pitch Angle at 800 RPM

Pitch Angle (deg)	Propeller speed (rpm)	Blade A (deg)	Blade B (deg)
4	800	-4.0	-4.1

Zero Values:	Static Pressure (Pa)	Dynamic Pressure (Pa)	Temperature (K)	Pre load (N)
	86970.3	-1.73	297.1	99.4

Static Pressure (Pa)	Dynamic Pressure (Pa)	Temperature (K)	Corrected Load (N)	Air Density (kg/cu. m)	Tunnel Velocity (m/sec)	Induced Vel. Component (-)	Tare Drag (N)	Thrust (N)	Advance Ratio (-)	Thrust Coefficient (-)
86965.5	17.95	296.6	73.0	1.021	5.9	0.73	-2.56	75.5	0.118	0.2006
86966.4	18.22	296.6	72.3	1.021	6.0	0.73	-2.60	74.9	0.119	0.1990
86968.3	20.12	296.5	70.3	1.022	6.3	0.66	-2.66	73.0	0.125	0.1937
86969.9	20.65	296.4	70.4	1.022	6.4	0.65	-2.70	73.2	0.126	0.1941
86929.7	54.13	296.2	45.2	1.022	10.3	0.26	-4.25	49.4	0.205	0.1312
86928.6	53.66	296.2	46.2	1.022	10.2	0.26	-4.23	50.5	0.204	0.1339
86949.2	34.67	296.2	58.1	1.023	8.2	0.42	-3.38	61.5	0.164	0.1631
86951.6	34.88	296.1	58.5	1.023	8.3	0.42	-3.40	61.9	0.164	0.1641
86914.2	74.90	296.1	34.2	1.023	12.1	0.17	-5.15	39.3	0.241	0.1044
86916.6	74.27	296.1	34.7	1.022	12.1	0.17	-5.11	39.8	0.240	0.1056
86897.2	101.42	296.0	21.6	1.023	14.1	0.11	-6.30	27.9	0.280	0.0740
86899.8	99.48	296.0	22.7	1.023	13.9	0.11	-6.17	28.8	0.277	0.0764
86869.8	131.01	296.0	8.2	1.022	16.0	0.06	-7.57	15.8	0.318	0.0418
86872.2	131.88	295.9	10.2	1.023	16.1	0.06	-7.62	17.9	0.319	0.0474
86840.0	166.57	295.9	-8.7	1.022	18.1	0.02	-9.11	0.4	0.359	0.0010
86842.0	166.33	295.9	1.0	1.022	18.0	0.02	-9.09	10.1	0.359	0.0269
86807.2	206.50	295.7	-18.9	1.023	20.1	-0.01	-10.83	-8.1	0.400	-0.0214
86807.9	206.35	295.9	-20.8	1.022	20.1	-0.01	-10.82	-9.9	0.400	-0.0264
86795.5	225.14	295.7	-30.1	1.023	21.0	-0.02	-11.65	-18.5	0.417	-0.0490
86794.0	226.27	295.7	-29.4	1.023	21.0	-0.02	-11.71	-17.7	0.419	-0.0470
86813.7	206.45	295.7	-28.0	1.023	20.1	-0.01	-10.83	-17.2	0.400	-0.0456
86814.4	205.97	295.7	-23.3	1.023	20.1	-0.01	-10.80	-12.5	0.399	-0.0331
86854.2	167.72	295.6	-5.2	1.024	18.1	0.02	-9.16	3.9	0.360	0.0104
86856.1	169.04	295.6	-0.4	1.024	18.2	0.02	-9.23	8.8	0.362	0.0234
86887.5	132.78	295.6	5.9	1.024	16.1	0.06	-7.65	13.5	0.320	0.0359
86889.8	134.05	295.6	7.3	1.024	16.2	0.06	-7.70	15.0	0.322	0.0396

Table D11 4° Pitch Angle at 1200 RPM

Pitch Angle (deg)	Propeller speed (rpm)	Blade A (deg)	Blade B (deg)
4	1200	4.1	3.9

Zero Values:	Static Pressure (Pa)	Dynamic Pressure (Pa)	Temperature (K)	Pre load (N)
	86747.0	-0.03	300.6	99.1

Static Pressure (Pa)	Dynamic Pressure (Pa)	Temperature (K)	Corrected Load (N)	Air Density (kg/cu. m)	Tunnel Velocity (m/sec)	Induced Vel. Component (-)	Tare Drag (N)	Thrust (N)	Advance Ratio (-)	Thrust Coefficient (-)
86708.3	32.9	300.3	157.1	1.006	8.1	0.84	-5.58	162.7	0.107	0.1950
86707.8	32.4	300.1	157.5	1.007	8.0	0.85	-5.59	163.1	0.106	0.1954
86687.4	48.5	300.0	147.6	1.007	9.8	0.62	-6.51	154.1	0.130	0.1845
86688.0	48.4	300.3	140.7	1.006	9.8	0.62	-6.50	147.2	0.130	0.1765
86687.4	48.2	300.3	141.5	1.006	9.8	0.62	-6.47	148.0	0.130	0.1774
86663.5	71.6	300.2	125.0	1.006	11.9	0.44	-7.71	132.7	0.158	0.1591
86662.0	71.6	300.0	125.3	1.006	11.9	0.44	-7.72	133.1	0.158	0.1594
86630.4	98.0	300.5	115.2	1.004	14.0	0.33	-9.03	124.2	0.185	0.1491
86629.1	98.9	300.6	107.8	1.004	14.0	0.32	-9.06	116.8	0.186	0.1403
86627.8	99.0	300.1	110.2	1.006	14.0	0.32	-9.07	119.2	0.186	0.1430
86596.9	129.5	300.5	87.7	1.004	16.1	0.24	-10.57	98.3	0.213	0.1180
86598.2	130.4	300.3	92.6	1.005	16.1	0.24	-10.61	103.2	0.214	0.1238
86596.5	129.3	299.6	88.6	1.007	16.0	0.24	-10.54	99.2	0.213	0.1188
86562.8	160.7	299.5	77.6	1.007	17.9	0.18	-12.06	89.6	0.237	0.1073
86563.0	160.6	299.6	77.2	1.006	17.9	0.18	-12.05	89.3	0.237	0.1070
86520.6	201.0	300.1	53.7	1.004	20.0	0.13	-14.00	67.7	0.265	0.0813
86521.7	201.4	300.2	55.5	1.004	20.0	0.13	-14.03	69.5	0.266	0.0835
86477.1	245.3	299.8	35.1	1.005	22.1	0.09	-16.09	51.2	0.293	0.0614
86477.5	244.7	300.4	31.1	1.003	22.1	0.09	-16.06	47.2	0.293	0.0567
86432.3	289.0	300.5	11.5	1.002	24.0	0.06	-18.17	29.7	0.319	0.0357
86432.9	289.2	300.7	13.0	1.001	24.0	0.06	-18.19	31.2	0.319	0.0376
86382.5	339.9	300.0	-7.2	1.003	26.0	0.03	-20.67	13.5	0.345	0.0162
86380.3	339.4	300.6	-7.8	1.001	26.0	0.03	-20.65	12.9	0.345	0.0155
86327.3	388.2	300.4	-35.7	1.001	27.9	0.01	-23.05	-12.6	0.369	-0.0152
86326.4	388.8	300.1	-35.9	1.002	27.9	0.01	-23.09	-12.8	0.369	-0.0154
86377.1	337.0	300.3	-8.3	1.002	25.9	0.03	-20.52	12.2	0.344	0.0147
86376.6	338.1	300.3	-10.2	1.002	26.0	0.03	-20.55	10.4	0.345	0.0125
86427.3	288.3	300.1	12.6	1.003	24.0	0.06	-18.16	30.8	0.318	0.0370
86427.3	288.1	300.0	10.3	1.003	24.0	0.06	-18.15	28.5	0.318	0.0342
86470.8	244.1	300.1	32.1	1.004	22.1	0.09	-16.04	48.1	0.292	0.0578
86474.0	244.5	300.3	32.1	1.003	22.1	0.88	-56.21	88.3	0.293	0.1062
86518.4	200.4	300.9	55.1	1.002	20.0	0.13	-13.95	69.1	0.265	0.0831
86517.8	201.3	300.4	52.4	1.003	20.0	0.13	-14.00	66.4	0.266	0.0798
86559.3	159.0	300.8	74.5	1.002	17.81	0.18	-12.0	86.5	0.236	0.104
86558.0	159.2	300.4	73.9	1.004	17.81	0.18	-12.0	85.9	0.236	0.103
86588.9	128.7	300.1	91.9	1.005	16.00	0.24	-10.5	102.5	0.212	0.123
86588.5	126.5	300.5	91.8	1.004	15.88	0.25	-10.4	102.2	0.211	0.123

Static Pressure	Dynamic Pressure	Temperature	Corrected Load	Air Density	Tunnel Velocity	Induced Vel. Component	Tare Drag	Thrust	Advance Ratio	Thrust Coefficient
(Pa)	(Pa)	(K)	(N)	(kg/cu. m)	(m/sec)	(-)	(N)	(N)	(-)	(-)
86617.8	96.4	300.6	106.9	1.004	13.86	0.33	-8.9	115.8	0.184	0.139
86618.0	96.9	300.7	110.6	1.004	13.89	0.33	-9.0	119.5	0.184	0.144
86618.5	96.7	301.4	112.3	1.001	13.90	0.33	-8.9	121.3	0.184	0.146
86640.6	69.5	301.2	128.2	1.002	11.78	0.45	-7.6	135.8	0.156	0.163
86640.6	69.2	301.0	128.4	1.003	11.75	0.45	-7.5	136.0	0.156	0.163
86663.3	49.6	301.4	135.7	1.002	9.95	0.61	-6.5	142.2	0.132	0.171
86663.9	48.8	301.1	140.2	1.003	9.86	0.62	-6.5	146.7	0.131	0.176
86662.6	50.0	300.3	136.0	1.005	9.98	0.61	-6.6	142.6	0.132	0.171
86676.5	31.9	300.8	157.9	1.004	7.98	0.85	-5.5	163.4	0.106	0.196
86676.3	32.8	300.4	147.1	1.005	8.07	0.84	-5.6	152.6	0.107	0.183

Table D12 8° Pitch Angle at 800 RPM

Pitch Angle (deg)	Propeller speed (rpm)	Blade A (deg)	Blade B (deg)
8	800	8.0	8.0

Zero Values:	Static Pressure (Pa)	Dynamic Pressure (Pa)	Temp. (K)	Pre load (N)
	87051.6	-0.94	296.4	99.5

Static Press. (Pa)	Dyn. Press. (Pa)	Temp. (K)	Corrected Load (N)	Air Density (kg/cu. m)	Tunnel Vel. (m/sec)	Induced Vel. Coeff. (-)	Tare Drag (N)	Thrust (N)	Advance Ratio (-)	Thrust Coeff. (-)
87041.9	20.4	295.4	83.2	1.026	6.3	0.75	-3.00	86.2	0.125	0.0371
87043.6	20.6	295.3	83.0	1.027	6.3	0.74	-3.01	86.0	0.126	0.0368
87032.9	33.3	295.2	72.8	1.027	8.1	0.51	-3.72	76.5	0.160	0.0258
87032.7	32.7	295.2	73.5	1.027	8.0	0.53	-3.74	77.2	0.159	0.0262
87014.0	51.1	295.1	61.8	1.027	10.0	0.35	-4.59	66.4	0.198	0.0181
87015.6	50.7	295.1	61.0	1.027	9.9	0.35	-4.58	65.6	0.198	0.0179
86991.2	74.2	295.1	50.1	1.027	12.0	0.23	-5.69	55.8	0.239	0.0126
86992.3	74.5	295.1	51.2	1.027	12.0	0.23	-5.70	56.9	0.240	0.0128
86993.1	74.3	295.1	50.6	1.027	12.0	0.23	-5.69	56.3	0.239	0.0127
86968.6	100.1	295.2	37.7	1.026	14.0	0.16	-6.89	44.5	0.278	0.0086
86970.3	98.3	295.1	40.7	1.027	13.8	0.16	-6.80	47.5	0.275	0.0093
86938.4	132.6	295.1	24.6	1.026	16.1	0.10	-8.38	33.0	0.320	0.0056
86939.2	132.6	294.9	22.6	1.027	16.1	0.10	-8.38	31.0	0.320	0.0052
86908.3	166.0	295.0	14.8	1.026	18.0	0.07	-9.93	24.7	0.358	0.0037
86908.8	166.5	295.0	10.4	1.026	18.0	0.06	-9.94	20.3	0.358	0.0031
86871.1	207.3	294.8	-4.9	1.026	20.1	0.03	-11.84	6.9	0.400	0.0009
86872.2	208.6	294.9	-5.5	1.026	20.2	0.03	-11.89	6.4	0.401	0.0009
86830.3	249.3	294.8	-19.9	1.026	22.0	0.01	-13.82	-6.1	0.439	-0.0008
86832.5	248.4	294.8	-24.1	1.026	22.0	0.01	-13.79	-10.3	0.438	-0.0013
86786.3	296.1	294.8	-37.3	1.025	24.0	-0.01	-16.05	-21.3	0.478	-0.0024
86789.0	296.2	294.8	-30.6	1.025	24.0	-0.01	-16.05	-14.6	0.478	-0.0016
86842.2	248.2	294.8	-14.6	1.026	22.0	0.01	-13.78	-0.8	0.438	-0.0001
92594.9	139.3	284.9	-	1.132	15.7	0.11	-8.92	8.9	0.312	0.0015
86884.0	208.7	294.8	-9.1	1.027	20.2	0.03	-11.90	2.8	0.401	0.0004
86886.8	207.9	294.7	-0.5	1.027	20.1	0.03	-11.88	11.4	0.400	0.0015
86931.4	167.2	294.8	12.0	1.027	18.0	0.06	-9.99	21.9	0.359	0.0033
86931.2	167.2	294.7	13.7	1.028	18.0	0.06	-9.99	23.7	0.359	0.0036
86967.1	133.3	294.7	25.8	1.028	16.1	0.10	-8.41	34.2	0.320	0.0058
86966.2	132.1	294.8	23.1	1.028	16.0	0.10	-8.37	31.4	0.319	0.0053
87000.8	100.4	294.7	38.6	1.029	14.0	0.16	-6.90	45.5	0.278	0.0088
87000.6	101.3	294.7	36.3	1.028	14.0	0.16	-6.95	43.3	0.279	0.0084
87027.1	75.5	294.8	49.2	1.029	12.1	0.23	-5.75	55.0	0.241	0.0123
87027.5	75.8	294.7	49.2	1.029	12.1	0.23	-5.76	54.9	0.242	0.0123
87051.7	51.6	294.8	60.6	1.029	10.01	0.35	-4.6	65.2	0.199	0.018

Static Press.	Dyn. Press.	Temp.	Corrected Load	Air Density	Tunnel Vel.	Induced Vel. Comp.	Tare Drag	Thrust	Advance Ratio	Thrust Coeff.
(Pa)	(Pa)	(K)	(N)	(kg/cu. m)	(m/sec)	(-)	(N)	(N)	(-)	(-)
87052.7	51.8	294.7	60.4	1.029	10.03	0.34	-4.6	65.1	0.200	0.018
87071.6	34.2	294.8	71.9	1.029	8.15	0.50	-3.8	75.7	0.162	0.025
87073.6	33.8	294.7	71.8	1.029	8.10	0.51	-3.7	75.5	0.161	0.025
87094.3	20.2	294.8	82.8	1.029	6.26	0.75	-3.0	85.8	0.125	0.037
87094.3	21.0	294.7	80.7	1.030	6.39	0.73	-3.0	83.8	0.127	0.036

Table D13 4° Pitch Angle at 1200 RPM

Pitch Angle (deg)	Propeller speed (rpm)	Blade A (deg)	Blade B (deg)
8	1200	4.1	4.0

Zero Values:	Static Pressure (Pa)	Dyna- mic Press (Pa)	Temp. (K)	Pre load (N)
	86716.	-2.33	300.9	99.6

Static Press. (Pa)	Dyn. Press. (Pa)	Temp. (K)	Corrected Load (N)	Air Density (kg/cu. m)	Vel. (m/sec)	Induced Vel. Comp. (-)	Tare Drag (N)	Thrust (N)	Advance Ratio (-)	Thrust Coefft. (-)
86675.7	41.5	300.0	177.7	1.006	9.1	0.79	-6.80	184.5	0.121	0.2210
86675.4	41.1	300.4	182.8	1.005	9.0	0.80	-6.76	189.5	0.120	0.2273
86643.0	73.7	300.8	156.9	1.003	12.1	0.51	-8.77	165.6	0.161	0.1990
86643.5	73.0	300.8	153.3	1.004	12.1	0.51	-8.73	162.1	0.160	0.1947
86619.6	99.5	300.4	136.3	1.005	14.1	0.39	-10.18	146.5	0.187	0.1758
86617.8	99.8	300.2	143.5	1.005	14.1	0.39	-10.20	153.7	0.187	0.1843
86618.5	99.4	300.6	139.7	1.004	14.1	0.39	-10.17	149.8	0.187	0.1799
86587.1	132.4	300.6	122.8	1.003	16.2	0.29	-11.92	134.7	0.215	0.1619
86588.5	130.5	301.0	126.8	1.002	16.1	0.30	-11.81	138.6	0.214	0.1667
86558.0	162.5	300.2	111.1	1.005	18.0	0.24	-13.49	124.6	0.239	0.1496
86559.7	163.3	300.6	108.9	1.003	18.0	0.23	-13.52	122.4	0.239	0.1471
86516.9	207.7	300.3	90.2	1.004	20.3	0.17	-15.81	106.0	0.270	0.1273
86518.2	206.4	301.0	88.2	1.001	20.3	0.17	-15.74	104.0	0.269	0.1252
86475.4	250.3	301.0	67.9	1.001	22.4	0.13	-18.00	85.9	0.297	0.1034
86474.9	248.3	301.0	67.7	1.001	22.3	0.13	-17.92	85.6	0.295	0.1031
86429.2	292.5	300.3	49.1	1.002	24.2	0.10	-20.20	69.3	0.320	0.0833
86429.9	293.4	300.6	44.7	1.002	24.2	0.10	-20.22	64.9	0.321	0.0781
86379.9	344.5	300.8	24.8	1.001	26.2	0.07	-22.88	47.7	0.348	0.0575
86380.8	345.9	300.5	24.4	1.001	26.3	0.07	-22.98	47.4	0.349	0.0571
86377.5	344.4	300.0	26.7	1.003	26.2	0.07	-22.91	49.6	0.348	0.0596
86329.7	392.3	300.9	3.0	0.999	28.0	0.05	-25.42	28.4	0.372	0.0343
86329.7	392.7	300.7	1.2	1.000	28.0	0.05	-25.45	26.7	0.372	0.0322
86278.1	447.2	300.8	-25.1	0.999	29.9	0.03	-28.32	3.2	0.397	0.0038
86279.0	445.2	300.7	-21.1	1.000	29.8	0.04	-28.23	7.2	0.396	0.0087
86332.5	394.0	300.3	-11.4	1.001	28.1	0.05	-25.54	14.1	0.372	0.0170
86331.8	394.0	299.8	-11.6	1.003	28.0	0.05	-25.53	13.9	0.372	0.0167
86332.7	393.6	300.1	-17.2	1.002	28.0	0.05	-25.51	8.3	0.372	0.0100
86383.8	342.6	300.3	5.3	1.002	26.1	0.07	-22.79	28.1	0.347	0.0338
86384.3	340.8	300.6	4.4	1.001	26.1	0.08	-22.70	27.1	0.346	0.0327
86437.9	290.4	300.7	28.0	1.001	24.1	0.10	-20.08	48.1	0.319	0.0579
86436.9	289.6	300.0	29.2	1.004	24.0	0.10	-20.04	49.3	0.319	0.0592
86480.1	248.2	300.7	47.5	1.002	22.3	0.13	-17.90	65.4	0.295	0.0787

Table D14 12.1° Pitch Angle at 800 RPM

Pitch Angle (deg)	Propeller speed (rpm)	Blade A (deg)	Blade B (deg)
12	800	12.1	12.1

Zero Values:	Static Pressure (Pa)	Dyna- mic Press. (Pa)	Temper- ature (K)	Pre load (N)
	86829	-1.25	295.7	99.4

Static Press. (Pa)	Dyn. Press. (Pa)	Temp. (K)	Correct ed Load (N)	Air Density (kg/cu. m)	Tunnel Vel. (m/sec )	Induced Vel. Comp. ( - )	Tare Drag (N)	Thrust (N)	Advance Ratio (-)	Thrust Coefft. (-)
86815.1	20.0	295.2	89.2	1.025	6.2	0.81	-3.15	92.4	0.124	0.2447
86817.7	19.4	295.2	89.7	1.025	6.2	0.82	-3.11	92.8	0.122	0.2458
86805.3	35.4	295.1	81.2	1.025	8.3	0.55	-4.17	85.4	0.165	0.2261
86805.7	35.1	295.1	82.3	1.025	8.3	0.55	-4.16	86.5	0.165	0.2289
86791.6	49.3	294.9	74.2	1.025	9.8	0.42	-4.96	79.2	0.195	0.2094
86792.4	49.1	294.7	73.9	1.026	9.8	0.42	-4.95	78.9	0.195	0.2086
86767.6	73.1	295.0	61.4	1.025	11.9	0.29	-6.16	67.6	0.238	0.1789
86767.9	73.4	295.0	62.3	1.025	12.0	0.29	-6.18	68.4	0.238	0.1812
86739.6	100.7	294.8	51.5	1.025	14.0	0.21	-7.53	59.0	0.279	0.1562
86739.4	100.6	294.6	50.5	1.026	14.0	0.21	-7.52	58.1	0.279	0.1536
86704.8	134.6	294.9	36.4	1.024	16.2	0.14	-9.20	45.5	0.322	0.1206
86704.6	134.1	295.0	39.3	1.024	16.2	0.14	-9.16	48.5	0.322	0.1285
86669.3	168.9	295.0	24.8	1.024	18.2	0.10	-10.87	35.7	0.361	0.0946
86669.4	168.7	295.0	25.7	1.023	18.2	0.10	-10.85	36.5	0.361	0.0969
86632.2	205.6	295.1	13.9	1.023	20.1	0.07	-12.69	26.6	0.399	0.0706
86631.7	206.1	295.1	9.1	1.023	20.1	0.07	-12.72	21.8	0.399	0.0578
86631.7	205.7	294.8	12.5	1.024	20.0	0.07	-12.69	25.2	0.399	0.0668
86587.8	249.5	294.6	-2.6	1.024	22.1	0.04	-14.90	12.3	0.439	0.0326
86588.7	248.9	294.7	-6.7	1.023	22.1	0.04	-14.85	8.2	0.439	0.0217
86588.5	248.2	294.7	-2.3	1.023	22.0	0.04	-14.80	12.5	0.438	0.0332
86546.5	291.4	294.5	-17.6	1.024	23.9	0.02	-17.00	-0.6	0.475	-0.0017
86546.5	292.4	294.7	-21.0	1.023	23.9	0.02	-17.03	-4.0	0.476	-0.0105
86497.5	342.8	294.5	-47.3	1.023	25.9	0.01	-19.61	-27.7	0.515	-0.0734
86497.3	343.4	294.9	-42.9	1.022	25.9	0.01	-19.65	-23.2	0.516	-0.0617
86551.2	291.0	295.0	-32.0	1.022	23.9	0.02	-16.98	-15.0	0.475	-0.0397
86551.2	290.8	295.0	-32.6	1.022	23.9	0.02	-16.97	-15.7	0.475	-0.0416
86597.2	246.5	294.7	-17.0	1.024	21.9	0.04	-14.73	-2.3	0.437	-0.0061
86598.0	246.5	294.5	-17.7	1.024	21.9	0.04	-14.73	-3.0	0.436	-0.0079

## APPENDIX E WIND TUNNEL TEST DATA - SECOND TEST SERIES

Table E1: - 8° Pitch Angle at 1000 RPM

Pitch Angle (deg)	Propeller speed (rpm)	Blade A (deg)	Blade B (deg)
-8	1000	-8	-8

Point #	Static Pressure Pa	Dynamic Pressure Pa	Temperature K	Thrust N	Tacho Voltage V	Prop Speed rpm	Armature Voltage V	Armature Current A	Air Density kg/m <sup>3</sup>	Tunnel Velocity m/s
0	86281.7	1.00	304.7	0.00	0.00	0.0	0.0	0.0	0.987	1.42
1	86279.2	0.92	304.5	-0.28	0.00	0.0	0.0	0.0	0.987	1.37
2	86280.9	0.80	304.4	-0.18	0.00	0.0	0.0	0.0	0.988	1.27
3	86277.3	14.13	305.2	63.09	25.86	992.2	62.4	12.4	0.985	5.36
4	86276.3	18.07	304.9	57.40	25.87	992.2	62.1	12.4	0.986	6.05
5	86283.2	31.30	305.3	45.96	25.88	992.6	61.8	11.3	0.985	7.97
6	86287.2	48.98	305.1	29.39	25.89	993.0	61.3	9.3	0.985	9.97
7	86283.4	70.81	304.7	10.39	25.90	993.4	60.8	7.0	0.987	11.98
8	86281.9	96.05	304.9	-7.36	25.90	993.7	60.3	4.4	0.986	13.96
9	86275.6	127.21	305.5	-31.42	25.91	993.7	59.7	1.7	0.984	16.08
10	86275.6	143.98	305.4	-44.32	25.90	993.7	59.2	0.3	0.984	17.10
11	86276.6	156.90	305.7	-49.53	26.45	1014.8	60.0	-0.2	0.983	17.86
12	86273	157.72	305.6	-51.57	26.34	1010.6	59.9	-0.3	0.984	17.91
13	86271.5	141.10	305.4	-40.43	25.91	994.1	59.1	0.4	0.984	16.93
14	86273.2	127.37	305.5	-31.90	25.90	993.7	59.4	1.6	0.984	16.09
15	86277.6	95.28	305.5	-6.32	25.90	993.7	60.0	4.3	0.984	13.92
16	86278.1	70.73	305.3	10.84	25.91	994.1	60.5	7.1	0.985	11.99
17	86282	51.77	305.6	26.82	25.91	994.1	60.8	9.1	0.984	10.26
18	86277.3	32.59	305.4	43.45	25.91	994.1	60.9	10.9	0.984	8.14
19	86281.4	17.15	305.7	60.89	25.91	994.1	61.3	12.6	0.983	5.91
20	86288.7	14.78	305.5	61.23	25.91	994.1	61.3	12.5	0.984	5.48
21	86286.8	1.30	305.3	-1.14	0.00	0.0	0.0	0.0	0.985	1.63

Table E2 -4° Pitch Angle at 1000 RPM

Pitch Angle (deg)	Propeller speed (rpm)	Blade A (deg)	Blade B (deg)
-4	1000	4	4

Point #	Static Pressure Pa	Dynamic Pressure Pa	Temperature K	Thrust N	Tacho Voltage V	Prop Speed rpm	Armature Voltage V	Armature Current A	Air Density kg/m <sup>2</sup>	Tunnel Velocity m/s
0	86302.4	0.87	305.1	0.00	0.00	0.0	0.0	0.0	0.986	1.33
1	86303.5	0.71	305.0	0.12	0.00	0.0	0.0	0.0	0.986	1.20
2	86299.9	0.76	305.2	0.05	0.28	0.0	0.0	0.0	0.985	1.25
3	86296.1	17.27	305.1	80.93	25.83	991.1	63.7	16.4	0.985	5.92
4	86288.5	31.51	305.8	68.45	25.86	992.2	63.3	14.8	0.983	8.01
5	86294.8	49.06	305.3	54.02	25.88	993.0	62.9	13.4	0.985	9.98
6	86298.1	71.11	305.3	36.07	25.88	993.0	62.3	11.8	0.985	12.02
7	86297.8	98.11	305.5	18.17	25.89	993.4	61.7	9.3	0.984	14.12
8	86297.0	126.95	305.2	2.20	25.90	993.7	60.9	5.5	0.985	16.05
9	86295.1	158.83	305.1	-19.31	25.91	994.1	60.3	2.8	0.985	17.95
10	86296.3	178.72	305.3	-32.80	25.91	994.1	59.7	0.8	0.985	19.05
11	86292.6	196.36	305.2	-42.01	26.19	1004.9	59.4	-0.3	0.985	19.97
12	86292.7	196.63	305.0	-41.66	26.19	1004.9	59.7	-0.3	0.986	19.97
13	86292.1	177.82	305.3	-31.74	25.91	994.1	59.7	0.7	0.985	19.00
14	86292.1	160.26	305.2	-20.73	25.91	994.1	60.0	2.5	0.985	18.04
15	86289.3	128.57	304.8	-1.02	25.91	994.1	60.5	5.5	0.987	16.14
16	86285.8	99.18	305.4	19.42	25.91	994.1	61.1	9.1	0.984	14.20
17	86284.2	72.37	304.8	36.84	25.91	994.1	61.5	12.1	0.986	12.11
18	86285.3	52.29	304.6	52.38	25.91	994.1	61.7	13.8	0.987	10.29
19	86286.7	35.10	305.2	66.49	25.91	994.1	62.0	15.5	0.985	8.44
20	86284.8	18.29	305.2	79.56	25.91	994.1	62.1	16.7	0.985	6.09
21	86285.2	3.16	305.0	0.79	0.00	0.0	0.0	0.0	0.986	2.53

Table E3 0° Pitch Angle at 800 RPM

Pitch Angle (deg)	Propeller speed (rpm)	Blade A (deg)	Blade B (deg)
0	800	0	0

Point #	Static Pressure Pa	Dynamic Pressure Pa	Temperature K	Thrust N	Tacho Voltage V	Prop Speed rpm	Armature Voltage V	Armature Current A	Air Density kg/m <sup>2</sup>	Tunnel Velocity m/s
0	86529.8	0.00	298.7	0.00	0.00	0.0	0.0	0.0	1.0094	0.00
1	86525.8	0.00	298.6	0.76	0.00	0.0	0.0	0.0	1.0098	0.00
2	86532.5	0.00	298.4	-1.85	0.00	0.0	0.0	0.0	1.0103	0.00
3	86535.2	0.16	298.3	-2.72	0.25	0.0	1.2	2.3	1.0107	0.56
4	86537.6	0.58	298.4	-3.06	0.25	0.0	1.2	2.3	1.0106	1.08
5	86533.6	8.34	297.9	68.99	20.72	795.0	50.2	16.3	1.0121	4.06
6	86535.9	16.73	297.7	61.38	20.72	795.0	50.1	15.6	1.0127	5.75
7	86533.9	30.44	297.6	50.62	20.72	795.0	50.1	14.5	1.0133	7.75
8	86533.3	46.27	297.5	39.39	20.74	795.8	49.9	12.9	1.0134	9.56
9	86533.1	48.81	297.4	36.72	20.74	795.8	49.9	12.9	1.0137	9.81
10	86537.5	78.60	297.4	19.65	20.75	796.2	49.5	10.3	1.0139	12.45
11	86539.8	99.29	297.3	7.98	20.76	796.6	48.9	7.9	1.0141	13.99
12	86539.8	129.43	297.3	-7.88	20.76	796.6	48.4	4.6	1.0141	15.98
13	86544.8	159.88	297.3	-23.25	20.76	796.6	47.8	1.3	1.0143	17.76
14	86547.3	128.80	297.3	-8.35	20.76	796.6	48.3	5.0	1.0142	15.94
15	86554.5	98.97	297.3	7.89	20.77	797.0	49.1	7.7	1.0143	13.97
16	86558.7	75.70	297.3	20.15	20.77	797.0	49.5	10.6	1.0146	12.22
17	86557.6	53.00	297.4	34.69	20.77	797.0	49.9	12.9	1.0142	10.22
18	86562.3	33.37	297.3	47.77	20.76	796.6	50.1	14.6	1.0144	8.11
19	86567.2	15.74	297.3	60.90	20.76	796.6	50.3	15.6	1.0145	5.57
20	86570.4	11.21	297.2	67.11	20.76	796.6	50.3	15.9	1.0148	4.70
21	86569.7	0.77	297.7	-3.61	0.00	0.0	0.0	0.0	1.0133	1.23
22	86566.4	0.00	298.2	-2.38	0	0.0	0	0	1.0116	0.00
23	86943.9	0.46	298.8	-6.49	0	0.0	0	0	1.0140	0.95
24	86942.2	0.46	298.6	-9.02	0	0.0	0	0	1.0145	0.95

Table E4 0° Pitch Angle at 1200 RPM

Pitch Angle (deg)	Propeller speed (rpm)	Blade A (deg)	Blade B (deg)
0	1200	0	0

Point #	Static Pressure Pa	Dynamic Pressure Pa	Temperature K	Thrust N	Tacho Voltage V	Prop Speed rpm	Armature Voltage V	Armature Current A	Air Density kg/m <sup>3</sup>	Tunnel Velocity m/s
0	86581.1	0.00	297.5	0.00	0.00	0.0	0.0	0.0	1.0141	0.00
1	86573.8	0.00	297.4	0.54	0.00	0.0	0.0	0.0	1.0142	0.00
2	86580.3	0.02	297.4	0.16	0.24	0.0	1.3	2.1	1.0144	0.19
3	86585.6	28.59	297.1	149.97	30.94	1187.1	75.1	31.5	1.0154	7.50
4	86588.6	32.48	297.1	144.88	30.93	1186.7	74.9	31.7	1.0154	8.00
5	86586.9	48.78	297.1	134.11	31.01	1189.8	75.3	31.0	1.0154	9.80
6	86585.5	67.35	297.1	117.96	30.96	1187.8	74.9	29.2	1.0153	11.52
7	86588.4	98.78	297.1	94.84	30.96	1187.8	74.7	26.8	1.0154	13.95
8	86592.0	127.21	297.0	75.85	30.92	1186.3	74.2	24.2	1.0159	15.83
9	86590.6	163.99	297.0	60.19	31.11	1193.6	74.0	21.4	1.0159	17.97
10	86577.0	199.24	297.0	37.94	31.12	1194.0	73.8	15.7	1.0159	19.81
11	86575.7	246.50	296.9	15.74	31.14	1194.7	72.7	11.4	1.0161	22.03
12	86577.1	293.85	297.0	-11.76	31.13	1194.4	71.8	6.2	1.0159	24.05
13	86578.0	327.29	296.8	-31.83	31.11	1193.6	71.1	3.0	1.0163	25.38
14	86570.5	349.55	296.7	-44.38	31.20	1197.0	70.5	1.4	1.0166	26.22
15	86582.7	331.65	296.7	-33.95	31.12	1194.0	71.1	3.5	1.0169	25.54
16	86589.0	290.15	296.6	-11.01	31.13	1194.4	72.2	6.5	1.0172	23.88
17	86585.6	245.11	296.6	10.73	31.10	1193.2	73.0	10.2	1.0172	21.95
18	86594.2	209.49	296.5	33.20	31.13	1194.4	73.6	15.2	1.0176	20.29
19	86596.0	155.31	296.4	66.89	31.12	1194.0	74.3	22.2	1.0178	17.47
20	86603.9	138.21	296.4	68.40	31.12	1194.0	74.5	24.4	1.0181	16.48
21	86605.2	101.62	296.4	99.03	31.12	1194.0	74.9	27.2	1.0182	14.13
22	86605.2	65.85	296.3	119.68	31.12	1194.0	75.2	29.8	1.0186	11.37
23	86609.1	65.49	296.2	122.04	31.12	1194.0	75.2	29.8	1.0189	11.34
24	86613.4	51.59	296.2	138.58	31.12	1194.0	75.4	30.9	1.0189	10.06
25	86618.2	32.99	296.1	145.95	31.12	1194.0	75.7	no reading	1.0193	8.05
26	86626.8	25.32	296.1	152.43	31.11	1193.6	75.8	no reading	1.0195	7.05
27	86625.1	0.03	297.1	0.23	0	0.0	0	no reading	1.0161	0.24

Table E5 4° Pitch Angle at 1000 RPM

Pitch Angle (deg)	Propeller speed (rpm)	Blade A (deg)	Blade B (deg)
4	1000	4	4

Point #	Static Pressure Pa	Dynamic Pressure Pa	Temperature K	Thrust N	Tacho Voltage V	Prop Speed rpm	Armature Voltage V	Armature Current A	Air Density kg/m <sup>2</sup>	Tunnel Velocity m/s
0	86382.6	7.54	305.3	0.00	0.00	0.0	0.0	0.0	0.9860	3.91
1	86385.0	6.27	305.3	0.43	0.00	0.0	0.0	0.0	0.9859	3.57
2	86386.1	5.97	305.2	-0.51	0.28	0.0	0.0	0.0	0.9863	3.48
3	86369.8	26.28	305.0	119.76	25.86	992.2	64.3	28.5	0.9868	7.30
4	86369.0	31.14	305.6	118.84	25.86	992.2	63.9	28.5	0.9846	7.95
5	86367.3	48.02	305.0	105.80	25.87	992.6	63.5	27.7	0.9866	9.87
6	86360.5	70.59	305.1	90.69	25.88	993.0	63.2	26.2	0.9863	11.96
7	86369.1	95.62	305.7	76.85	25.88	993.0	62.7	24.2	0.9845	13.94
8	86363.5	126.93	305.4	58.24	25.89	993.4	62.2	21.0	0.9852	16.05
9	86358.8	159.20	304.4	41.56	25.90	993.7	61.7	17.7	0.9884	17.95
10	86357.7	200.79	305.2	23.71	25.91	994.1	61.3	13.5	0.9860	20.18
11	86347.9	235.91	304.7	3.75	25.92	994.5	59.7	7.8	0.9874	21.86
12	86344.4	286.42	304.8	-16.85	25.92	994.5	58.3	4.2	0.9870	24.09
13	86341.5	331.92	305.0	-35.00	25.93	994.9	58.8	0.2	0.9863	25.94
14	86341.5	331.07	305.8	-34.66	25.93	994.9	58.8	0.2	0.9838	25.94
15	86337.2	284.69	305.6	-19.56	25.32	971.5	58.5	3.3	0.9845	24.05
16	86336.9	234.38	305.5	8.63	25.77	988.8	60.6	9.6	0.9846	21.82
17	86336.2	196.61	305.3	24.57	25.49	978.0	60.7	12.8	0.9855	19.98
18	86339.1	156.10	305.5	45.53	25.71	986.5	61.7	18.4	0.9849	17.80
19	86343.2	128.47	305.4	57.49	25.91	994.1	62.3	21.4	0.9850	16.15
20	86335.5	93.69	304.2	77.70	25.67	984.9	62.4	24.1	0.9888	13.77
21	86335.6	72.21	304.8	90.94	25.73	987.2	63.1	26.7	0.9871	12.10
22	86333.8	46.46	304.3	102.98	25.53	979.5	62.5	27.6	0.9885	9.69
23	86335.5	32.75	305.5	118.19	25.77	988.8	62.9	28.8	0.9847	8.16
24	86334.8	27.33	305.4	124.37	25.87	992.6	63.3	29.1	0.9850	7.45
25	86327.9	0.00	305.0	0.99	0	0.2	0	0	0.9862	-



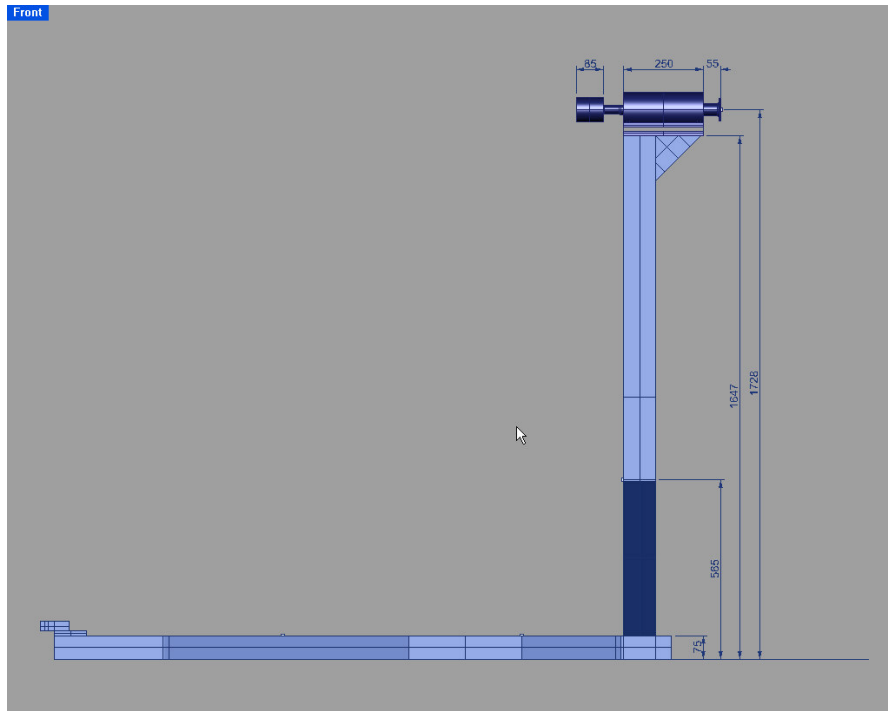


Figure F3 Side view of test rig

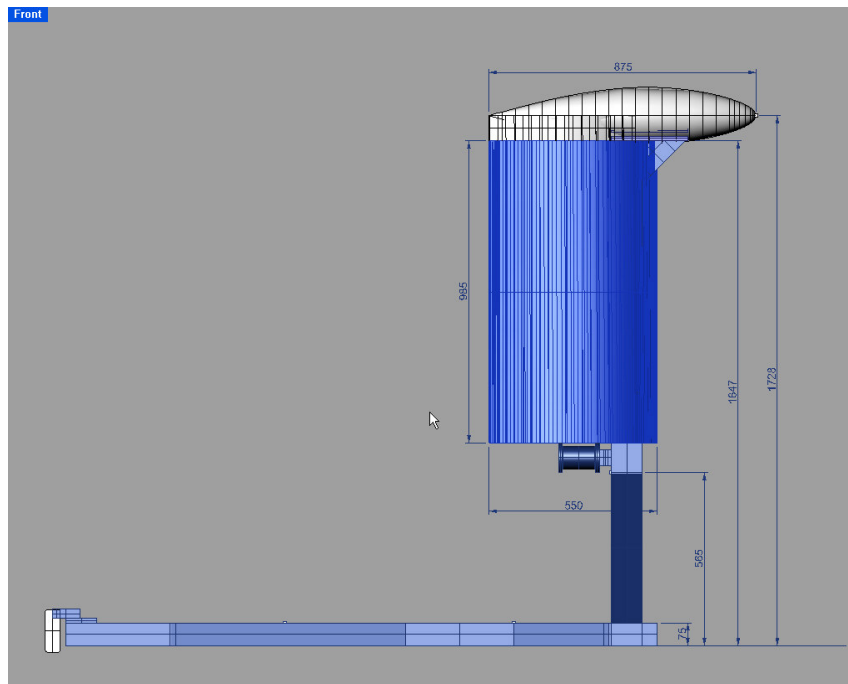


Figure F4 Side view of test rig with fairing

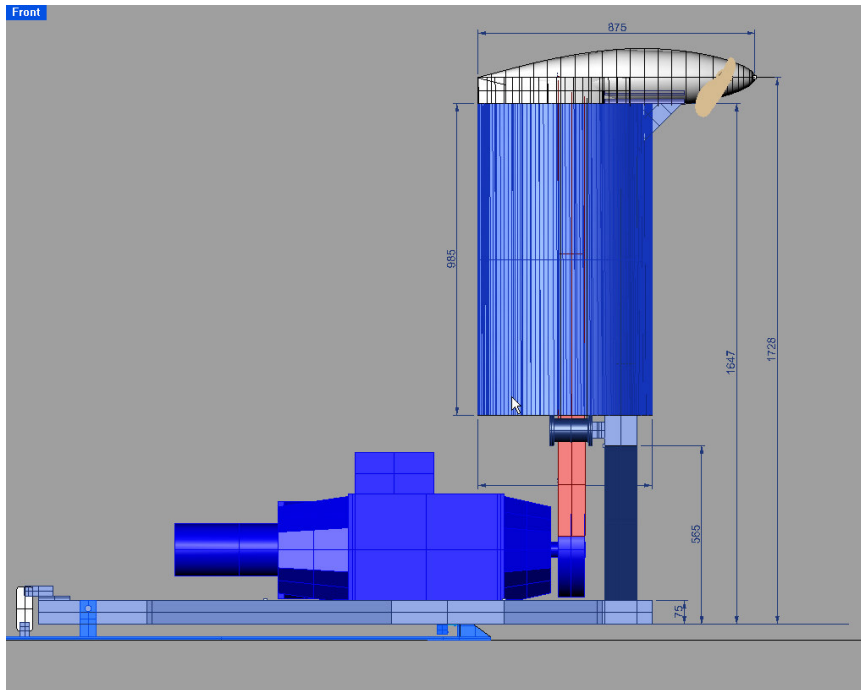


Figure F5 Side view of test rig with fairing, motor and propeller

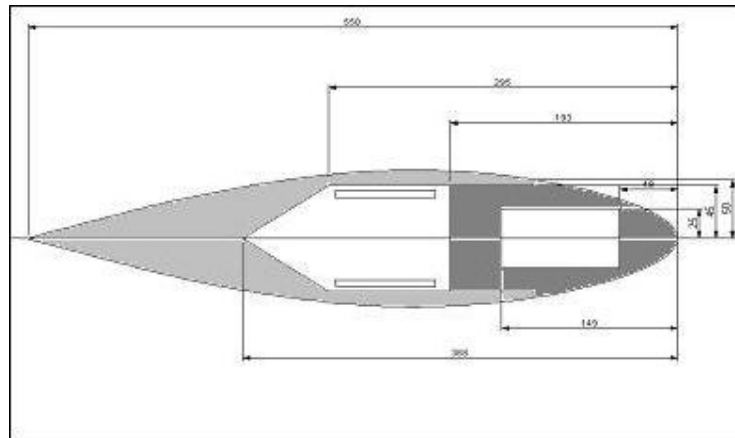


Figure F6 Cross section through new test rig fairing

## **APPENDIX G PROPELLER TEST RIG STRESS CALCULATIONS**

### **Flexure Stress Calculations**

As the final treatment condition was unknown the yield strength was determined through the manufacture of a test sample which was subjected to a tension test to ultimate load.

The mass of the motor was conservatively estimated at 800 kg. Assuming an equal distribution of load between the four vertically orientated flexures, the resultant load on each flexure was calculated to be approximately 1962 N. The thickness of the flexure strip was 1 mm and with a width of 30 mm the cross sectional area of each flexure is 30 mm<sup>2</sup> resulting in a tensile stress of 16 MPa and hence a large factor of safety in tension.

## Propeller blade stressing

Table G1– Calculation of Blade Tensile Stresses at 1200 rpm

Radial Distance from centre (r/R)	Cross Sectional Area (m <sup>2</sup> )	Distance from hub (m)	Outboard Volume (cu. m)	Volume Centroid (m)	Element Mass (kg)	Element Velocity (m/s)	Elemental Force (N)	Cumulative Force (N)	Cumulative tensile stress (MPa)
0	0.00126	0.00	0.000075	0.030	0.060	3.8	29	4650	3.70
0.10	0.00126	0.06	0.000013	0.065	0.010	8.2	10	4622	3.68
0.117	0.00126	0.07	0.000014	0.075	0.012	9.4	14	4611	3.67
0.133	0.00162	0.08	0.000017	0.085	0.014	10.7	18	4598	2.84
0.150	0.00182	0.09	0.000019	0.095	0.015	11.9	23	4579	2.52
0.167	0.00204	0.10	0.000022	0.105	0.017	13.2	29	4556	2.24
0.183	0.00228	0.11	0.000024	0.115	0.019	14.5	35	4528	1.99
0.20	0.00251	0.12	0.000026	0.125	0.021	15.7	41	4493	1.79
0.217	0.00272	0.13	0.000028	0.135	0.022	17.0	48	4452	1.64
0.233	0.00290	0.14	0.000030	0.145	0.024	18.2	55	4404	1.52
0.250	0.00313	0.15	0.000033	0.155	0.026	19.5	64	4348	1.39
0.267	0.00343	0.16	0.000036	0.165	0.029	20.7	74	4284	1.25
0.283	0.00370	0.17	0.000038	0.175	0.030	22.0	84	4210	1.14
0.30	0.00391	0.18	0.000122	0.195	0.097	24.5	300	4126	1.06
0.35	0.00421	0.21	0.000126	0.225	0.101	28.3	357	3826	0.91
0.40	0.00417	0.24	0.000122	0.255	0.098	32.0	393	3469	0.83
0.45	0.00396	0.27	0.000114	0.285	0.091	35.8	409	3076	0.78
0.50	0.00362	0.30	0.000102	0.315	0.081	39.6	405	2667	0.74
0.55	0.00317	0.33	0.000088	0.345	0.071	43.4	385	2262	0.71
0.60	0.00272	0.36	0.000076	0.375	0.061	47.1	360	1877	0.69
0.65	0.00235	0.39	0.000066	0.405	0.053	50.9	337	1517	0.65
0.70	0.00204	0.42	0.000105	0.450	0.084	56.5	596	1181	0.58
0.80	0.00145	0.48	0.000066	0.510	0.053	64.1	424	585	0.40
0.90	0.00074	0.54	0.000022	0.570	0.018	71.6	161	161	0.22
1.00	0.00000	0.60	0.000000	0.6	0.000	75.4	0	0	0.00